Nonsteady Load Responses of Wind Turbines to Atmospheric and Mountain-Generated Turbulence Eddies, With Impacts on the Main Bearing: A Validation Study

James G. Brasseur,[1] Jennifer Morris,[2] Edward Hart,[2] Abbas Kazemi Amiri,[2] Yi Guo,[3] and Jonathan Keller[4]

1 University of Colorado Boulder
2 University of Strathclyde
3 Technical University of Denmark
4 National Renewable Energy Laboratory

NREL is a national laboratory of the U.S. Department of Energy
Office of Energy Efficiency & Renewable Energy
Operated by the Alliance for Sustainable Energy, LLC

This report is available at no cost from the National Renewable Energy Laboratory (NREL) at www.nrel.gov/publications.

Contract No. DE-AC36-08GO28308

Technical Report
NREL/TP-5000-88503
August 2024

Nonsteady Load Responses of Wind Turbines to Atmospheric and Mountain-Generated Turbulence Eddies, With Impacts on the Main Bearing: A Validation Study

James G. Brasseur,[1] Jennifer Morris,[2] Edward Hart,[2] Abbas Kazemi Amiri,[2] Yi Guo,[3] and Jonathan Keller[4]

1 University of Colorado Boulder
2 University of Strathclyde
3 Technical University of Denmark
4 National Renewable Energy Laboratory

Suggested Citation
Brasseur, James G., Jennifer Morris, Edward Hart, Abbas Kazemi Amiri, Yi Guo, and Jonathan Keller. 2024. *Nonsteady Load Responses of Wind Turbines to Atmospheric and Mountain-Generated Turbulence Eddies, With Impacts on the Main Bearing: A Validation Study*. Golden, CO: National Renewable Energy Laboratory. NREL/TP-5000-88503. https://www.nrel.gov/docs/fy24osti/88503.pdf.

NREL is a national laboratory of the U.S. Department of Energy
Office of Energy Efficiency & Renewable Energy
Operated by the Alliance for Sustainable Energy, LLC

This report is available at no cost from the National Renewable Energy Laboratory (NREL) at www.nrel.gov/publications.

Contract No. DE-AC36-08GO28308

Technical Report
NREL/TP-5000-88503
August 2024

National Renewable Energy Laboratory
15013 Denver West Parkway
Golden, CO 80401
303-275-3000 • www.nrel.gov

NOTICE

This work was authored in part by the National Renewable Energy Laboratory, operated by Alliance for Sustainable Energy, LLC, for the U.S. Department of Energy (DOE) under Contract No. DE-AC36-08GO28308. Funding provided by the U.S. Department of Energy Office of Energy Efficiency and Renewable Energy Wind Energy Technologies Office. The views expressed herein do not necessarily represent the views of the DOE or the U.S. Government.

Cover Photos by Dennis Schroeder: (clockwise, left to right) NREL 51934, NREL 45897, NREL 42160, NREL 45891, NREL 48097, NREL 46526.

Acknowledgments

The computational program was financially supported by the U.S. Department of Energy Office of Energy Efficiency and Renewable Energy (Brasseur, Lavely). The field study was supported by the Centre for Doctoral Training in Wind & Marine Energy Systems & Structures (CDT-WAMESS) program at the University of Strathclyde (Morris) and by the National Renewable Energy Laboratory and the U.S. Department of Energy (Brasseur, Keller, Guo). Hart was funded by a Brunel Fellowship from the "Royal Commission for the Exhibition of 1851." We acknowledge Adam Lavely, whose Ph.D. thesis research provided the key computational results in Figure 4 around which the field analysis is based. Lavely was supported by the Walker Fellowship of the Penn State Applied Research Laboratory, and computational resources were provided by the National Science Foundation Extreme Science and Engineering Discovery Environment (XSEDE) program. We acknowledge with thanks the contributions to instrumentation analysis by Latha Sethuraman and George Scott at the National Renewable Energy Laboratory.

List of Acronyms

1P	once-per-revolution
3P	three-per-revolution
ABL	atmospheric boundary layer
ALM	actuator line model
BEBM	blade edge bending moment
BFBM	blade flap bending moment
cc	correlation coefficient
DOE	U.S. Department of Energy
Hz	hertz
kNm	kilonewton-meter
LCOE	levelized cost of energy
LES	large-eddy simulation
LHS	left-hand side
LSBMM	low-speed shaft (main shaft) bending moment vector magnitude
LST	low-speed shaft (main shaft) torque
M80CWS	meteorological (met) tower cup anemometer wind speed at 80 m (hub height)
MW	megawatt
m/s	meter(s) per second
NREL	National Renewable Energy Laboratory
NWS	nacelle wind speed (measured from nacelle cup anemometer)
NWTC	National Wind Technology Center (NREL Flatirons Campus)
O&M	operations and maintenance
OOP	out-of-plane (i.e., on a plane perpendicular to the main shaft, or x, axis)
OOPBM	OOP (out-of-plane) bending moment
RHS	right-hand side
rpm	revolutions per minute
SCADA	supervisory control and data acquisition
SRBIA	single rotating blade in the atmosphere
TBMM	tower base bending moment vector magnitude
TKE	turbulent kinetic energy
WS	wind speed
WD	wind direction

Executive Summary

Previous computational and field experiments identified three characteristic time scales in the aerodynamic responses of utility-scale wind turbine loads to atmospheric boundary layer (ABL) turbulence. The first is a 30 to 90 second time scale for the passage of high/low speed "streaks" through the rotor plane, the second is the blade and rotor rotation time scales (approximately 1 to 5 seconds), and the third are sub second time responses to blade rotations through the internal gradients within individual coherent eddy structures. In the current study, we compare wind turbine drivetrain responses to the highly nonsteady interactions between wind turbine rotors and energetic turbulence eddies with the atmosphere from two classes of well-resolved data. The first class is from high-fidelity large-eddy simulation (LES) of a typical daytime ABL embedded with an actuator line model of the National Renewable Energy Laboratory (NREL) 5-megawatt (MW) wind turbine model. The second class is field data from the GE 1.5-MW wind turbine at the National Wind Technology Center (NWTC) on the NREL Flatirons Campus, 5 kilometers east of the Rocky Mountain Front Range. With these data we contrast the responses to the passage of ABL eddies embedded within northerly/southerly winds with the passage of the mountain-generated eddies embedded within the westerly winds. These analyses are in context with the nonsteady forcing of the main bearing by the aerodynamic generation of the nontorque bending moment vector on the main shaft.

Potentially relevant to main bearing failure mechanisms, both computational and field data show that the magnitudes of turbulence-generated nontorque bending moments are of order or larger than torque. Whereas torque underlies power, we show that nonsteady variations in nontorque bending moment underlie nonsteady force variations on the main bearing. However, the temporal variations in these two responses are uncorrelated, implying that the aerodynamic mechanisms that drive power and main bearing response are fundamentally different. We find this to be the case in the field with both mountain-generated eddies (westerly winds) and ABL-generated eddies (northerly/southerly winds). Whereas the time and length scales are comparable, the mountain eddies were somewhat more energetic than the northerly/southerly ABL eddies. Interestingly, however, the fluctuations in nontorque bending moment that force the main bearing were found to be stronger when forced by the ABL eddies than the mountain eddies.

The field studies validate the key results from the computational study and show even stronger response in the nontorque bending moment than in the computer simulations. In all cases, the torque and nontorque bending moments are temporally uncorrelated, torque and power are driven by time variations in rotor-averaged horizontal wind velocity, and nontorque bending moments are driven by time changes in the degree of nonuniformity in the distribution of velocity over the rotor plane. Thus, the results generalize the mechanisms underlying nonsteady aerodynamic forcing of the drivetrain to classes of turbulence eddy types that have strengths of order or stronger than ABL eddies, and with transverse coherence lengths of order the wind turbine rotor. These eddy types include the turbulence eddies naturally embedded with the lower atmosphere, the topography-generated turbulence eddies generated by flow over mountains, and, by extension, the turbulence eddies generated in the wake of upstream wind turbine rotors.

Table of Contents

List of Figures

List of Tables

1 Introduction: Motivations and Aims

Levelized cost of energy (LCOE) is the ratio of operating costs plus capital investment to energy production over the current wind turbine life span of 20 to 30 years. Despite significant reductions in the LCOE from wind over the past decades (Wiser and Bolinger 2019; Wiser et al. 2019), the scale of future deployments, with extensions to offshore, will require further reductions in LCOE in the coming years (Wiser et al. 2015; UK Gov. 2019). Whereas increases in annual power production (the denominator in LCOE) is often the focus of reductions in LCOE, operations and maintenance (O&M) costs (in the numerator of LCOE) are a sizable and potentially growing share of LCOE, especially as lower upfront costs and better performance contribute to a decline in LCOE. Wind plant O&M can account for 25% to 35% or more of LCOE (Carrol et al. 2017; Wiser et al. 2019) and can be as much as 50% for land-based plants (Wiser et al. 2019). Drivetrain component reliability is an important contribution to turbine O&M and wind plant LCOE due to repair costs, lost revenue during downtime, and logistic challenges, especially as wind plants move offshore (Dao et al. 2019). The main bearing, in particular, is a critical drivetrain component with high replacement cost due to the typical requirement for a large crane and the potential need for a vessel to remove the rotor and main shaft during replacement.

Although comprehensive data are lacking, it has become apparent that the frequency of main bearing failure exceeds expectations; the rate of premature bearing failures are unacceptably high for some populations (Chovan 2018; Hart et al. 2019, 2023). However, the primary underlying mechanisms are, as yet, unclear (Kotzalas and Doll 2010; Hart et al. 2023; Kenworthy et al. 2023b), largely because main bearings have received much less attention than other drivetrain components (Keller et al. 2016, 2021). This is a knowledge deficit that poses serious risk to wind plant profitability and there is no clear solution in both design and operation. What is known is that bearing failures are strongly driven by the detailed characteristics of the applied loadings within operational conditions in which they function (Hart et al. 2020, 2022). These loadings are strongly time-varying due to the strongly unsteady loads experienced by wind turbine main bearings in operation, in contrast with the steadier conditions of conventional mechanical power plant operation (Hart et al. 2019, 2020). There is evidence suggesting that main bearing failures are associated with the high loading, low speed, and low lubrication layer thickness within the bearing, indicating a potential for repeated metal-to-metal contact (Kotzalas and Doll 2010; Chovan 2019; Hart et al. 2022). The current study therefore investigates a key mechanism with the potential to generate strong nonsteady variations in main bearing loadings.

Aerodynamic interactions between the turbine rotor and the spatially and temporally varying complex wind field in which it is operating generate time-varying drivetrain loads with fluctuations around the mean that can easily vary by as much as ±50% (Vijayakumar et al. 2016; Lavely 2017; Nandi et al. 2017; Hart 2020; Hart et al. 2020). Higher wind speeds and capacity factors, as well as shear and turbulence, tend to increase wear-and-tear and turbine O&M costs (Wiser et al. 2019). To fully understand the main bearing failure mechanisms that shorten bearing operational lifetimes, it is necessary to understand in detail the characteristics of

temporal changes in the loads (i.e., forces and moments) that act on the main shaft from the aerodynamic interactions between the rotating wind turbine rotor and the turbulent winds, specifically the energy-dominant turbulence eddies embedded within the atmospheric boundary layer (ABL). These strong buoyancy and shear-generated eddies pass continuously through the turbine rotors from sunup to sundown in the daytime ABL, the period when turbulent fluctuations are, by far, strongest (Svensson, et al. 2011). The current research considers this problem from a real-world viewpoint, contrasting the analysis of data collected from a 5-megawatt (MW) wind turbine with an actuator line model (ALM) of the rotor blades embedded within large-eddy simulation (LES) of the daytime ABL with the analysis of a series of datasets that have been collected from an extensive field measurement campaign. These data include the synchronized quantification of the time-varying moments on the wind turbine main shaft together with the time variations in the wind velocity field taken from anemometers on both a meteorological tower (met tower) and the wind turbine nacelle.

1.1 Potential Impacts of Atmospheric Turbulence on Main Bearing Function

Figure 1 illustrates the wind turbine drivetrain, showing the rotor weight and the force and moment vectors at the hub and on the main shaft that are driven by atmospheric turbulence and the time changes in the net radial force, $\mathbf{F}_{bearing}$, which act on the bearing by the main shaft driven by the hub moment and force. We illustrate the distribution of the bearing force over "load zones" that surround $\mathbf{F}_{bearing}$. The changes in the direction and magnitude of $\mathbf{F}_{bearing}$ with time, driven by the passage of turbulence eddies through the rotor, cause corresponding time changes in the location, magnitude, and extent of the load zone surrounding $\mathbf{F}_{bearing}$. We hypothesize that the passage of the rollers through specific repetitive time changes in the location and magnitude of the bearing load zone could, over time, be detrimental to bearing function. As will be shown, the time variations in $\mathbf{F}_{bearing}(t)$ arise from the time variations in the moment acting at the hub on the main shaft from aerodynamic forcing of the rotor blades. The hypothesis is that premature failure of the main bearing is encouraged or caused by specific repetitive time changes in bearing response to the time changes in the magnitude and location of the load zone that result from the aerodynamic interactions between the rotor and the energy-dominant turbulence eddies within the daytime ABL. Detrimental bearing responses might include, for example, time changes in lubrication layer thickness that encourage metal-to-metal contact, or specific displacements of the roller or cage that reorient the roller just before a second load impulse detrimental to the reoriented roller.

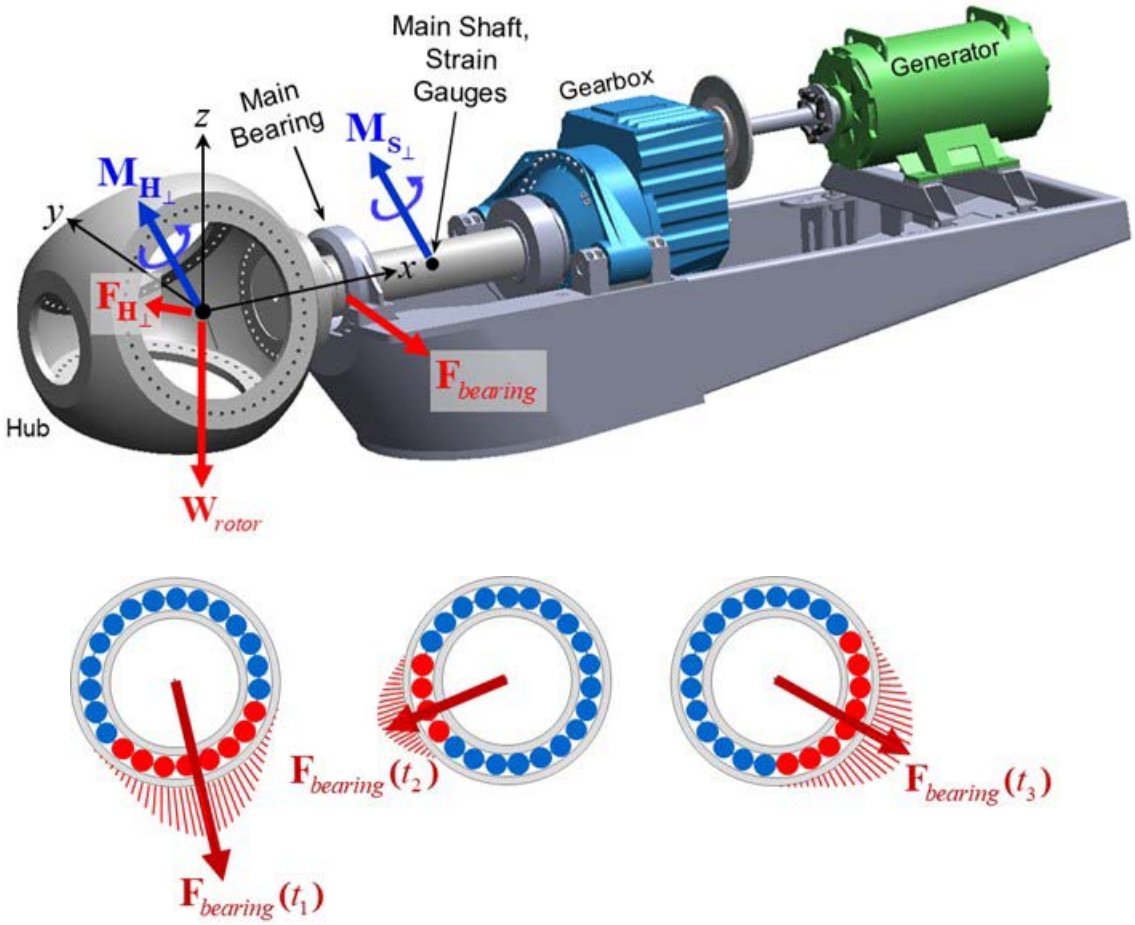

Figure 1. Illustration of the hub and three-point mount drivetrain of a typical utility-scale wind turbine (top) and the time-changing bearing force and its distribution over time-changing load zones (bottom).

In the upper figure the x-axis is along the main shaft centerline with its origin at the hub with the z-axis nominally in the direction opposite to gravity. Shown are the following vectors: $\mathbf{F}_{\mathbf{H}_\perp}$ and $\mathbf{M}_{\mathbf{H}_\perp}$ are the aerodynamically driven force and moment vectors on the rotor acting at the hub and projected on a plane perpendicular to x (out-of-plane, or OOP); $\mathbf{F}_{bearing}$ is the net radial (OOP) force vector acting on the main bearing at its interface with the main shaft; $\mathbf{M}_{\mathbf{S}_\perp}$ is the OOP moment vector measured on the main shaft with strain gages in the wind turbine field dataset; and $\mathbf{W}_{rotor}$ is the rotor weight vector. In the lower figure t_1, t_2, and t_3 are three sequential times to illustrate a potential impact of the passage of strong atmospheric turbulence eddies through the rotor plane on time changes in both the direction and magnitude of the radial bearing force and its distribution over the main bearing load zone.

The following expression results from an equilibrium moment balance (inertia neglected) on the main shaft between the hub and the gearbox entrance, specifically by summing moment components around the gearbox location on the main shaft:

$$\left[\mathbf{F}_{bearing}\right]_{\substack{aerodynamic\\contribution}} = \mathbf{F}_{bearing} - \frac{L}{L_2}\mathbf{W}_{rotor} = \frac{1}{L_2}\left(-M_{H_z}\mathbf{e}_y + M_{H_y}\mathbf{e}_z\right) + \frac{L}{L_2}\mathbf{F}_{\mathbf{H}_\perp}, \quad (1)$$

where $\mathbf{F}_{bearing}$ is the net radial force acting on the main bearing, L is the distance between the hub and gearbox, and L_2 is the distance between the main bearing and gearbox. In Figure 1, x is along the main shaft from the hub, and y and z are perpendicular to x with z in the plane that passes

through the gravity vector. When the main shaft is horizontal to the ground, z points opposite to gravity; when the main shaft is tilted, $\mathbf{W}_{rotor}$ is the rotor weight vector projected onto the z axis. The contribution from the weight of the rotor, $\mathbf{W}_{rotor} = -W_{rotor}\mathbf{e}_z$, is placed on the left-hand side (LHS) so that the right-hand side (RHS) contains only the terms that underlie the time variations in bearing force vector magnitude and direction from aerodynamic interactions between the passage of atmospheric turbulence eddies through the rotor plane. Sub H implies "at the hub." $\mathbf{M}_{\mathbf{H}_\perp} = M_y\mathbf{e}_y + M_z\mathbf{e}_z$ and $\mathbf{F}_{H_\perp} = F_{H_y}\mathbf{e}_y + F_{H_z}\mathbf{e}_z$ are the "out-of-plane" (OOP), or radial, bending moment and force vectors acting at the hub in response to aerodynamic interactions between the turbulent wind and the rotor blades. As discussed in more detail in Section 2.3, $\mathbf{M}_{\mathbf{H}_\perp}$ arises from the imbalance in aerodynamic force over the three blades. $\mathbf{F}_{H_\perp}$ quantifies the imbalance in the force vectors on each blade when projected onto the rotor plane.

The complete moment and force vectors are $\mathbf{M}_{\mathbf{H}} = M_{H_x}\mathbf{e}_x + \mathbf{M}_{\mathbf{H}_\perp}$ and $\mathbf{F}_{\mathbf{H}} = F_{H_x}\mathbf{e}_x + \mathbf{F}_{\mathbf{H}_\perp}$, where M_{H_x} is torque ($\propto$ power) and F_{H_x} is thrust on the main shaft from the rotor, which along with any contribution from the weight of the rotor yields the net axial force acting on the main bearing. Equation 1 shows that time variations in the components of $\mathbf{M}_{\mathbf{H}_\perp}(t)$ create time variations in the net bearing radial force, $\mathbf{F}_{bearing}(t)$. In addition, time variations in net aerodynamic rotor force at the hub also contribute to $\mathbf{F}_{bearing}(t)$ from interactions between the rotor and ABL turbulence. However, order of magnitude estimates of $\mathbf{M}_{\mathbf{H}_\perp}$ versus $\mathbf{F}_{\mathbf{H}_\perp}$ suggest that $\mathbf{M}_{\mathbf{H}_\perp}$ should dominate and an ongoing LES study with an ALM for the wind turbine blades (Kenworthy et al. 2023a) indicates that the force term on the RHS of Eq. (1) is more than an order of magnitude smaller than the moment terms, on average, and is temporally uncorrelated with bearing force on the LHS. By contrast, the OOP hub moment $\mathbf{M}_{\mathbf{H}_\perp}(t)$ is highly correlated with $\mathbf{F}_{bearing}(t)$, implying that the time variations in bearing force are nearly entirely in response to the time variations in the hub moment components on the RHS of Eq. (1).

In Section 2 we describe a computational experiment in which an ALM representation of the National Renewable Energy Laboratory (NREL) 5-MW wind turbine rotor is embedded within a high-fidelity LES of the canonical daytime ABL. There we correlate turbulence-induced time variations in hub moment $\mathbf{M}_{\mathbf{H}_\perp}(t)$ with flow variables to determine mechanisms underlying time responses in main bearing force through Eq. (1). In Sections 7 and 9 we compare key statistical characteristics from the computational experiments with corresponding statistics from field data from the GE 1.5-MW wind turbine at the NREL Flatirons site adjacent to the Rocky Mountain Front Range. Here, strain gauges were used to measure the two components of the OOP main shaft moment vector $\mathbf{M}_{\mathbf{S}_\perp}$ downwind of the main bearing, rather than the hub moment $\mathbf{M}_{\mathbf{H}_\perp}$ from the computational experiments. To compare correlations from the computational experiment with the field results, it is necessary to relate $\mathbf{M}_{\mathbf{H}_\perp}$ to $\mathbf{M}_{\mathbf{S}_\perp}$. Combining Eq. (1) with an equilibrium moment balance over the portion of the main shaft between the strain gauges and the gearbox entrance separated by distance L_4 shown in Figure 1, the equilibrium relationship between $\mathbf{M}_{\mathbf{S}_\perp}$ and $\mathbf{M}_{\mathbf{H}_\perp}$ may be derived:

$$\left[\mathbf{M}_{\mathbf{S}_\perp}\right]_{\substack{aerodynamic\\contribution}} = \mathbf{M}_{\mathbf{S}_\perp} + \frac{L_1 L_4}{L_2} W_{rotor}\mathbf{e}_y = \frac{L_4}{L_2}\left[\mathbf{M}_{\mathbf{H}_\perp} + L_1\left(F_{H_z}\mathbf{e}_y - F_{H_y}\mathbf{e}_z\right)\right] \tag{2}$$

Like Eq. (1), the contribution from rotor weight is placed on the LHS so that the RHS describes the time changes in $\mathbf{M}_{\mathbf{S}_\perp}(t)$ that are driven by the aerodynamic interactions between the rotor blades and turbulence eddies. Like Eq. (1), the OOP bending moment on the main shaft is proportional to the aerodynamic OOP moment and force vectors acting at the hub from the rotor. For the same reasons that the moment contribution to Eq. (1) dominates the force contribution in the generation of the main bearing radial force, the RHS of Eq. (2) is very likely dominated by the OOP hub moment, $\mathbf{M}_{\mathbf{H}_\perp}$. We argue, therefore, that the statistical correlations we develop in the current analysis for the temporal relationships among $\mathbf{M}_{\mathbf{S}_\perp}(t)$, torque and wind velocities should be close to the same as between $\mathbf{M}_{\mathbf{H}_\perp}(t)$, torque, and wind velocities.

It is the existence of specific repetitive deleterious time variations in the net radial and axial forces on the bearing that we hypothesize may underlie premature failures of the main bearing. Ultimately our aim is to identify specific time changes in these forces that are driven by specific sources to create nonsteady characteristics of the nontorque moment components of $\mathbf{M}_{\mathbf{H}_\perp}(t)$ and thrust that may contribute to premature main bearing failures. The nontorque moment that generates $\mathbf{F}_{bearing}(t)$ is illustrated by the blue vector at the hub in Figure 1. We hypothesize that the nonsteady nontorque moment vector, $\mathbf{M}_{\mathbf{H}_\perp}(t)$, generates time changes in $\mathbf{F}_{bearing}(t)$, and therefore the bearing load zone, in such a manner as to contribute to bearing failure. In the current study, we address a specific source for the generation of the OOP bending moment, $\mathbf{M}_{\mathbf{H}_\perp}(t)$: the nonsteady aerodynamic forcings of the wind turbine blades and rotor by the energy-dominant atmospheric turbulence eddies within the daytime ABL as they pass through the rotor plane (Vijayakumar and Brasseur 2019).

Atmospheric turbulence is, by far, strongest during the daytime period; this is when solar heating of the Earth's surface generates atmospheric thermals that dominate in the mixed layer, localized convectively driven concentrations of strong vertical turbulence motion ("updrafts"). The horizontal winds required to drive wind turbines, by contrast, create large mean shear-rate adjacent to the surface that drives the creation of highly coherent streamwise-elongated energy-dominant eddies shown in Figure 3 from LES. These concentrations of horizontal fluctuating velocity are commonly referred to as "streaks." These strong horizontal fluctuations are contained within the highly coherent streamwise-elongated energy-dominant eddies shown in Figure 3 from LES, as will be described in detail in Section 2.1. These structures dominate the lower 20% of the daytime ABL, 200 to 400 meters (m) from the surface, where wind turbines operate, to create the structure of the energy-containing coherent turbulence eddies that pass through wind turbine rotors (Khanna and Brasseur 1998). We hypothesize that the nonsteady aerodynamic forcing of the rotor blades in response to the continual passage of these energetic coherent turbulence eddies create strong temporal changes in the net axial and radial forces on the main bearing that may contribute to bearing wear, and perhaps eventual failure. This is particularly the case where the wind turbines are directly forced by atmospheric turbulence eddies. These are the wind turbines in the first few rows of large wind plants and throughout widely spread smaller wind plants, many of which operate in hilly terrain.

LES and field studies of wind turbines operating within the daytime ABL over land (Vijayakumar et al. 2016; Nandi et al. 2017; Lavely 2017) have shown that the characteristic turbulence eddies within the lower ABL typically pass through the wind turbine rotor with a time scale of order a minute (30 to 90 seconds [s]). Thus, a wind turbine on a typical day experiences many hundreds of eddy passages during the daytime period, when atmospheric turbulence is strongest. A field study (Nandi et al. 2017) and a study applying full blade-boundary-layer-resolved hybrid unsteady Reynolds-averaged Navier-Stokes (URANS)/LES (Vijayakumar et al. 2016) have identified two shorter time scales in the responses to nonsteady aerodynamic forcings of the rotor disk, in addition to eddy-passage time. One is the time scale associated with the rotational passage of the rotor blades through the turbulence eddies. Because utility-scale wind turbine rotors typically rotate at 10 to 20 revolutions per minute (rpm), the once-per-revolution (1P) rotational time scale is in the range 3 to 6 s, an order of magnitude below the eddy passage time scale, whereas the more common three-per-revolution (3P) response is ~1 to 3 s.

The second, shorter, time-scale response is explained with Figure 2 from an extremely high-resolution simulation of a single rotating blade in the atmosphere (SRBIA) passing through an LES-generated ABL turbulence eddy (Vijayakumar et al. 2016). These shortest temporal events are found to be ramp-like load changes in torque and OOP bending moment on the main shaft (Vijayakumar et al. 2016) with time scales below a second (Nandi et al. 2017). They result from the time changes in the aerodynamic forces on rotor blades as they cut through the localized spatial gradients in velocity within individual atmospheric eddies. These are elongated eddies that pass through the rotor plane every 30 to 90 s (discussed in Section 2.3 in context with Figure 5). Because the nonsteady torque variations shown in Figure 2 are representative of the nonsteady variations in the main shaft moment vector at the hub (Vijayakumar et al. 2016), and because the short-duration temporal events cause sudden changes in main shaft loads as high as ±50% of the mean, these short-duration ramp-like events in hub moment have the potential to stimulate strong nonsteady transients in the main bearing load zone.

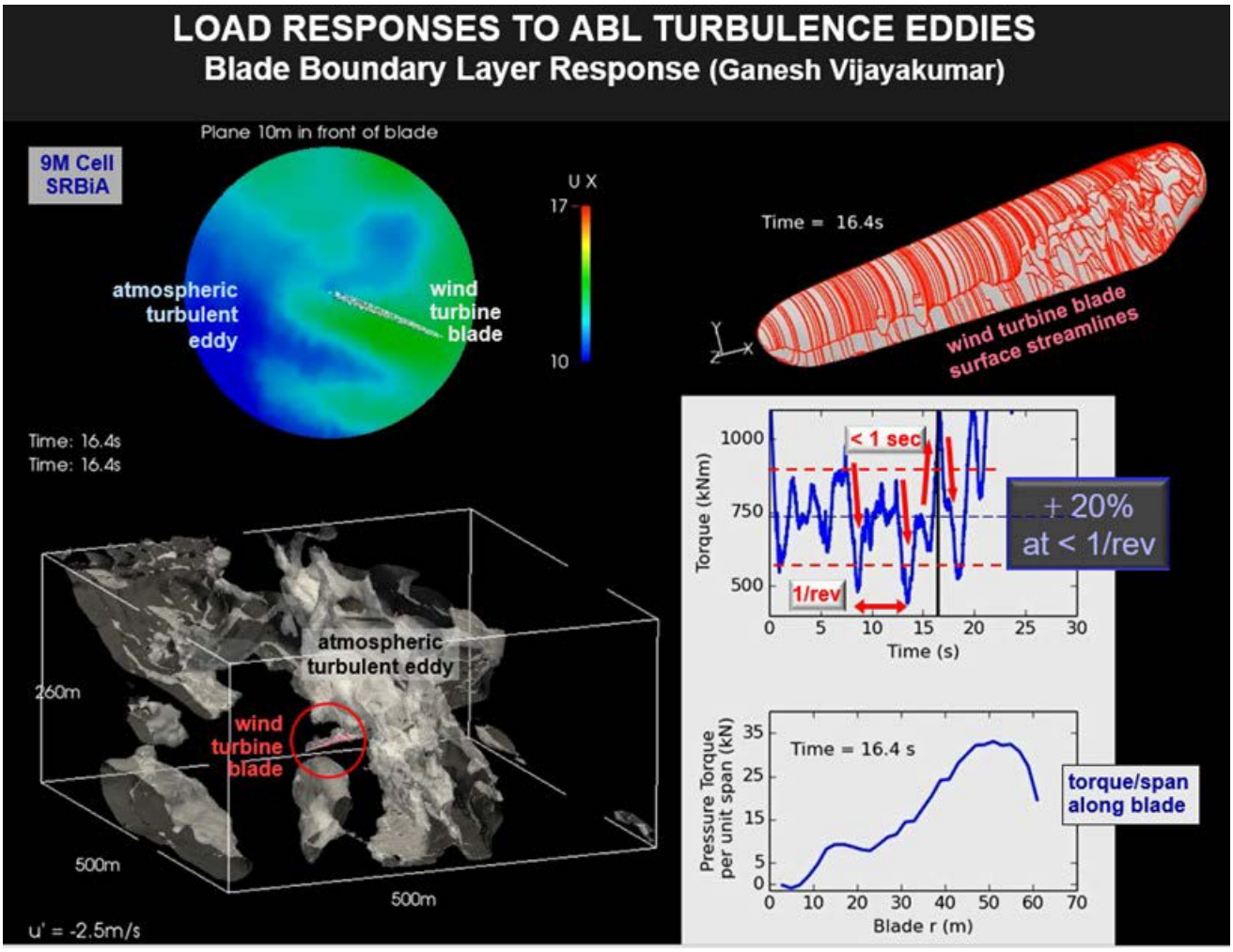

Figure 2. Passage of a wind turbine blade through a turbulence eddy embedded within the daytime ABL.

The results were simulated with extreme-resolution blade-boundary-layer-resolved hybrid URANS-LES numerical simulations of an NREL 5-MW wind turbine blade rotating through an LES of the daytime atmospheric boundary layer by Vijayakumar et al. (2016). The predictions indicate the existence of ramp-like time changes in torque at subsecond time scales that result from blade passage through internal velocity gradients within the eddy.

As will be described in Section 2, potentially important discoveries from LES-ALM computations were reported by Lavely (2017). In the current study, we test these discoveries with field data. Previous studies have shown that blade lift, and consequently thrust and torque on the main shaft, respond primarily to time changes in horizontal velocity (i.e., perpendicular to the rotor disk) and secondarily to time changes in convectively driven vertical velocity, both of which fluctuate by several meters per second (m/s) with the passage of energetic turbulence eddies (Vijayakumar et al. 2016; Lavely 2017). *With the current field study (Section 7) we verify the computational result that the nontorque moment on the main shaft is driven by physics that are very different from that driving torque, implying that mechanisms developed to reduce LCOE by increasing power production must be fundamentally different from those designed to reduce LCOE by suppressing a potential main bearing failure mechanism.*

1.2 Aims and Organization

Our aim is to apply field data from the GE 1.5-MW wind turbine at the NREL Flatirons Campus, which is owned by the U.S. Department of Energy (DOE), to quantify the details by which nonsteady aerodynamic forcing on a wind turbine rotor from turbulence eddying motions impact nonsteady responses on the main shaft and, potentially, main bearing function. We specifically aim to validate the key computation-based discoveries described in Section 2.

Because the Flatirons Campus lies on the plains to the east of a well-defined ridge that defines the eastern edge of the Rocky Mountain range, westerly winds contain turbulence eddying motions that are generated by flow separation over the adjacent mountain ridge (Section 3). Given that the predominant wind direction is from the west (westerly) and that the mountain-generated turbulence eddies have strength and scale not too different from atmospheric eddies (Sections 3.2 and 9), we contrast the passage of mountain-generated turbulence eddies with typical daytime atmospheric turbulence eddies and compare statistical quantifications and correlations from westerly winds with mountain-generated eddies to those winds from the north or south embedded with ABL eddies. Because the met tower is located to the west of the GE 1.5-MW wind turbine, we could only use met tower data for analysis of wind turbine response to westerly winds. We therefore compared statistics from data obtained with the anemometers on the met tower with corresponding statistics using the cup anemometer on the nacelle with westerly winds to interpret the results obtained with northerly/southerly winds.

Our field study therefore separates into two parts: (1) analysis of the impact of turbulence eddying motions generated by air flow over and through the mountains to the west of the wind turbine and comparing statistics using the met tower vs. nacelle anemometer data, and (2) statistical comparison of results from westerly vs. northerly/southerly winds using the nacelle anemometer to determine the differences in measured load responses from mountain-eddy turbulence vs. turbulence eddies embedded within the daytime ABL. Our specific aims include the following quantifications:

- The same turbulence events observed at both the met tower and the wind turbine for westerly winds
- Temporal correlations between horizontal wind speed and main shaft torque, main shaft bending moments, blade flap bending moment (BFBM) and blade edge bending moment (BEBM) at the blade root, and tower base bending moment vector magnitude (TBMM)
- Temporal correlations in main shaft bending moment to fluctuations in torque and horizontal wind speed (and, by extension, thrust)
- The validity of replacing met tower data with nacelle anemometer data for statistical analysis of ABL turbulence-turbine interactions with northerly/southerly winds
- Key differences in responses of wind turbine loads to mountain-generated turbulence vs. daytime ABL turbulence by comparing statistical responses to westerly vs. northerly/southerly winds.

The report is organized as follows. In the next section (Section 2) we provide the details of the LES of the daytime ABL with an embedded actuator line wind turbine rotor model for the NREL

5-MW wind turbine with key results from the computational experiment evaluated in the field study. In Sections 3 and 4 we describe the field experiment with the GE 1.5-MW wind turbine, the met tower and wind turbine instrumentation, the data analyzed, and in Section 5 the transition in power, rotor RPM and blade pitch between regimes 2 and 3. In Section 6 we describe qualitatively the nature of the mountain eddies that pass through the NREL/GE wind turbine rotor, we develop a method to determine the passage of mountain eddies from the met tower to the wind turbine, and we down-select the most probable eddy passage events within the westerly winds. Using these down-selected data, we analyze in Section 7 the response of the 1.5-MW wind turbine loads to turbulence eddy passage for westerly winds and compare with the key computational results. In Section 8 we analyze the validity of using the nacelle anemometer in place of met tower wind data and show surprisingly good correlation between the two. This sets the stage in Section 9 for analysis of northerly/southerly wind data, where turbulence eddies are formed within the ABL, and for comparisons with westerly wind data where the turbulence eddies are formed by flow separation off the Front Range mountains. We end in Section 10 with generalized analysis and description of the new levels of understanding obtained with our integrated computational/experimental study.

2 Impacts of Atmospheric Turbulence on Main Shaft Hub Loadings From a Computational Experiment Based on High-Fidelity Large-Eddy Simulation

2.1 Large-Eddy Simulation of Daytime Atmospheric Boundary Layer Turbulence Structure

An extremely well-resolved LES of a moderately convective typical daytime ABL was carried out as a "precursor" simulation in which an actuator line model (ALM) of the NREL 5-MW wind turbine rotor was embedded to develop a computational experiment to quantify the response of a utility-scale wind turbine to typical daytime atmospheric turbulence (Section 2.2). The details of the LES/ABL code have been described in a number of publications (see Jayaraman and Brasseur 2021 and references therein). The code solves the LES-filtered incompressible Navier-Stokes equation with the Coriolis acceleration term written in a form where mean pressure gradient is specified with a "geostrophic wind" vector. The Boussinesq approximation models the buoyancy force term with the incompressible form of the continuity equation applied so that resolved pressure satisfies a Poisson equation. The thermal energy equation was written for potential temperature and solved with surface temperature flux specified. The subfilter-scale stress (momentum) and flux (temperature) terms were modeled with a one-equation eddy viscosity model with a constant of 0.1. The ABL geometrical grid (i.e., before dealiasing) was 756 × 756 × 256 grid points over a computational domain of 5120 m × 5120 m × 2048 m with a "capping inversion" (a local stabilizing positive temperature gradient region of thickness ≈100 m typical of the daytime ABL) at $z_i \approx 1000$ m in the quasi-stationary state, where z_i is the height of the capping inversion.

The well-resolved ABL LES produced grid cells with size of order the blade chord of the NREL 5-MW wind turbine. The geostrophic wind (effectively, the wind speed above the capping inversion) was specified as 15 m/s and the surface temperature flux (a boundary condition for the potential temperature equation) was specified as 0.20 Km/s, which is typical for the daytime ABL (Wyngaard 2010, Figure 9.5). The global stability state of the LES-generated ABL in the equilibrium limit was $-z_i/L \approx 8$ where L is the Obukhov length scale (see Wyngaard 2010). This moderately convective state is typical of the daytime ABL with winds for wind turbine power generation.

A low-dissipation pseudo-spectral algorithm was used in the horizontal and second-order central finite differencing applied in the vertical on a staggered grid. Dealiasing by truncation was applied in the horizontal so that the turbulence evolved on an effective 512 × 512 × 256 grid. Periodic boundary conditions on velocity and potential temperature were applied in the horizontal to model a statistically horizontally homogeneous ABL. A lower boundary condition for the total shear stress vector was applied using the "surface exchange" representation that has historically been the standard approach in ABL LES. At the top of the computational domain, the geostrophic wind velocity and mean temperature gradient were specified. The Coriolis force

parameter was chosen for midlatitudes and numerical stability was maintained with a fully explicit third-order Runge-Kutta variable time advance with fixed Courant number.

Given that wind turbines operate in response to the energy-dominant turbulence eddies within the ABL, it is important to understand the basic turbulence structure of the precursor LES, a mixture of convective and shear driven motions. Solar heating drives strong vertical motions that concentrate within atmospheric thermals separated by weaker and broader downward turbulent motions (Khanna and Brasseur 1998; Jayaraman and Brasseur 2021). These turbulent vertical motions are strongest in the "mixed layer," where strong mixing tends to homogenize mean temperature and, to a lesser extent, momentum. The strong vertical turbulent motions interact with strong horizontal turbulent motions in the surface layer below, in which shear-driven streamwise turbulent fluctuations concentrate within highly coherent streamwise-elongated turbulence eddy structures historically known as "streaks." The daytime ABL is typically capped by a stable "capping inversion" layer of height $z_i \sim 1000$ to 2000 m after noon that is related to the level of surface heat flux. The capping inversion defines the boundary layer thickness and confines the region of strong three-dimensional turbulence motions.

Figure 3 is an isocontour plot of the x-component of the fluctuating velocity (i.e., streamwise velocity relative to the mean) over a horizontal plane of 5 kilometers (km) × 5 km at one time instant taken from an LES at the hub-height level of the NREL 5-MW wind turbine, representative of the largest overland wind turbines (rotor diameter 126 m, 90-m hub height). This isocontour plane is well within the surface layer and shows clearly the low- and high-speed "streaks" as the turbulent-kinetic-energy (TKE)- dominant coherent eddy structure that generates the strongest nonsteady load responses on the wind turbine rotor. The turbulence Reynolds numbers are very high, so the highly unstable convective motions of the daytime ABL interact with the shear-driven motions to create streamwise-oriented "large-scale rolls" that span the depth of the boundary layer with roughly helical structure (Jayaraman and Brasseur 2021).

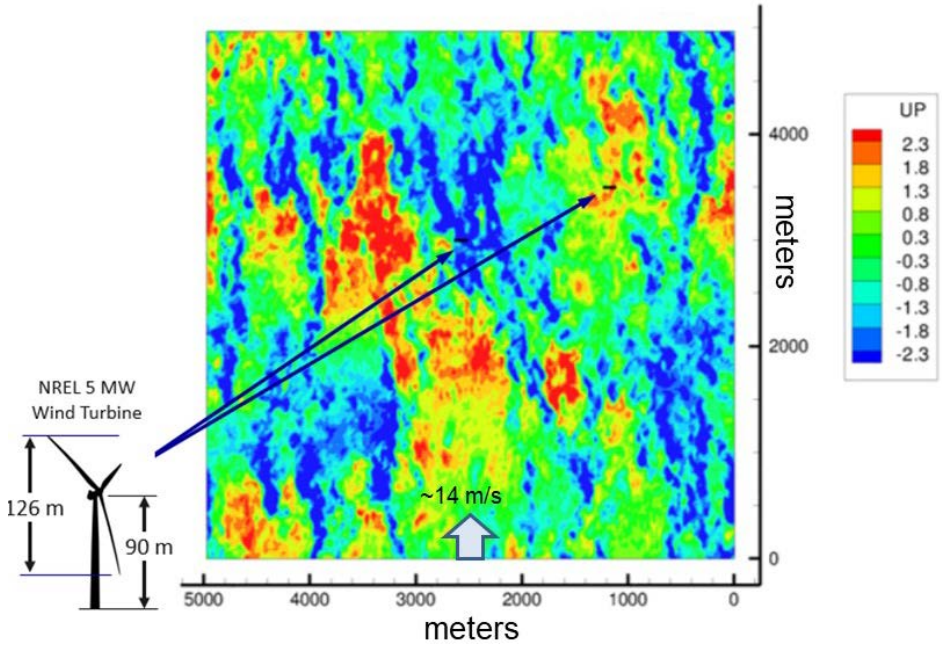

Figure 3. Isocontour plot of the streamwise fluctuating velocity component, *u*', from a LES of a canonical daytime atmospheric boundary layer at hub height for the NREL 5-MW wind turbine.

The blue regions ($u' < 0$) show coherent "low-speed streaks" which, as indicated by the black bars, have width of order the rotor diameter of the NREL 5-MW wind turbine. The red regions ($u' > 0$) show coherent structures with higher-than-average fluctuating velocity. The mean horizontal velocity at hub height is ~14 m/s and the stability state of the ABL is $-z_i/L \sim 8$, where $z_i \sim 1000$ m is the capping inversion height and L is the Obukhov scale. The image is from Vijayakumar et al. (2012) and is from the same simulation set used by Lavely (2017).

The strongest turbulent motions, the ones of particular importance to wind turbine response, are the coherent surface layer eddies shown in Figure 3. Whereas the vertical turbulence motions are created by buoyancy force, the horizontal turbulence motions are produced by the distortion of existing turbulence by strong mean shear-rate resulting from the necessary existence of mean wind relative to the ground where velocity is forced to zero. The energy-containing coherent surface-layer eddies are typically concentrated within the lower 200 to 400 m of the ABL, the region occupied by wind turbines and wind plants. Thus, wind turbines are directly forced in the daytime ABL from the passage of TKE-dominant turbulence streaks through the rotor with velocity differences across the rotor disk easily as high as 5 to 10 m/s (Aguasvivas et al. 2015; Vijayakumar et al. 2016) with a time-mean velocity difference typically of order 1 m/s between the lower and upper margins of the rotor disk. Gradients within the turbulence eddies dominate the spatial gradients over the rotor disk. The characteristic advective time scale for the passage of these energy-dominant turbulence eddies is of order 30 to 60 s (Lavely et al. 2014; Nandi et al. 2017).

The simulation underlying Figure 3 was used for the precursor LES underlying the computational experiments analyzed in the sections below. The mean velocity profile deviates from logarithmic in the surface layer due to the convective nature of the daytime ABL from the solar heating of the ground (see Wyngaard 2010). However, in the surface layer, mean shear rate is high relative to the mixed layer. Consequently, the turbulence eddies that dominate turbulent kinetic energy retain the streamwise-elongated “low-speed streak” structure given by the blue

regions in Figure 3, surrounded by the somewhat less coherent "high-speed regions" shown by the red and yellow colors. Thermals with concentrated vertical velocity fluctuations are strongly correlated with the low-speed streaks and penetrate to the upper boundary layer (Khanna and Brasseur 1998). These convective vertical motions interfere with the shear-driven horizontal turbulent motions to "fatten" the high-speed regions while extending, or minimally changing, the low-speed streaks depending on the global ABL stability state (Jayaraman and Brasseur 2021). An important observation from Figure 3 is that the low-speed streaks that pass through the rotor disk have characteristic transverse scales of order the diameter of the wind turbine rotor. ABL turbulence therefore creates the time changes in aerodynamic rotor loads at the rotor scale.

2.2 The Computational Experiment: NREL 5-MW Wind Turbine Within Large-Eddy Simulation of the Atmospheric Boundary Layer

Lavely (2017) embedded the NREL 5-MW wind turbine rotor (Jonkman, et al. 2009) within the precursor LES of the daytime ABL shown in Figure 3 using the ALM of wind turbine blades (Sorenson et al. 2002; Jha et al. 2016; Martinez-Tossas et al. 2017). In the ALM, each blade is resolved by a series of actuator points, each of which models a local airfoil section with specified airfoil shape and pitch. The net force on a blade segment represented by an actuator point is generated by a locally two-dimensional representation of the airfoil section as it interacts with the local velocity field obtained from the LES. The sectional force is approximated using empirical C_ℓ-α and C_d-α curves for the airfoil previously measured in a wind tunnel experiment in steady state. The predicted force vector is then spread over a spherical volume of specified size with Gaussian weighting that is included as a body force in the Navier-Stokes equation within the LES flow-field solver. This is a two-way coupled model that includes the generation of wake vorticity and induced velocity along the blade span, including the generation of wing-tip vortices from the presence of local lifting blade surfaces.

The ALM approach contrasts with a fully blade-boundary-layer-resolved simulation in which the extremely thin boundary layers on the rotor blades at very high chord Reynolds numbers must be resolved at the micron level while simultaneously resolving the rotor and ABL scales at hundreds of meters (Vijayakumar et al. 2016). This very costly and complex approach is generally impractical (Vijayakumar and Brasseur 2019). The ALM is also in contrast with the lower fidelity and less costly blade element momentum theory models. These apply one-way coupling and do not model the impacts of the rotating blades on the flowfield. It has been shown that the two-way coupled ALM is necessary to capture, moderately well, the nonsteady responses of the blade sectional loads (lift and drag) and the corresponding nonsteady responses of the moments on the manuscript (Lavely et al. 2014; Lavely 2017). In particular, blade element momentum theory does not capture the small-time-scale ramp-like transients predicted with the blade-boundary-layer-resolved simulations (Vijayakumar et al. 2016) as illustrated in Figure 2. Lavely (2017) applied the advanced ALM developed by Jha et al. (2016) with the Gaussian distribution volume radius ε proportional to the sectional blade chord, which is necessary to capture the load distribution toward the blade tip where the chord length rapidly decreases. Forty actuator points modeled the airfoil sections of each blade.

Lavely carried out a series of computational experiments to measure time variations in the load response on the rotor and, in particular, the moment components and axial force on the main shaft from the rotor hub of the NREL 5-MW wind turbine embedded within the high-fidelity LES of the daytime ABL of Figure 3. The ABL LES was carried out as a precursor simulation without the wind turbine with a code that has been used multiple times previously by multiple researchers for studies of ABL structure and dynamics.

From the precursor ABL LES using the pseudo-spectral algorithm, a plane of space-time-resolved velocity and potential temperature was extracted for application to a second LES as inflow Dirichlet boundary conditions. As described in Vijayakumar et al. (2010), this second simulation was developed within the OpenFOAM computational environment that applies the same equations and models as in the precursor LES, but using a fully physical-space finite volume algorithm. The domain is 480 m × 480 m × 250 m surrounding an ALM of the NREL 5-MW wind turbine rotor that is placed so that the incoming face is perpendicular to the mean velocity vector at hub height (90 m). The OpenFOAM domain grid was finer than the precursor so as to resolve the rotor blades with the ALM. The modeled blades rotated through the fixed grid in the OpenFOAM domain. Dirichlet boundary conditions are applied at the inflow plane using the precursor simulation. Zero-gradient (outflow) boundary conditions were applied on the downstream outflow plane, the side planes, and the top plane. The initial condition was obtained from the precursor simulation interpolated onto the higher-resolution grid within the OpenFOAM domain.

In the computational experiments, rotor speed and blade pitch were held steady for the NREL 5-MW wind turbine (Jonkman et al. 2009). From the precursor ABL LES, the hub-height mean wind velocity was 14.1 m/s. Although this wind speed is above the rated wind speed of 11.4 m/s, the controller was turned off, pitch was held fixed (11°), and the main shaft angular velocity was maintained constant at the rated rotor speed of 12.1 rpm (0.20 hertz [Hz]). Thus, 1P and 3P rotation periods were 4.96 s (0.2 Hz) and 1.65 s (0.6 Hz), respectively. Coning, yaw, and tilt angles were set to zero so that the flat rotor plane is maintained perpendicular to the horizontal mean wind velocity. Gravity is set to zero so that the quantified responses on the main shaft are entirely from the aerodynamic interactions between the space-time varying turbulent wind velocity field and the wind turbine blades and rotor.

2.3 Interaction Between Turbulence and Rotor To Generate Time-Varying Loads: Key Computational Results

The axial force (thrust) on the main shaft was calculated by summing the contributions from all actuator points and was output at each simulation time instant. In a similar way, the three components of the time-varying hub moment vector, $\mathbf{M_H} = M_{H_x}\mathbf{e}_x + \mathbf{M}_{\mathbf{H}_\perp}$ were output at each time instant, where M_{H_x} is the torque and $\mathbf{M}_{\mathbf{H}_\perp} = M_y\mathbf{e}_y + M_z\mathbf{e}_z$ is the net nontorque, or OOP, bending moment at the hub from the time-varying aerodynamic forces on the rotor blades generated by interaction with the turbulence eddies described in the previous section. As given in Eq. (1) and discussed in Section 1.1, $\mathbf{M}_{\mathbf{H}_\perp}(t)$ drives the time changes in the aerodynamic contributions to the time changes in bearing force, $\mathbf{F}_{bearing}(t)$. In addition, two parameters that

quantify temporal and spatial variations of the resolved horizontal velocity (u_x) over time were calculated for comparison with the thrust force, torque, and nontorque moment components acting on the main shaft. The data were collected over a period of 200 s, roughly 4 to 5 large-eddy passage times.

Centrally important results from this study are given in Figure 4, where we plot the time variation in torque component, M_{H_x}, and the magnitude of the OOP bending moment vector, $\left|\mathbf{M}_{\mathbf{H}_\perp}(t)\right|$, over the 200-s period, together with the time variations in main shaft thrust and two key flow variables that explain mechanisms, as will be discussed. In Figure 4, two timescales are immediately apparent in the torque, bending moment, and thrust loads acting on the main shaft: the 3P time variation with period 1.67 s (0.6 Hz) and the eddy passage time that, for this ABL, is ~50 to 60 s. The scale of Figure 4 is too coarse to observe the sub-second time scale discussed in Section 1.1 and shown in Figure 2. However, these short time variations become apparent when the time axis is appropriately expanded. To identify the trends in the three plots of Figure 4 without the 3P variations that create a strong well-defined peak in the frequency spectra, a low-pass filter was applied with a sharp spectral cutoff at 1/2 the 3P frequency of 0.6 Hz. The superposed low-pass-filtered signal is drawn with the red "trend" lines.

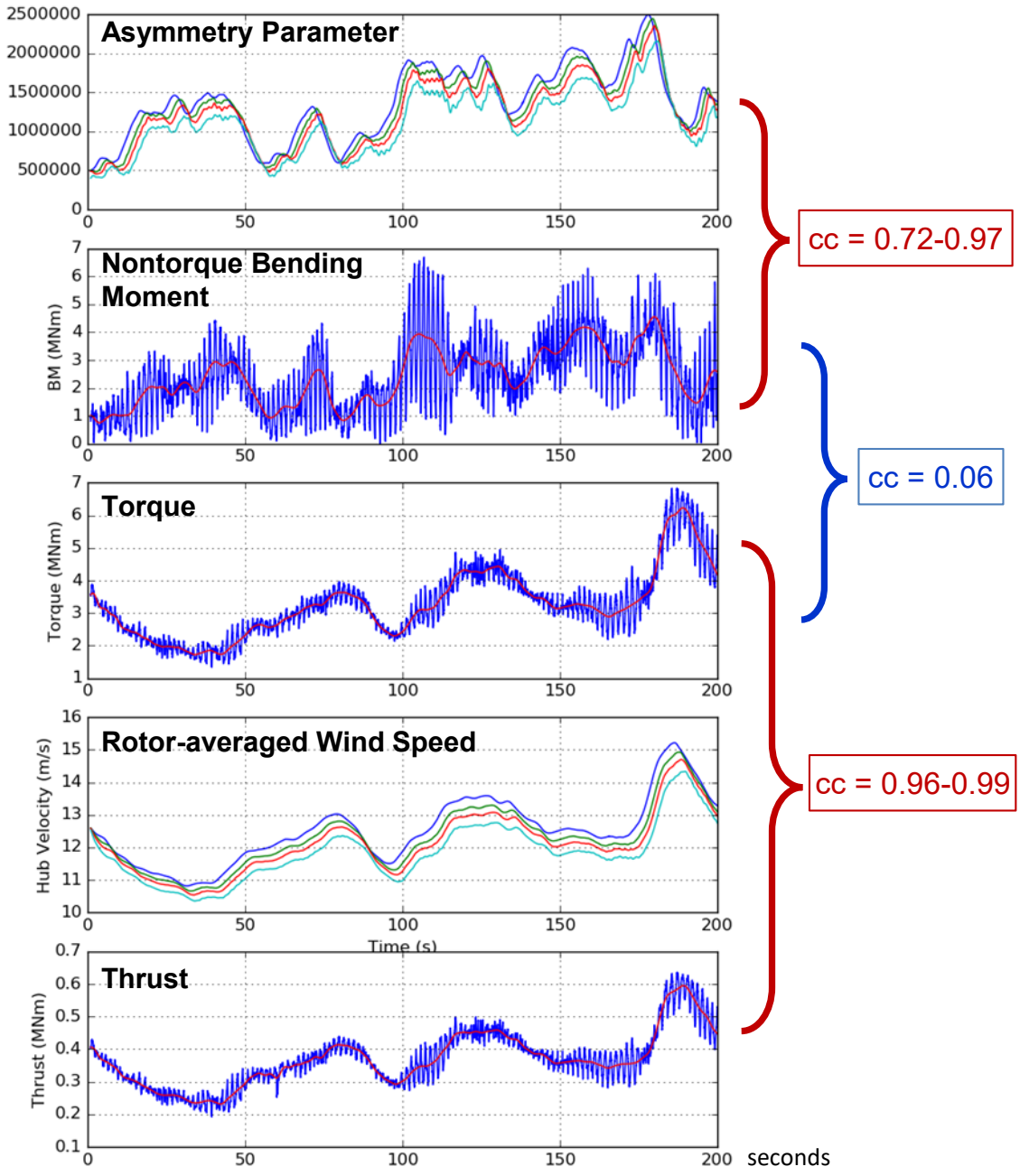

Figure 4. Key results from the computational experiments of the NREL 5-MW wind turbine, modeled using ALM embedded within a precursor LES of the daytime ABL.

Shown are signals from the Lavely (2017) simulation of the torque moment component and the magnitude of the nontorque, or OOP bending moment vector, acting on the main shaft from the rotor hub over a 200-s period in the stationary state. Also indicated are the (Pearson) correlation coefficients (cc) with the lower values using the full signal and the higher values using the moment signals after low-pass filtered below the 3P frequency. As indicated, torque and nontorque bending moment magnitude are uncorrelated in time. Two signals are well-correlated with torque: rotor-averaged horizontal wind speed and thrust (axial force on the main shaft). As described in the text, the temporal variations in the "asymmetry parameter" are well-correlated with nontorque bending moment.

An important result from the predictions in Figure 4 is that, over the 200-s time period of the simulation, the average magnitude of the OOP bending moment (which forces the main bearing)

is only 30% below that for torque, which underlies power generation. As importantly, Figure 4 indicates that the fluctuations around the trend line of the nontorque moment are much larger than those for torque, so that the main shaft bending moment is often as large or larger than torque, which is a consequence of the continual passage through the wind turbine rotor of the elongated energy-containing turbulence eddies within the daytime ABL. As will be shown in Sections 7 and 9, the comparable magnitudes of torque and OOP bending moment predicted with LES-ALM are confirmed with field data from the GE 1.5-MW wind turbine at the NREL Flatirons Campus. In the absence of turbulence eddies, the hub moment, $\mathbf{M}_\mathbf{H}$, would be nearly aligned with the axis of the main shaft driving power. We conclude, therefore, that the energy-containing eddying motions within the daytime ABL drive $\mathbf{M}_\mathbf{H}$ to be continuously off axis with sufficient strength that the OOP contribution of $\mathbf{M}_\mathbf{H}$ that creates nonsteady forcing of the main bearing function is of the same order as the axial component that is required for power generation. We shall return to this point in Sections 7.1, 9.2, and 10.2.

As illustrated in Figure 5, the 3P peak-to-peak variations in Figure 4 arise from nonsteady loadings that are generated by the rotation of the individual rotor blades through nonuniform concentrations of velocity fluctuation within the energy-dominant atmospheric turbulence eddies as they pass through the rotor plane (Vijayakumar et al. 2016; Vijayakumar and Brasseur 2019). Figure 5 shows isocontours of horizontal velocity over the rotor disk at two time instants during the transition from a low-speed streak covering the majority of the rotor plane (left) to the beginning of an extended period of high-speed flow (right). Such transitions are as illustrated visually in Figure 3 where highly elongated blue regions of low-speed fluctuations pass over a rotor disk followed by the passage of the more extended red regions of high-speed flow. As illustrated there, the lateral scale of the low-speed streaks is of order the rotor diameter, which is consistent with the color distributions in Figure 5. Given that the rotation period (5 s) is an order of magnitude smaller than large-eddy passage time (50 to 60 s), each rotor blade passes through an eddy of order 10 times while it passes through the rotor plane. Furthermore, in each rotation the blade commonly experiences multiple strong transverse gradients in horizontal velocity over length scales that are small compared to the rotor diameter with corresponding response times that are much smaller than the blade rotation period. The result is the subsecond ramp-like peak-to-peak variations shown in Figure 2.

In Figure 5 the blade has rotated twice during the transition period illustrated, a short 10-s period of relatively rapid change within the broader periods of blade rotation through high and low-speed large-eddy structures that pass through the rotor disk every 30 to 90 s (Lavely et al. 2014). Aerodynamic blade response varies with variations in the internal eddy structure during the many passages of wide ranges of eddy type and orientation relative to the rotor disk—variations that include differences in the relationships between vertical and horizontal velocity fluctuations (Section 2.1). Specifically, concentrations of buoyancy-driven vertical velocity fluctuations are strongly correlated with low-speed streaks (Khanna and Brasseur 1997; Jayaraman and Brasseur 2021), so as the rotor responds to transitions between high-speed and low-speed coherent structures, both the magnitude and the direction of wind velocity vectors change. As a low-speed streak sweeps through the rotor plane, for example, the velocity vector magnitude decreases

while the direction of the velocity vector orients more vertically in comparison to periods of high-speed eddy passage where the velocity vector is much more horizontally oriented with higher magnitude. These changes cause corresponding changes in the local angles of attack of velocity vectors relative to the rotating airfoil sections along the blade spans, which is the dominant contribution to changes in sectional lift and in blade loads (Vijayakumar et al. 2016).

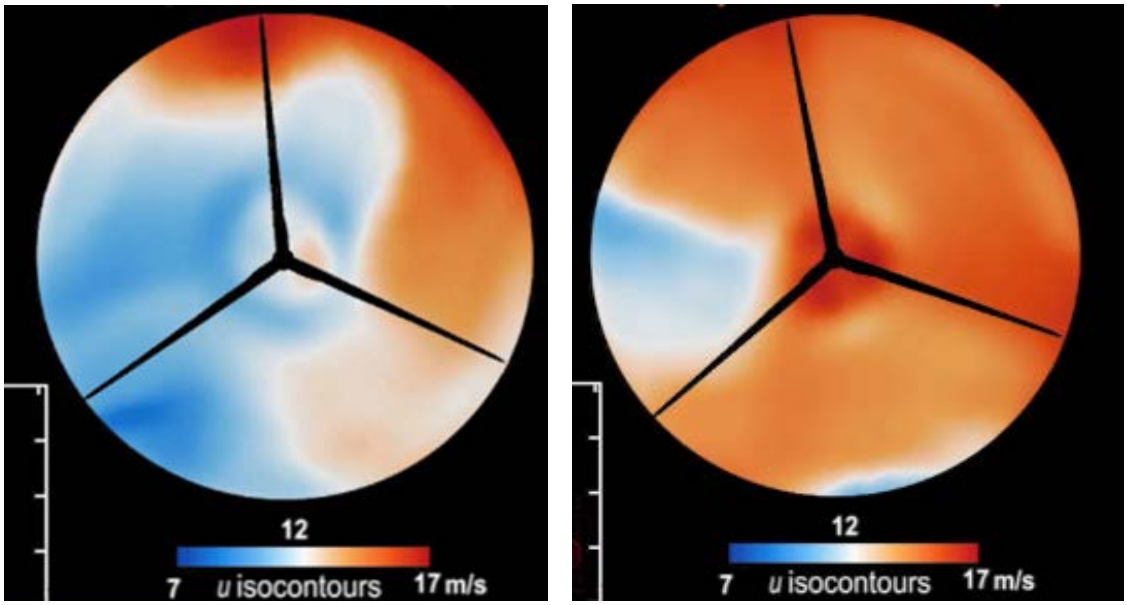

Figure 5. Example of the variation in horizontal velocity over the rotor plane from the latter period of low-speed streak passage (left) to the initiation of a period of high-speed flow (right).

The two plots are separated by 10 s (two blade rotations). These images are from an animation (Aguasvivas et al. 2015) using the data of Lavely (2017).

It is important to appreciate that these variations are not small. Note from Figure 5, for example, that LES of the 5-MW wind turbine within a typical daytime ABL produces horizontal velocity over the rotor plane that varies from 7 to 17 m/s, which is a large peak-to-peak variation of 10 m/s relative to a hub-height mean of 14 m/s, with corresponding variations in time. Whereas the shear parameter is often used to indicate the level of mean velocity variation across the rotor in the vertical, the movie from which Figure 5 was extracted (Aguasvivas et al. 2015) shows that the spatial and temporal variations in wind velocity through the rotor plane can far exceed the variations over the rotor plane described by the ensemble average wind profile, typically of order 1 m/s.

Note in Figure 4 that the temporal variations in the torque trend (red curves) look very different from the trend in the OOP bending moment. Similarly, the magnitudes in peak-to-peak fluctuations around the trend line are much lower for torque than for the OOP bending moment. Indeed, a key result from these simulations is that the torque and nontorque moments on the main shaft are *fully uncorrelated*; the cc computed in the 200-s period of Figure 4 is only 0.06. This key result indicates that the mechanisms underlying the generation of time variations in torque and mechanical power are fundamentally different from the mechanisms that generate the time variations in the main shaft bending moment magnitude.

Figure 4 shows that time changes in torque and thrust acting on the main shaft are *highly correlated* with time changes in the magnitude of the rotor-averaged wind velocity component normal to the rotor disk. The near-perfect correlation indicates that time changes in wind turbine mechanical power and thrust force on the main shaft are largely driven by time changes in the average magnitude of the normal velocity acting over the rotor plane. Rotor-normal velocity does not contain the 3P variations apparent in the main shaft loads. The near-perfect correlations are associated with near-perfect correspondence between the rotor-averaged wind speed and the trends in the load responses on the main shaft at time scales greater than the blade rotation period. As discussed above, these time changes in wind speed cause time changes in the angles-of-attack and lift on the blade airfoil sections, and, correspondingly, time changes in torque and thrust.

However, the time changes in rotor-averaged wind speed are unrelated to the time changes in the nontorque bending moment, as is clear from the cc's shown in Figure 4. This lack of correlation implies that the nonsteady changes in the nontorque bending moment are driven by a mechanism unrelated to average wind speed through the rotor plane. We discovered that the time changes in the magnitude of the OOP bending moment are instead driven by the *nonuniformity, or asymmetry, in the distribution* of the wind over the rotor plane. To show this quantitatively, we plot in Figure 4 the time variations of a parameter that is designed to quantify the degree of asymmetry in the rotor-normal velocity distribution between the three blades—what we refer to as the "triaxial asymmetry parameter," I_A (Lavely 2017). In a rotor-localized coordinate polar system with the origin at the hub, with *x* pointing along the main shaft axis (perpendicular to the rotor plane), and with (r,θ) within the rotor plane, I_A is defined by

$$I_A = \iint_{A_{rotor}} r\delta U_x dA \tag{3}$$

where

$$\delta U_x \equiv \max\left\{\left|u_x(r,\theta) - u_x(r,\theta+\frac{2\pi}{3})\right|, \left|u_x(r,\theta) - u_x(r,\theta-\frac{2\pi}{3})\right|\right\} \tag{4}$$

The integral in Eq. (3) is over the rotor disk area, A_{rotor}, where at each point the triaxial asymmetry velocity difference δU_x is multiplied by the moment arm *r*. In practice the integral is carried out over a grid on A_{rotor} using 1st-order quadrature. δU_x is chosen to quantify triaxial asymmetry at the point (r,θ) by choosing the larger of two differences in rotor-normal velocity between the point at *dA* and the two points located ±120° from *dA* at the same radial distance *r*. The inclusion of *r* in Eq. (3) mimics the inclusion of the moment arm *r* in the calculation of the moment at the hub, enhancing contributions from the outer extremities of the rotor disk.

Figure 4 shows that, like rotor-averaged wind speed, integration over the rotor disk removes 3P oscillations with resulting time variations that closely match the trend (the low-pass-filtered OOP bending moment). Correspondingly, the cc between $I_A(t)$ and the trend in nontorque bending moment is 0.97, whereas the cc with the full signal is 0.72. The implication is that asymmetric

distributions in the contributions to the OOP bending moment from each of the three blades are generated by the asymmetric distributions in rotor-normal velocity over the blades, especially in the outer regions of the rotor disk. To illustrate this, consider Figure 5 where the left image visually indicates much higher asymmetry than the right image, especially toward the outer margins of the rotor disk. The high correlation between $I_A(t)$ and $\left|\mathbf{M}_{\mathbf{H}_\perp}(t)\right|$ in Figure 4 implies that the OOP hub bending moment is much higher at the time corresponding to the left image than to the right image in Figure 5.

Time changes in the thrust and OOP bending moment produce axial and radial displacements of the main shaft with corresponding time changes in resisting forces on the main bearing. Consequently, mitigating strategies to reduce turbulence-induced nonsteady loadings on the main bearing must address the time-changes in rotor-normal velocity asymmetry over the rotor disk during the passage of atmospheric turbulence eddies through the rotor. As is especially apparent in the movie from which Figure 5 was obtained, and as quantified by the temporal variations in the asymmetry parameter shown in Figure 4, large changes in the asymmetrical distribution of normal velocity over the rotor disk take place during the passage of energy-containing turbulence eddies. The asymmetrical distribution occurs for two reasons: because the internal distribution of velocity within individual turbulence eddies is generally asymmetrical, and due to asymmetrical orientations of the eddies relative to the rotor disk. The temporal variations in the asymmetry parameter in Figure 4 show the imprint of the large-eddy passage time scale in the temporal variations of the asymmetry parameter. However, it is apparent that important frequency content is produced in the OOP bending moment signal from the same temporal changes in the asymmetry parameter that are independent of the temporal changes in the rotor-averaged wind speed, torque, and thrust signals. Furthermore, the passage of the blades through the internal transverse gradients in velocity within the individual eddies generate 3P responses in the nontorque bending moment that are much larger than the 3P variations in torque.

3 The NREL Wind Site as a Test Bed for Turbulence Eddy–Turbine Interactions

Given the importance of the key results described previously and obtained from computational experiments using LES of a 5-MW wind turbine model embedded within a canonical daytime ABL, there is a need to validate the characteristics and correlations shown in Figure 4 with field data. In what follows, we analyze data obtained from the GE 1.5-MW wind turbine and met tower at the NREL Flatirons Campus to the east of the eastern ridge of the Rocky Mountain Front Range. Because the westerly winds transport mountain-generated turbulence eddies over the wind turbine while northerly/southerly winds expose the wind turbine to the turbulence eddies embedded within the ABL, we are able to both validate and generalize the key result in Figure 4. We also compare analysis of the data from the anemometers on a met tower, where wind velocity is not impacted by the wind turbine, to the data from the nacelle anemometer a few meters downstream of the rotating rotor blades.

3.1 The Location of the Wind Site Relative to Mountains and Urban Areas

To validate the key computation-based results previously described and, more generally, to analyze the nonsteady responses to the passage of turbulence eddies through the rotor plane of a utility-scale wind turbine in the field, we analyze data collected from the GE 1.5-MW wind turbine at the NWTC on the NREL Flatirons Campus. As illustrated in Figure 6, this wind turbine is in a relatively flat terrain 4.5 to 5 km east of the well-defined north-south edge of the Front Range mountains about 10 km south of Boulder, Colorado. As the westerly winds carrying mountain-generated turbulence pass over the Front Range ridges, the turbulent flow separates to create highly turbulent separation eddies that are carried eastward toward the NWTC and through the rotor of the GE 1.5-MW wind turbine, as illustrated in Figure 6. The M5 met tower is 162.2 m to the west of the wind turbine. The time-resolved data from the met tower and wind turbine, instrumented as described in Section 4, are stored in 10-minute (min) segments. In section 6.1 we describe analysis of the anemometer-measured wind-speed data from the met tower to identify the 10-min periods where turbulence eddies are most likely to pass from the met tower to the wind turbine.

The NREL/GE wind turbine originated as a GE 1.5 SLE three-bladed horizontal-axis variable-pitch wind turbine with hub height of 80 m and nominal rotor diameter of 77 m (Santos and van Dam 2015). The rated wind speed is 14 m/s, the cut-in and cut-out speed are 3.5 m/s and 25 m/s, respectively. At rated wind speed the main shaft rotates at 18.3 rpm and the GE controller applies full span pitch control. The met tower was placed 276° from true north to measure westerly winds embedded with mountain eddies. Additional details are given in Sections 4.2 and 4.3. Figure 7 illustrates the location of the wind site relative to nearby urban areas. The GE 1.5-MW wind turbine is about 4.5 km to the east of the Front Range, 8 to 9 km south of the southern-most housing developments in Boulder, and 9 to 10 km north of the closest housing developments to the south. The nearest housing developments to the east are 8 to 9 km distant. There may be some impacts from urban areas for northerly and southerly winds; however, there is a reasonably

long fetch over which the relatively small eddies generated by single-family houses are dissipated.

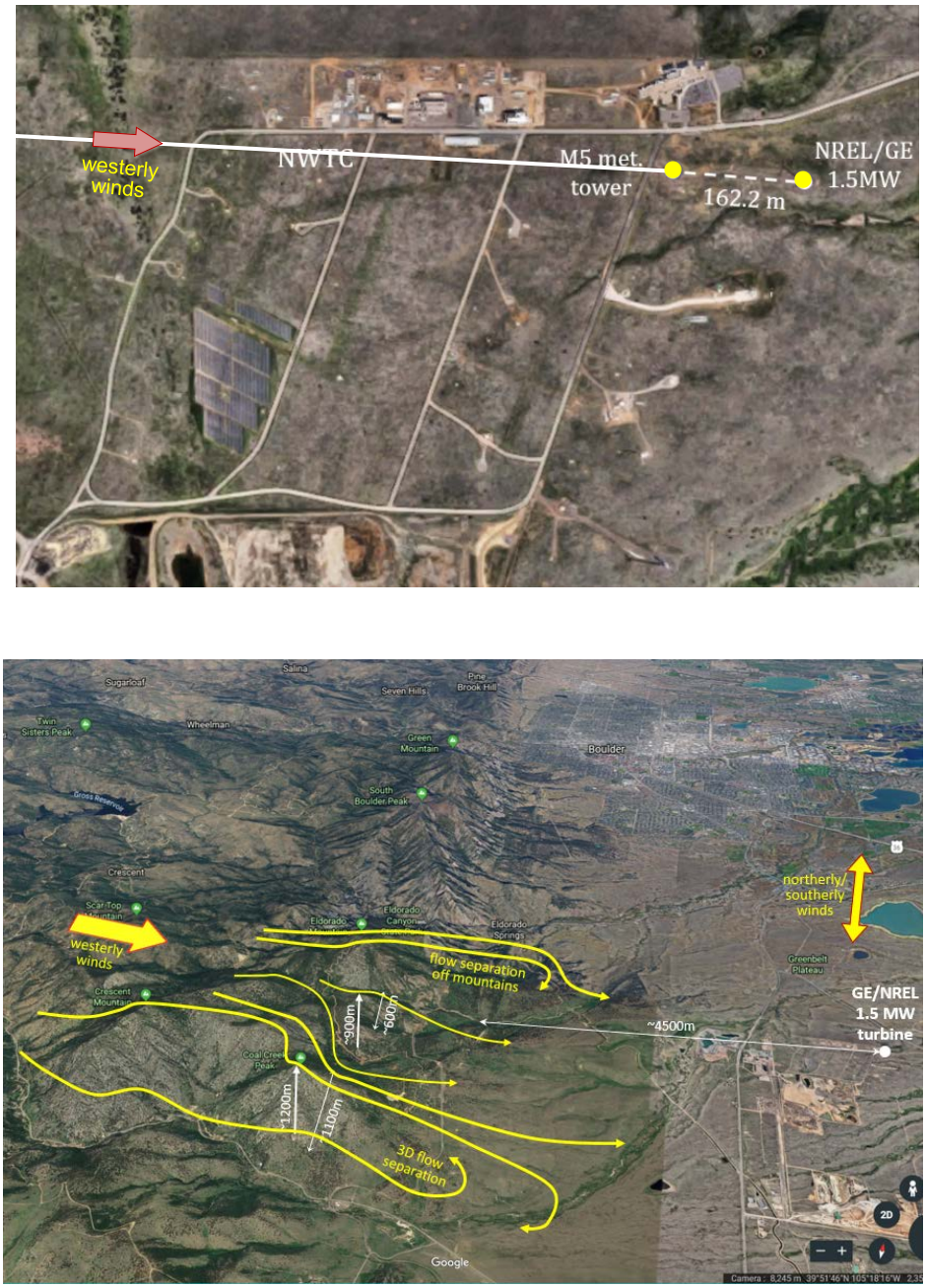

Figure 6. The National Wind Technology Center (NWTC) on NREL Flatirons Campus with the GE 1.5-MW wind turbine and M5 met tower (top) relative to the generation of mountain eddies (bottom).

The top image shows the location of the GE 1.5-MW wind turbine relative to the M5 met tower and the direction of the westerly winds. The bottom image illustrates the passage of mountain-generated turbulence eddies from the Front Range mountains 4.5-5 km to the west of the GE 1.5-MW wind turbine.

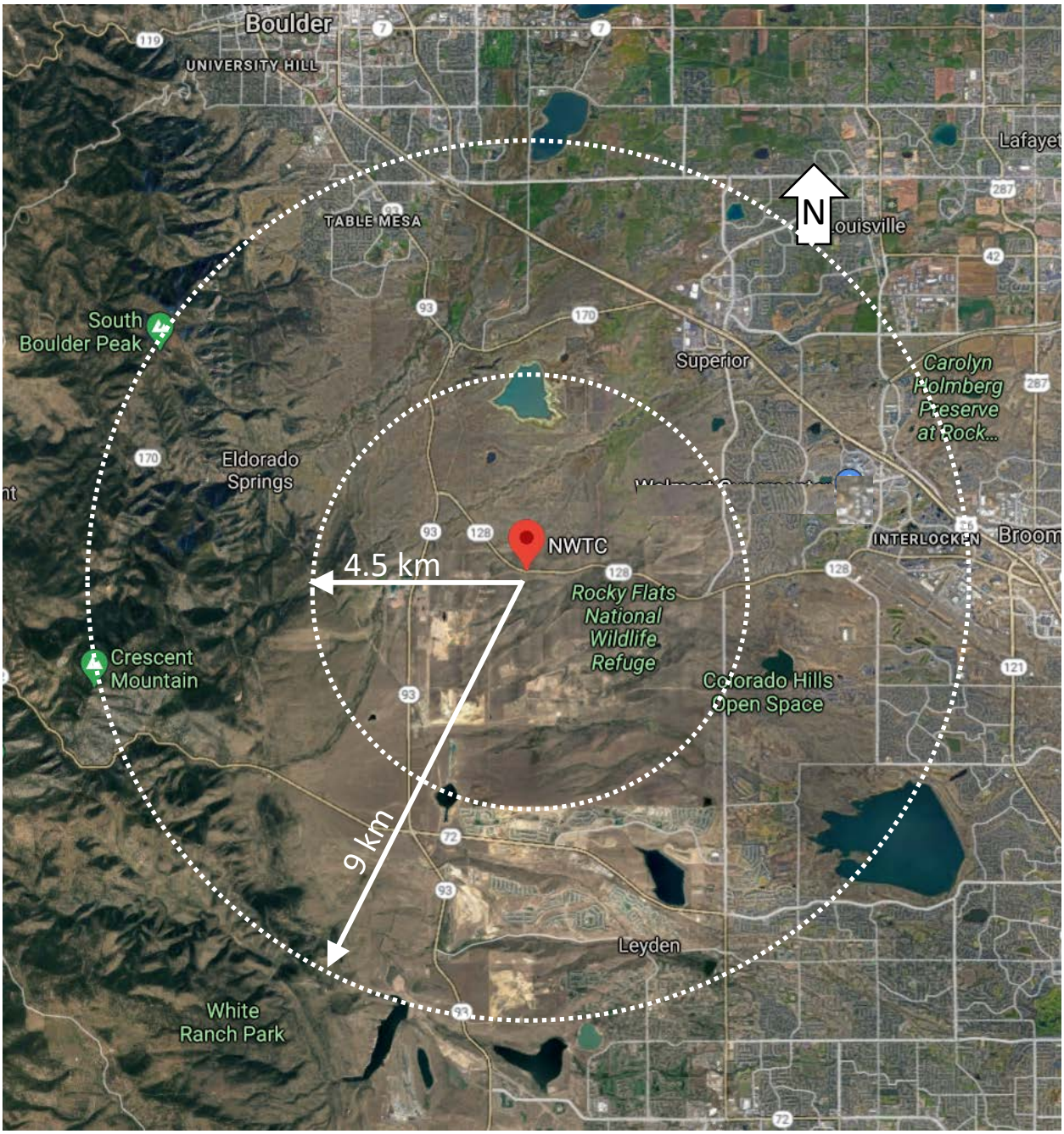

Figure 7. Location of the NWTC on the NREL Flatirons Campus relative to neighboring population centers and the Rocky Mountain Front Range

3.2 Relative Scales of the Mountain Eddies in Relationship to Atmospheric Eddies

Based on quantitative estimates from the Google Earth image in Figure 6, the peaks of the Front Range mountains ~5 km to the west of the GE 1.5-MW wind turbine are ~900 to 1200 m in height and ~600 to 1100 m in width. In Figure 8 we copy a figure from Hearst et al. (2016) in which a single cube is mounted on a flat plate with an active grid upstream to generate different

levels of free-stream turbulence outside a thick high Reynolds number flat plate turbulent boundary layer ($Re_x \sim 10^6$). Mounted more than 600 boundary layer thicknesses from the leading edge and active grid, the cube is embedded within a highly turbulent boundary layer of thickness roughly twice the cube height. Thus, the experiment characterizes the enhancement of the turbulent flow passing over a single obstacle qualitatively similar to the highly turbulent flow generated by the mountains to the west of the Front Range before passing over the Front Range peaks as illustrated in Figure 6 to generate the turbulence eddies that pass over the met tower and GE 1.5-MW wind turbine.

In the Hearst et al. experiments, the highly turbulent separated regions downstream of the obstacle reattach within two obstacle heights (Figure 5 of Hearst et al. 2016), which is consistent with experiments by Castro and Robbins (1977). Thus, we anticipate that the separated flow regions downstream of the Front Range mountains (Figure 6) reattach well upstream of the wind turbine, as illustrated in Figure 8 by the vertical dashed line at $x/h \approx 5$. Hearst et al. measured the integral scales of the turbulent flow upstream of the cube to be roughly 20% of the cube's height. Assuming that a similar scale ratio exists in the turbulent wake, we anticipate that the scale of the turbulence eddies approaching the GE 1.5-MW wind turbine downstream of the Front Range is of order 200 m in all three directions. Jayaraman and Brasseur (2021) used LES to quantify streamwise and vertical integral scales in a typical daytime moderately convective atmospheric boundary layer. They found that at 5% - 10% of the typical ABL height, roughly the hub height of the GE 1.5-MW and the NREL 5-MW wind turbines, the vertical integral scale is about 15%-20% of the ABL height. Because the transverse and vertical scales of the elongated atmospheric surface layer eddies are of the same order, we estimate that the typical transverse scales of daytime ABL eddies at hub height is ~200-300 m. This is also roughly the same scale that we estimate for the mountain-generated turbulence eddies.

The streamwise scale of the elongated eddies in the atmospheric surface layer is of order the boundary layer depth (Jayaraman and Brasseur 2021), roughly 3-4 times the transverse scales. However, we showed in Section 2.3 that the nonsteady responses of the hub moment, and therefore the bearing force (Eq. 1), is driven by the asymmetrical distribution of velocity over the rotor disk in the transverse and vertical directions. We conclude, therefore, that whereas the structure and streamwise length scale of atmospheric vs. mountain-generated eddies are different, the cross-stream scales of the turbulence eddies responsible for drivetrain load responses are roughly the same between the atmospheric and the mountain-generated eddies. Furthermore, for the GE 1.5-MW and NREL 5-MW wind turbines with rotor diameters of 77 m and 126 m, respectively, a large percentage of a blade likely responds to the passage of turbulence eddy, depending on the location of the eddy centroid relative to the rotor disk.

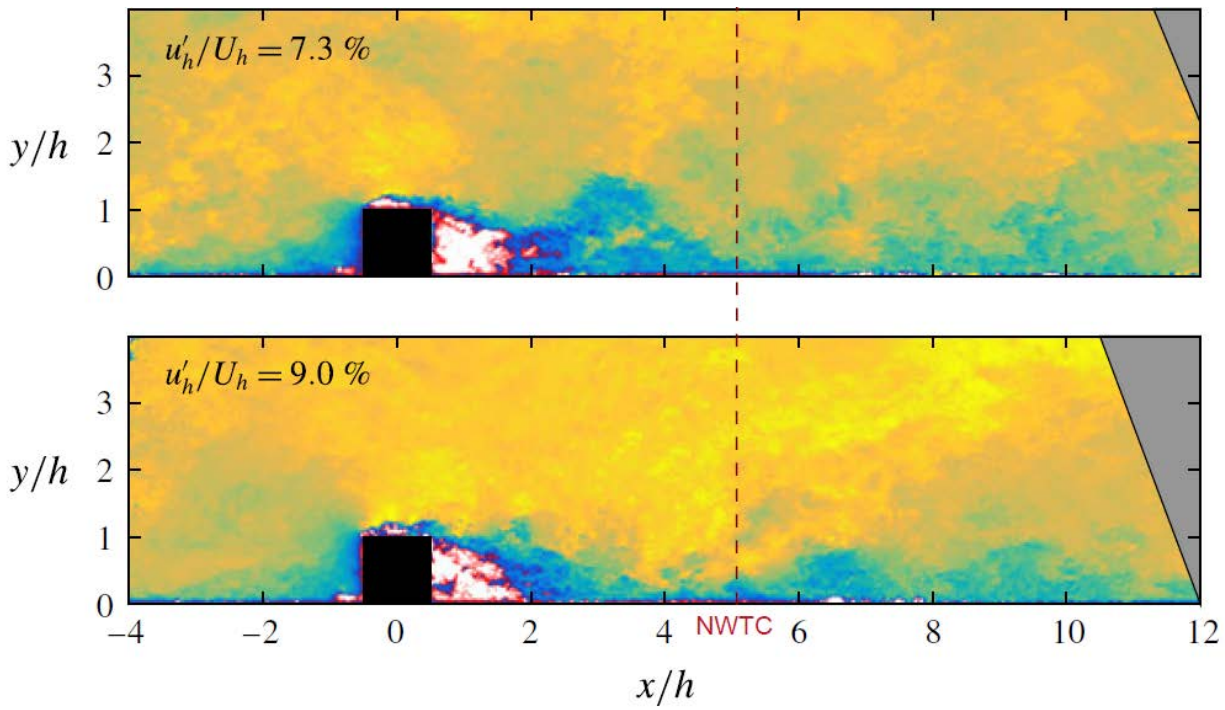

Figure 8. Measurement of instantaneous fluctuating streamwise velocity, u_h', behind a cube (black) mounted on a plate within a thick turbulent boundary layer. *Image from Hearst et al. (2016)*

The flat plate turbulent boundary layer is roughly twice the thickness of the cube. Measurements were made with particle image velocimetry with different levels of free-stream turbulence generated outside the boundary layer with an active grid at the turbulence intensity levels indicated. In the images, yellow is maximum, dark red is small negative, dark blue is small positive, and the black line between the red and blue regions indicates zero velocity. The figure is reproduced with permission from Cambridge University Press.

In addition to length scale, the time for the passage of mountain eddies through the rotor plane should be compared to the typical passage time of the elongated eddy structures through the wind turbine rotor plane. For the neutral and unstable ABL, Vijayakumar et al. (2012) used a structure-extraction technique to estimate the passage time of the low-speed streaks to be in the range of 40 to 100 s. In the current study we calculated the two-time autocorrelations of horizontal velocity at the met tower for datasets determined to most represent the passage of eddies from the met tower to the wind turbine and we estimated integral time scales. As will be described in Section 6, for the most probable eddy passage events we calculate a mean integral time scale of 36 s with a range of ~7 to 100 s. Based on previous experience with direct numerical simulation turbulence data analysis, the structure-extraction method produces estimates higher than the integral time scale, likely by factors of two or more. We therefore conclude that the passage time and scale of the mountain eddies are of the same order as the typical daytime atmospheric eddies that impact utility-scale wind turbines in flat terrain. This assessment is verified in Section 9 with field data.

4 Data Collection: GE 1.5-MW Wind Turbine and the Met Tower Instrumentation

4.1 The Period of Data Analysis and Data Collection

The data analyzed, collected from the GE 1.5-MW wind turbine and M5 met tower, were restricted to the 3-month period from June 14 through October 5, 2018 because the calibration factors for the blade #1 root bending moments are only valid in this period. Loads data were taken from the supervisory control and data acquisition (SCADA) data channels as well as from instrumentation installed by NREL on the wind turbine, as described in Section 4.3. The data analyzed were restricted to the period from 12:00 noon to 30 minutes prior to sunset because the ABL depth changes least rapidly during this period (Johansson et al. 2001) and can often be well-approximated as stationary. Datasets in which precipitation were recorded, either at the M5 met tower or at the Boulder Airport (BDU) weather station (ASOS Network 2019), were excluded from analysis.

4.2 The Met Tower Instrumentation

Figure 9 shows a schematic of the NREL M5 met tower situated 162.2 m to the west of the wind turbine at 276° from true north, along with a listing of the instrumentation mounted at different heights on the tower. This figure and Table 1 are a summary of the met tower instrumentation from Clifton (2014), which provides additional details (see also Clifton 2016). The cup anemometers measured horizontal wind speed, the vane anemometers measured the horizontal wind direction, and the sonic anemometers measured the three wind velocity components, all time resolved. Cup and vane anemometers were sampled at 1 Hz and the sonic anemometers were sampled at 20 Hz. The cup and vane data were upsampled to 20 Hz (by copying the data) and all data were stored at 20 Hz. Table 1 provides instrument details.

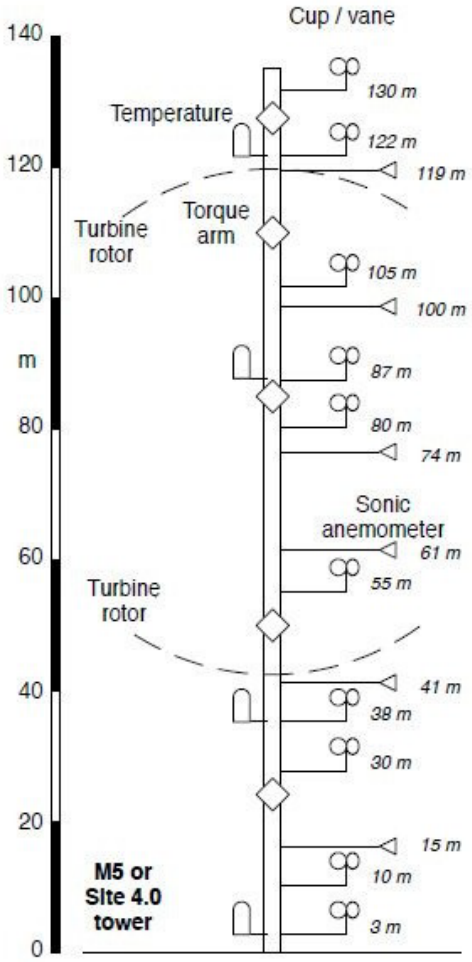

Height	Parameter	Boom
130	$WS(1)$	Short
122	$WD, WS, T_{dp}, \Delta T$	Short
119	Sonic u_x, u_y, u_z, T_s, accn	Long
105	$WS(1)$	Short
100	Sonic u_x, u_y, u_z, T_s, accn	Long
92	–	Short
90	–	Short
87	$WD, WS, T, T_{dp}, \Delta T$	Short
80	$WS(1)$	Short
74	Sonic u_x, u_y, u_z, T_s, accn	Long
61	Sonic u_x, u_y, u_z, T_s, accn	Long
55	$WS(1)$	Short
41	Sonic u_x, u_y, u_z, T_s, accn	Long
38	$WD, WS, T, T_{dp}, \Delta T$	Short
30	$WS(1)$	Short
15	Sonic u_x, u_y, u_z, T_s, accn	Long
10	WD, WS	Short
3	WD, WS, T, T_{dp}	Short
3	P, precip	N/A

Figure 9. Schematic and details of the instrumentation on the NREL M5 met tower.

For analysis of wind speed, only the cup anemometers were used. In the table, WS and WS(1) refer to wind speed measured by the cup anemometers and WD refers to wind direction measured with wind vanes. Many of the correlations between horizontal wind speed measured at the met tower and quantities measured on the wind turbine use the 80-m cup "hub anemometer." Data from the 74-m, 100-m, and 119-m sonics were not used. The images are from (Clifton 2014).

Table 1. Cup and Sonic Anemometers on the M5 Met Tower

Item	Meaning	Device	Range	Accuracy	Acquisition Rate
WS	Wind Speed	Met One SS-201 Cup Anemometer	0-90 m/s	0.5 m/s or 2%	1 Hz
WS(1)	Wind Speed, Class One	Thies 4.3351.1.10.0000	0-75 m/s	Not specified	1 Hz
WD	Wind Direction	Met One SD-201 Wind Vane	0-360 m/s	3.6°	1 Hz
u_x, u_y, u_z	Velocity Components	ATI K Type Sonic Anemometer	±30 m/s	0.01 m/s	20 Hz

The table is taken from (Clifton 2014).

The rotor-passage time scales for energy-dominant turbulence eddies in the ABL are sufficiently large that 1-Hz sampling is at least twice as high as necessary to resolve measurable fluctuations induced by the passage of turbulence eddies through the wind turbine rotor. This statement is based on analysis of the well-known frequency spectra measured in the surface layer of the daytime ABL by Kaimal et al. (1972) at heights relevant to wind turbine function. Specifically, the spectra bounding the grey region of Figure 4 of Kaimal et al. provides the range of spectra relevant to typical daytime atmospheric stability states at heights experienced by utility-scale wind turbines in flat terrain. We have argued in Section 3.2 that the length and time scales of the mountain eddies in the current study are consistent with typical daytime ABL eddies. The spectra are given as a function of the nondimensional frequency, $f^* = nz/U$, where n is the dimensional frequency, z is the height from the ground and U is the mean wind speed at z. The highest measurable frequencies associated with the energy-containing motions are, at most, an order of magnitude above the peaks in the measured spectra. Using the limiting spectra for $z \sim$ 100 m and $U \sim$ 15 m/s, one may estimate the highest potentially relevant frequency to be ~ 0.5 Hz, half the data-collection frequency of the cup and vane anemometers.

In summary, over individual data collection periods of 10 minutes, met tower velocity, and direction anemometers collect data at 1 Hz or 20 Hz and are stored continuously at 20 Hz. We shall use the term "datasets" to refer to these 10-min time-resolved data collection periods. Certain met-mast instruments, however, could not be used for various reasons. For example, sonic anemometer data are missing at 74 m, 100 m, and/or 119 m for some periods of the measurement campaign. Therefore, these instruments were never used. Instruments that are used (note that hub height is 80 m) include the cup and vane anemometers (Clifton 2014 and Clifton 2016), described in Table 1 and shown on the met tower in Figure 9. Note that two different types of cup anemometer are used on the M5 mast, a standard anemometer (Met One) and a "class one" anemometer (Thies), which has better specs (see Clifton 2014). Both stand-alone vanes and vanes coupled with cup anemometers are installed (mounted at opposite ends of a 1-m crossbar at the end of a "short" boom). The cups and vanes are not heated.

To identify turbulence eddies and some of the correlations between wind speed measured at the met tower and quantities measured on the wind turbine we use the class one 80-m cup anemometer, which we refer to as the "met tower hub anemometer." For the velocity averaged over the rotor plane, in key correlations, we use all anemometers on the met tower (along a line) identified in Figure 9 within the rotor plane. These include ATI 'K' Type sonic anemometers (Table 1) that collect data at 20 Hz. The vane anemometer at 87 m is used in the data analysis process. In addition, data analysis with the standard cup anemometer mounted on the wind turbine nacelle is compared with analysis using the hub anemometer on the met tower (Section 6.2.1) and in analysis of northerly/southerly winds (Section 9).

4.3 The GE 1.5-MW Wind Turbine and Instrumentation

As previously mentioned, the NREL/GE wind turbine is a GE 1.5 SLE, three-bladed horizontal-axis with variable pitch and hub height of 80 m with a rotor diameter of 77 m. The rated power of the GE 1.5-MW wind turbine occurs above its rated wind speed of 14 m/s at a rotor rotation

rate of 18.3 rpm. Figure 10 shows a schematic of instrumentation added to the wind turbine by NREL in addition to the standard SCADA data provided by the GE 1.5-MW wind turbine. Table 2 lists both SCADA and the NREL-added instrumentation on the wind turbine (Santos and van Dam 2015; Keller et al. 2019).

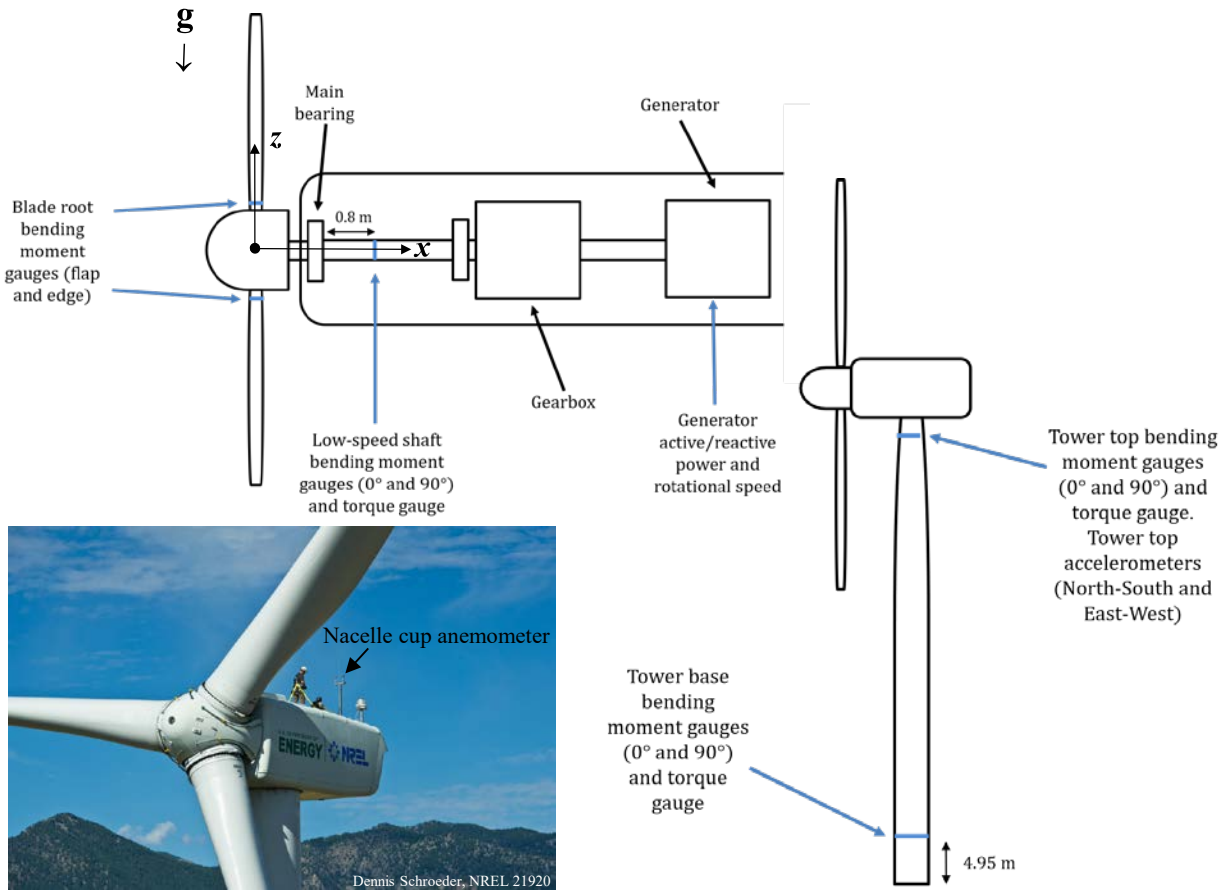

Figure 10. Schematic of NREL instrumentation on the GE 1.5-MW wind turbine blades and main shaft (left/top), on the tower (right) and on the nacelle (left/bottom)

The data channels specifically used in the current study are shown in Table 2. With the exception of the nacelle cup anemometer and yaw angle data used in the current study (Sections 8 and 9), the data analyzed in this study were collected from instrumentation installed by NREL. Other SCADA data were used indirectly. Specifically, time-resolved main shaft torque and OOP bending moment components from strain gauges mounted 0.8 m downwind from the main bearing (Figure 10) were analyzed in detail along with blade edge and flap bending moments measured at the blade root. The tower base bending moment vector magnitudes (TBMM) were measured 4.95 m from the tower bottom. The strain gauges were full bridges with matching strain gauges (Santos and van Dam 2015). The tower top bending moment signals were not analyzed. As discussed in Section 6.2.2, time changes in pitch angle were used to segregate data to develop correlations only during periods with negligible pitch changes so that pitch does not impact correlations.

Table 2. Data Channels in the GE 1.5-MW Wind Turbine Data Acquisition System

Source	Variable Name	Description	Sampling Frequency	Resampled Frequency
NREL	Active Power	Generator real power output	50 Hz	20 Hz
NREL	Blade_1_Edge	Edge bending moment, blade 1	50 Hz	20 Hz
NREL	Blade_1_Flap	Flap bending moment, blade 1	50 Hz	20 Hz
NREL	LSS_RPM	Main shaft rotational speed	50 Hz	20 Hz
NREL	Mainshaft_Downwind_Bend_0	Main shaft bending moment, rotating reference frame	50 Hz	20 Hz
NREL	Mainshaft_Downwind_Bend_90	Main shaft bending moment, rotating reference frame	50 Hz	20 Hz
NREL	Mainshaft_Downwind_Torque	Main shaft torque	50 Hz	20 Hz
SCADA	OPC_In_WindSpd	Nacelle wind speed from cup anemometer	1 Hz	20 Hz
NREL	Yaw Encoder	Nacelle yaw angle relative to true North	50 Hz	20 Hz
NREL	Pitch_Blade1	Pitch angle, blade 1	50 Hz	20 Hz
NREL	Tower_Base_Bend_1	Tower base bending moment	50 Hz	20 Hz
NREL	Tower_Base_Bend_2	Tower base bending moment	50 Hz	20 Hz

Except for the nacelle cup anemometer, all instruments were sampled and recorded at 50 Hz and down-sampled to 20 Hz using a Fourier low-pass hard filter for consistency with the met tower data, which were stored at 20 Hz. Like the met tower cup anemometer data, the nacelle cup anemometer was sampled at 1 Hz and upsampled to 20 Hz. Santos and van Dam (2015) discuss the calibrations for instrumentation on the GE 1.5-MW wind turbine. The calibrations used for the strain gauges to measure main shaft, tower, and blade root moments are given in Table 3 through Table 5. Calibrations for blades 2 and 3 strain gauges were not available or uncertain, so only blade 1 data were analyzed. Because calibration factors are only valid for blade 1 from June 14 to October 4, 2018, this period was chosen for analysis. To align the start of each rotation, rather than using the rotor azimuth angle from the data acquisition system (which was found to contain excessive noise at the start and end of revolutions), the main shaft speed was integrated in time.

Table 3. Main Shaft Strain Gage Calibration Coefficients

Channel	Slope (kNm/V)	Offset (V)	Valid From
LSS 0 Bending	1079.5	1.1782	6/14/2018
LSS 90 Bending	1079.5	1.6549	6/14/2018
LSS Torque	1274	1.1511	6/14/2018

kN·m = kilonewton-meter, V = volt

Table 4. Tower Base Strain Gage Calibration Coefficients

Channel	Slope (kNm/V/V)	Offset (V/V)	Valid From
Bending 1	4.9136×10^{7}	-2.5243×10^{-5}	1/1/2018 – 2/28/2019
Bending 2	4.8912×10^{7}	-3.0322×10^{-4}	1/1/2018 – 2/28/2019
Torque	4.8472×10^{7}	3.5438×10^{-5}	1/1/2018 – 2/28/2019

Table 5. Blade 1 Strain Gage Sensitivity Matrix

Channel	Flap (kNm/V/V)	Edge (kNm/V/V)	Valid From
Flap (kNm/V/V)	D1 = -2.19266×10^{6}	D2 = -3.35414×10^{5}	1/1/2018 – 11/30/2019
Edge (kNm/V/V)	D3 = -1.15853×10^{4}	D4 = -2.25393×10^{6}	1/1/2018 – 11/30/2019
Offsets (V/V)	$O_{flap} = -2.19447\times10^{-4}$	$O_{edge} = -3.48424\times10^{-5}$	1/1/2018 – 11/30/2019

4.4 Frequency Responses to Blade Passage

Figure 11 shows example mechanical power spectra with 1P and 3P frequency lines at rated wind speed drawn for blade flap and edge bending moments, and the main shaft torque and out-of-torque-plane bending moment vector magnitude. As discussed in Section 6.2.2, the measurements were made during periods before pitch was activated, which is well below rated wind speed (Figure 12). This is consistent with the spectra in which observed 1P/3P peaks are at frequencies largely below the rated values. Note that 1P peaks are identifiable for all bending moments (blade and main shaft) but torque, which is highly correlated with an integral over the rotor plane (Figure 4). Consequently, torque displays only 3P response. The 3P response is evident in both main shaft moment responses (torque and nontorque) but is not clearly evident in the blade moments because only strain gauges on a single blade were used.

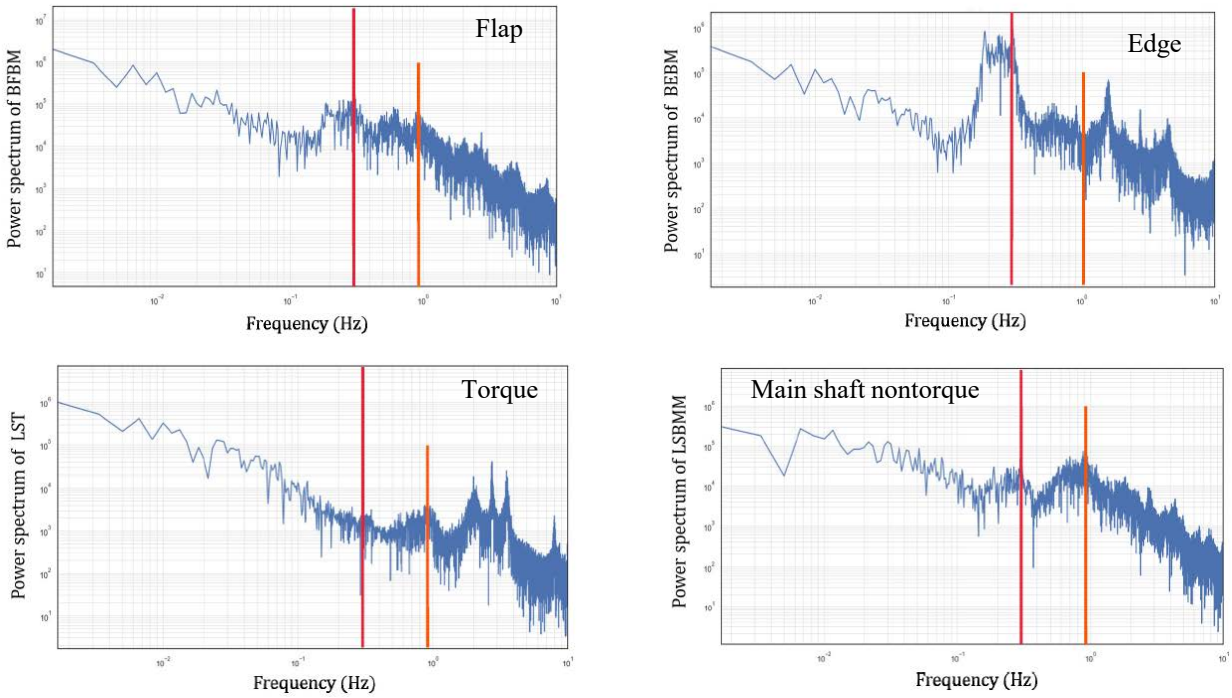

Figure 11. Example power spectra of blade flap bending moment (BFBM, top left), blade edge bending moment (BEBN, top right), main shaft torque (bottom left), and main shaft nontorque bending moment vector magnitude (bottom right).

The vertical lines indicate frequencies for 1P rotations (red, 0.305 rev/s) and 3P rotations (orange, 0.915 rev/s) if the wind turbine was operating at rated wind speed. During the periods when the data were collected, however, the rotor speed was below its rated value (Figure 12).

As shown in Figure 11, spectral responses to 1P and 3P blade rotations are spread out over relatively wide ranges of frequencies. We explored the application of stop-gap filtering to remove the signal surrounding the 1P and 3P peaks so as to isolate the non 1P or 3P contributions to the signal in our analysis. However, we concluded that the excessive broadness of the required filter leads to the removal of too much useful signal response, so no filtering was done on any data in the analysis.

5 Measured Classification Regimes of the GE 1.5-MW Wind Turbine

Given that our aim is to identify the aerodynamic responses of the wind turbine to nonsteady and spatially nonuniform variations in wind velocity over the rotor disk, we aim to minimize periods when wind turbine responses are not associated with wind variability. It is particularly important that the periods in which pitch response to the controller is measurable are not included in our analysis. It is necessary, therefore, to determine the thresholds in wind speed above which rotor speed is held constant and pitch control is initiated by the controller, in relationship to the transition from increasing to fixed wind turbine power with increasing wind speed.

Using the data reported in Table 2 and over the dates and time period described in Section 4.1, we plot in Figure 12 the power curve for the GE 1.5-MW wind turbine together with rotational speed of the rotor and main shaft, and the blade pitch angle. The nominal rated wind speed is reported to be 14 m/s at a peak power of 1.5 MW. These numbers are slightly higher than the measured rated wind speed of 13.7 m/s at maximum measured power of 1.46 MW. Pitch is observed to initiate at ~10 m/s, well below rated peak wind speed and power. Rotor speed goes constant slightly above initiation of pitch, at about 10.5 m/s, again well below rated wind speed and power. We conclude that the controller will interfere with the response to the passage of atmospheric eddies above about ~10 m/s and that phase 3 (maximum power) initiates well above the initiation of pitch control to maintain constant rotor speed.

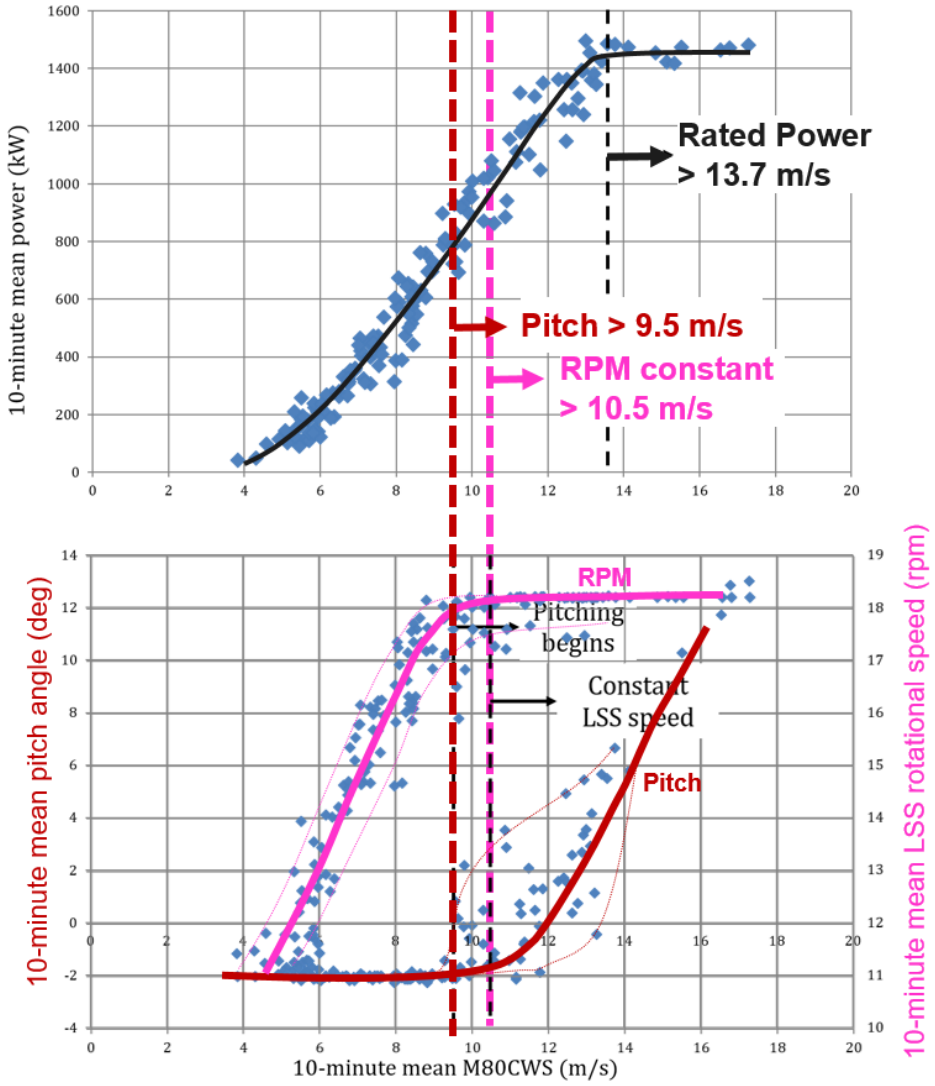

Figure 12. Regimes for the GE 1.5-MW wind turbine based on data over the period of analysis.

Measured power curve consistent with reported cut-in speed of 3.5 m/s and rated wind speed and initiation of regime 3 at 14 m/s. The data show that the transition to variable pitch and constant rotor speed begins near 10 m/s, well below rated wind speed.

6 Identification and Character of the Westerly Mountain-Generated Turbulence Eddies at the Wind Turbine

6.1 Passage of Individual Turbulence Eddies From the Met tower to the Wind Turbine

In Figure 13 we define four wind directions. For a 10-min dataset to be classified, we require that a minimum of 96% of the 10-min data collection was in the specified direction boundaries, where wind direction is measured with the 87-m met tower vane (Figure 9). We define westerly winds as winds ±45° from due west and northerly/southerly winds as within the 15° from true north or south toward the west and 45° from true north/south to the east. There were 139 datasets that satisfied the criterion for "westerly" and 33 for "northerly/southerly" (26 northerly, 7 southerly). Very few datasets satisfied the 96% criterion for easterly winds. As previously mentioned, datasets in which precipitation was recorded were excluded from the analysis.

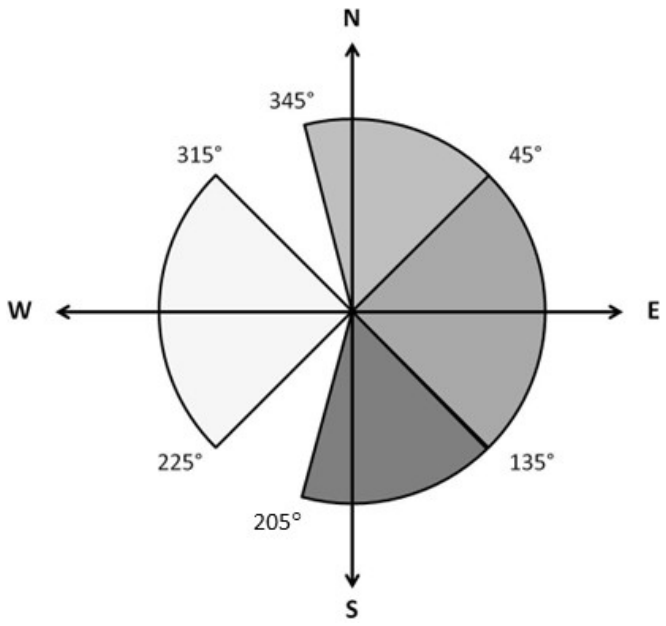

Figure 13. Definition of bins for classification of wind direction

A key element in our analysis of westerly winds is the segregation of the westerly datasets into those with a high probability of containing mountain-generated turbulence eddies that pass from the met tower through the wind turbine rotor. To identify such eddies, we search for time variations in horizontal velocity measured at the met tower with a similar signature in the horizontal velocity measured by the nacelle anemometer shifted in time consistent with transport by the mean wind. We search for eddies that, during the period of transport by the mean wind (~10 to 35 s), have not seriously changed in structure so that the eddy's velocity signature will correlate maximally when time is shifted appropriately to account for advection between the met tower and nacelle anemometers. Specifically, we calculate the cc between the horizontal velocities measured by the hub-height cup anemometer on the met tower and wind turbine

nacelle cup anemometer as a function of time shift, τ, between the two signals: cc(τ). The cc is calculated over the period of overlap between the two signals after time shifting (10 minutes minus time shift). Examples are shown in Figure 14 and Figure 15. In Figure 14(a) cc's are plotted as a function of τ for the two signals shown in Figure 14(b), where the tower signal has been shifted by τ_{crit}, determined by the peak in the correlation curve. Figure 14 is an example of good correlation where the cc reaches a max cc of 0.84 at a critical time shift τ_{crit} = 13 s, which is consistent with a 10-min average wind speed of 12.5 m/s. Figure 15 is an example of poor max cc (0.28) with an unphysical negative critical time shift of τ_{crit} = -24 s.

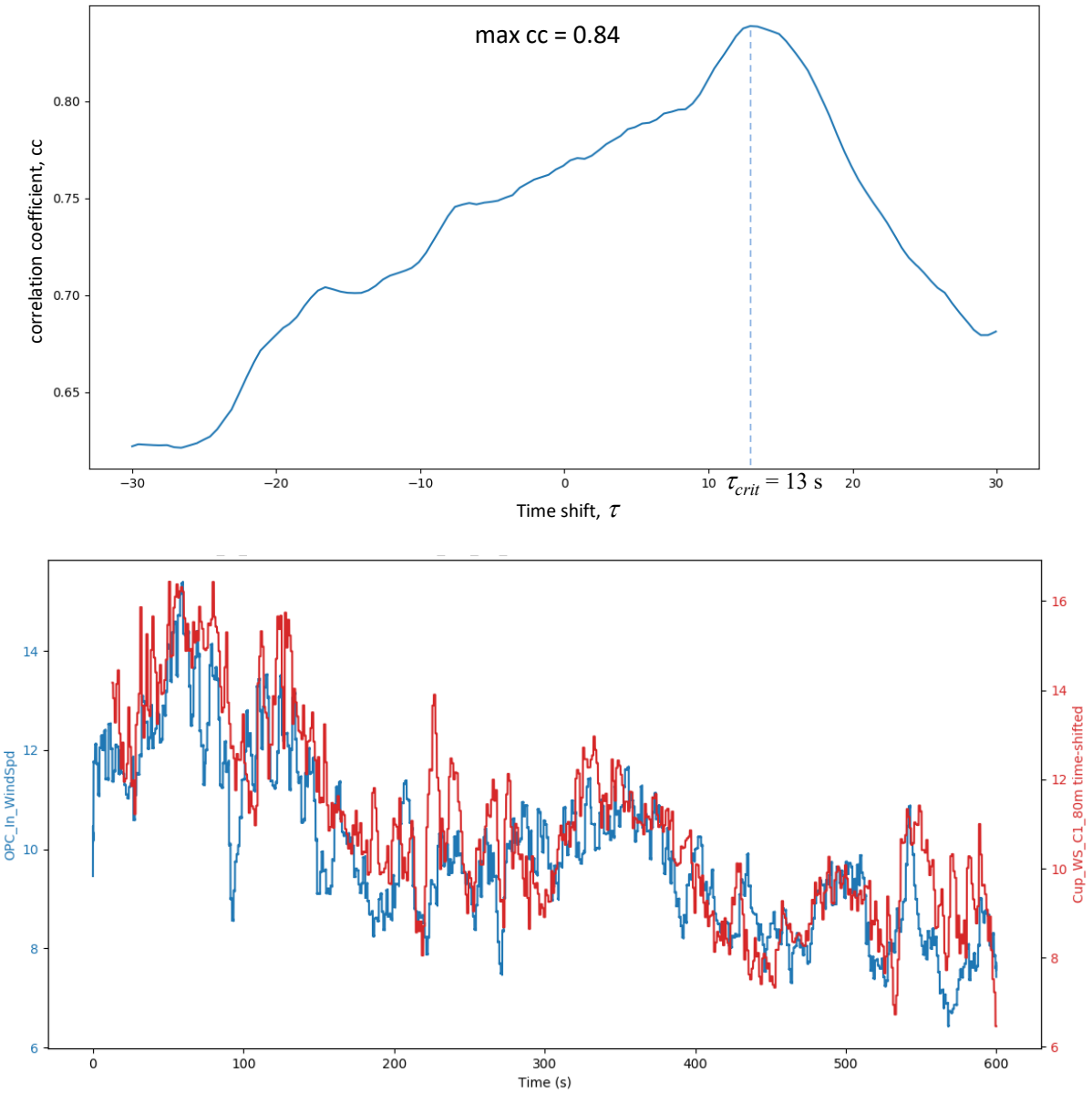

Figure 14. Example of optimal time shift between 10-min signals from the met tower hub anemometer (M80CWS) and the nacelle anemometer (OPC) for a signal that correlates well.

The upper plot gives the correlation coefficient versus time shift, cc(τ), for the pairs of signals shown in the lower plot, where the horizontal wind velocity measured at the met tower is shifted by the peak time shift τ_{max}. For these signal pairs, the maximum cc = 0.84 at time shift τ_{max} = 13 s.

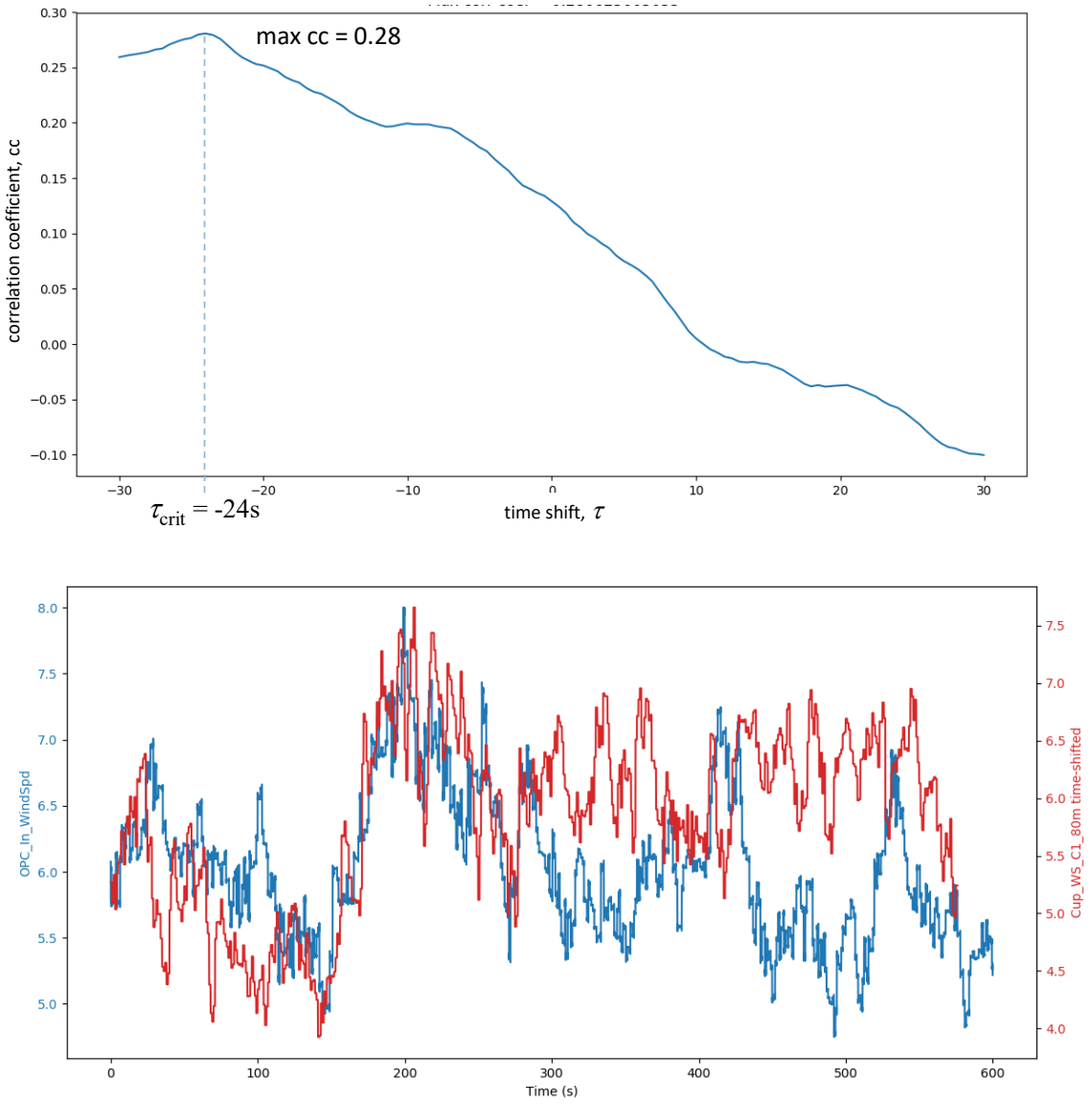

Figure 15. Example of optimal time shift between 10-min signals from the met tower hub anemometer (M80CWS) and nacelle anemometer (OPC) for a signal that does not correlate well.

The upper plot shows the correlation coefficient versus time shift, cc(τ), for the pairs of signals shown in the lower plot, where the horizontal wind velocity measured at the met tower is shifted by the peak time shift τ_{crit}. For these signal pairs, max cc = 0.28 at the unphysical time shift τ_{crit} = --24 s.

Figure 16 is a plot of 132 points with each point representing one of the 132 westerly datasets. Not all the cc(τ) curves are as well-defined as the two examples in Figures 14 and 15; for each dataset the critical time shift plotted on the *x*-axis is defined as the first peak in the time-shifted cc curve on the positive τ axis. Seven datasets from the original 139 westerly datasets produced negative critical time shift times; because these datasets cannot represent eddy passage from met tower to wind turbine they are excluded from the analysis. The *y*-axis defines the advection time for the turbulence fluctuations in the wind to be transported with the 10-min-averaged mean horizontal wind speed between the met tower and wind turbine rotor for the dataset that the point identifies. The mean of all 132 cc's for the shifted time series was 0.713, with a highly skewed

distribution that peaks at about 0.8, contains correlations as high as 0.95, and with a long tail to the lowest cc value of ~0.2.

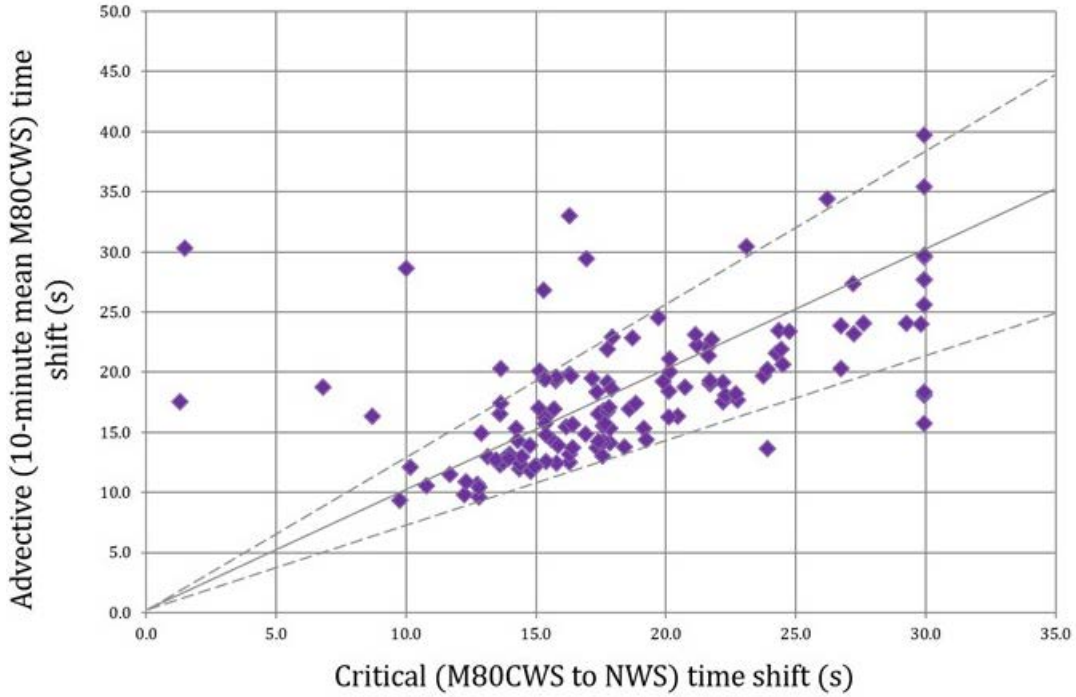

Figure 16. Critical time shift plotted against the advection time between the met tower and the wind turbine for each 10-min dataset period for all 132 westerly datasets that satisfy the criterion for critical time shift.

Advection time is based on the 10-min average in hub-height horizontal velocity at the met tower. The solid line shows perfect correspondence between critical time shift and advective time. The dashed lines show 9% deviation from perfect correspondence in either direction. The cc for the 132 dataset periods in this figure is 0.418.

6.2 Segregation of Datasets for Most Probable Eddy Passage Events

There were many datasets in which the magnitude of the peak correlation did not subjectively correspond to the visual quality of the overlap between the two signals. This happened for a variety of reasons that include:

- the presence of mixed eddy types in the 10-min data period,
- angulation of the 10-min-average mean velocity relative to the wind turbine so the eddy did not pass directly to the wind turbine,
- because the eddy was moving with an excessively low 10-minute-average velocity so that time for advection exceeded its correlation limit and the eddy changed significantly as it passed from met tower to wind turbine.

Here we develop methods to objectively segregate the datasets to create a subset of the 132 data points in Figure 15 with the highest probability of representing the passage of an eddy from the met tower to the wind turbine rotor.

6.2.1 High Misalignment and Low Wind Speed

The likelihood that an eddy that passes the met tower has missed the wind turbine increases as the direction of the 10-min-averaged velocity at the met tower, $\mathbf{U}_{10} = U_{10}\mathbf{e}_{10}$, deviates farther from the line between the met tower and the wind turbine hub (tower-hub axis). We demonstrate this relationship in the upper plot in Figure 17, where we identify in red those datasets in which $\mathbf{e}_{10}$ deviates by more than 23° from the tower-hub axis, and in yellow where $\mathbf{e}_{10}$ is within 3° of the tower-hub axis. We observe that the red points include five of the outliers in Figure 15.

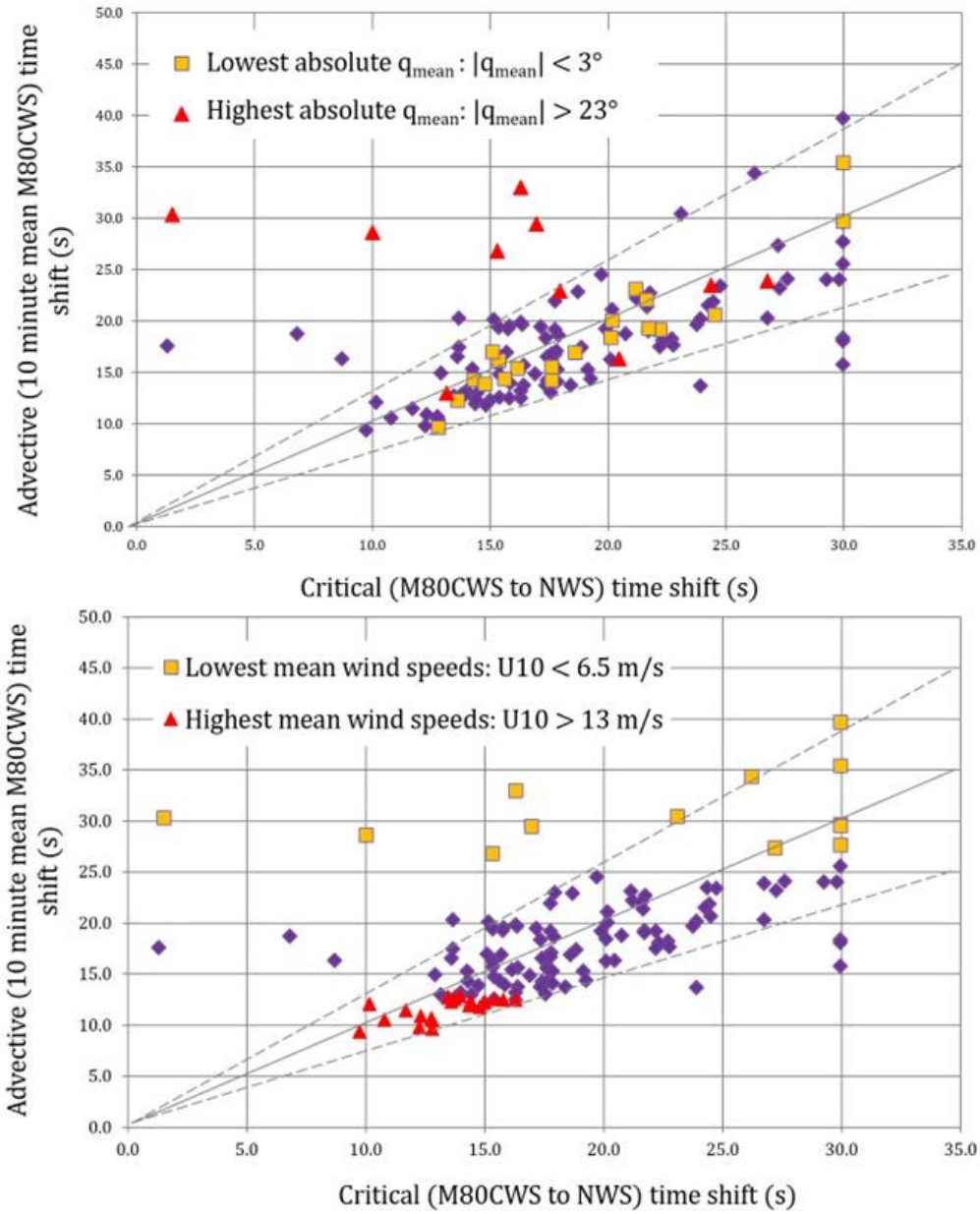

Figure 17. Impacts of 10-min mean wind orientation angle and mean wind speed on the location of potential outlier points in Figure 16.

The top figure shows 10-min dataset periods with high vs. low mean angle (q_{mean}) from the line drawn between the met tower and wind turbine hub, where q_{mean} is an average over all the wind vanes on the met tower. The bottom figure shows 10-min dataset periods with low vs. high average wind speed (U_{10}) at the met tower hub anemometer.

We also argue that when eddies advect from the met tower to the wind turbine with an average velocity that is of order or below the local eddy turnover time, the structure of the turbulent velocity fluctuations within the eddy will have changed significantly between the two. As a result, the forcing that led to the responses measured with sensors on the wind turbine will not be well-characterized by the velocity fluctuations measured at the met tower, appropriately shifted in time. This is demonstrated in the lower plot of Figure 17, where the same five outlier points associated with misalignment in the upper plot of Figure 17 are identified by the yellow square points. However, each of these figures also show other points that should be removed from the analysis based on poor alignment or low mean velocity.

We therefore combined these two arguments into a single algorithm to down-select from the 132 datasets in Figure 16. The algorithm aims to extract datasets with the highest probability of representing turbulence eddies that have been transported from the met tower to the wind turbine with the 10-min-averaged mean wind with relatively little change in turbulence structure. Having experimented with different methods and parameter variations, we applied the following algorithm to down-select from the 132 datasets displayed in Figure 16:

1. Rank all datasets by U_{10} (low to high).
2. Rank all datasets by q_{mean} (high to low).
3. Remove any datasets that occur in the top five of either list (1) or (2).
4. Remove any datasets that occur in the top 25 of both lists (1) and (2).

In the second step, q_{mean} is defined as the wind direction relative to the mean wind direction, (equivalent to the axis perpendicular to the rotor disk), averaged over all wind vanes on the met tower (Figure 9) and averaged over the 10-min period for that dataset. The procedure just described reduced the number of datasets for analysis from 132 (Figure 16) to the 109 datasets shown in Figure 18. Correspondingly, the cc between the advective time and critical time shift increased to 0.706 from the previous value of 0.418.

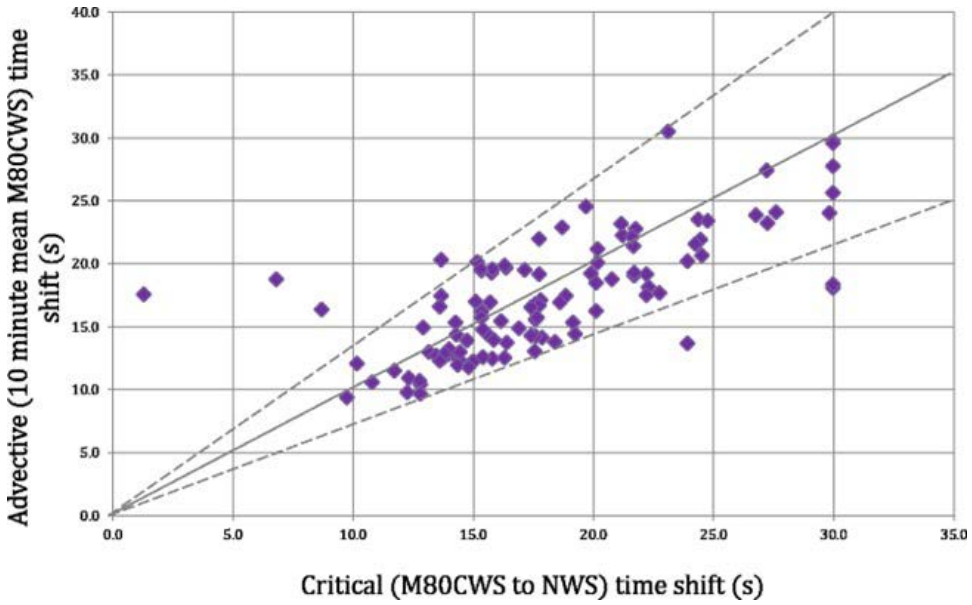

Figure 18. The points remaining from Figure 16 after the algorithm to remove datasets with both excessively high orientation angle and excessively low wind speed.

After the algorithm was applied, the 109 dataset periods shown in this figure remained from the original 132 in Figure 16. The cc for the points on this plot is 0.706.

6.2.2 Impacts of Pitch

Figure 12 shows that pitch control initiates above 9.6 m/s as given by the blade pitch angle, $\beta(t)$. It is likely that pitch control will strongly interfere with correlations established between temporal variations in the wind velocity over the rotor and the time variations in aerodynamic loads over the rotor blades. We therefore explore the likelihood that wind turbine response is strongly impacted by pitch control events and we develop criteria to remove datasets with significant impact.

Given that pitch control is manifested by time change in pitch angle, $\beta(t)$, we identify a "pitch control event" by the magnitude of $d\beta/dt$ (rather than by the pitch angle). We aim to remove datasets with excessive numbers of pitch control events in the 10-min dataset period. With careful examination of the 20-Hz $\beta(t)$ signals, we find that during 10-min data collection periods there exist continual excessively low-level time changes in β that arise from instrumentation noise in the range of 0.1 to 0.2°/s. This is shown in Figure 19, where we plot the binned distribution of $d\beta/dt$ over the 132 westerly datasets of Figure 16. From this pdf, together with careful analysis of time series of $\beta(t)$, we chose $|d\beta/dt| > 0.25$°/s to define a "pitch control event."

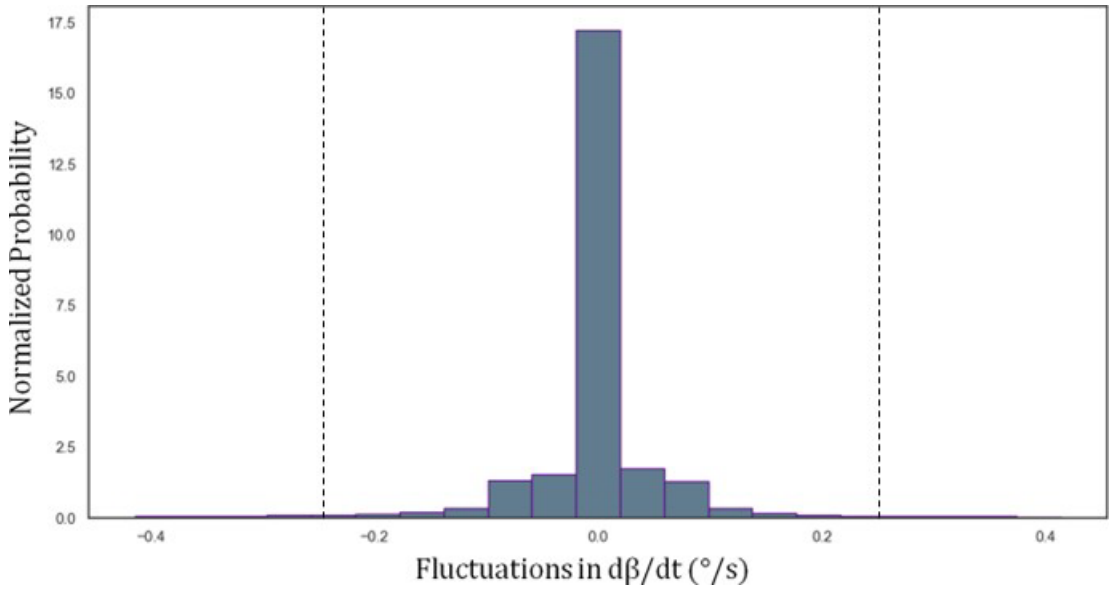

Figure 19. PDF of the rate of change in pitch angle over all 132 westerly 10-min datasets.

The datasets with pitch angle rate change magnitudes outside the two dashed lines (±0.25 °/s) are excluded from the analysis.

To demonstrate the impact of pitch control on the response of wind turbine loads to the passage of turbulence eddies through the rotor plane, we plot in Figure 20 the cc's between blade flap and TBMMs and the time-shifted velocity measured by the tower hub anemometer vs. velocity measured by the nacelle anemometer. In Section 8 we shall find that these two sets of cc measurements are, themselves, well-correlated. In Figure 20 the points are colored according to the number of pitch control events in the 10-min dataset period, as defined previously, where it is clear that increasing numbers of pitch control events in the 10-min sample period are associated with decreasing cc. In fact, the cc becomes negative when the number of pitch control events exceeds ~1000. This is shown explicitly in Figure 21, where the cc between velocity measured at the tower and time-shifted to the wind turbine and the blade flap and tower based bending moment magnitudes are plotted against the number of pitch control events in the 10-min dataset. We observe that in both cases the cc becomes negative when the number of pitch control events exceeds 1000 per 10-min data sample period. We therefore choose the criterion that datasets in which the number of pitch control events exceeds 1000 over the 10-min period of that dataset are excluded from further analysis.

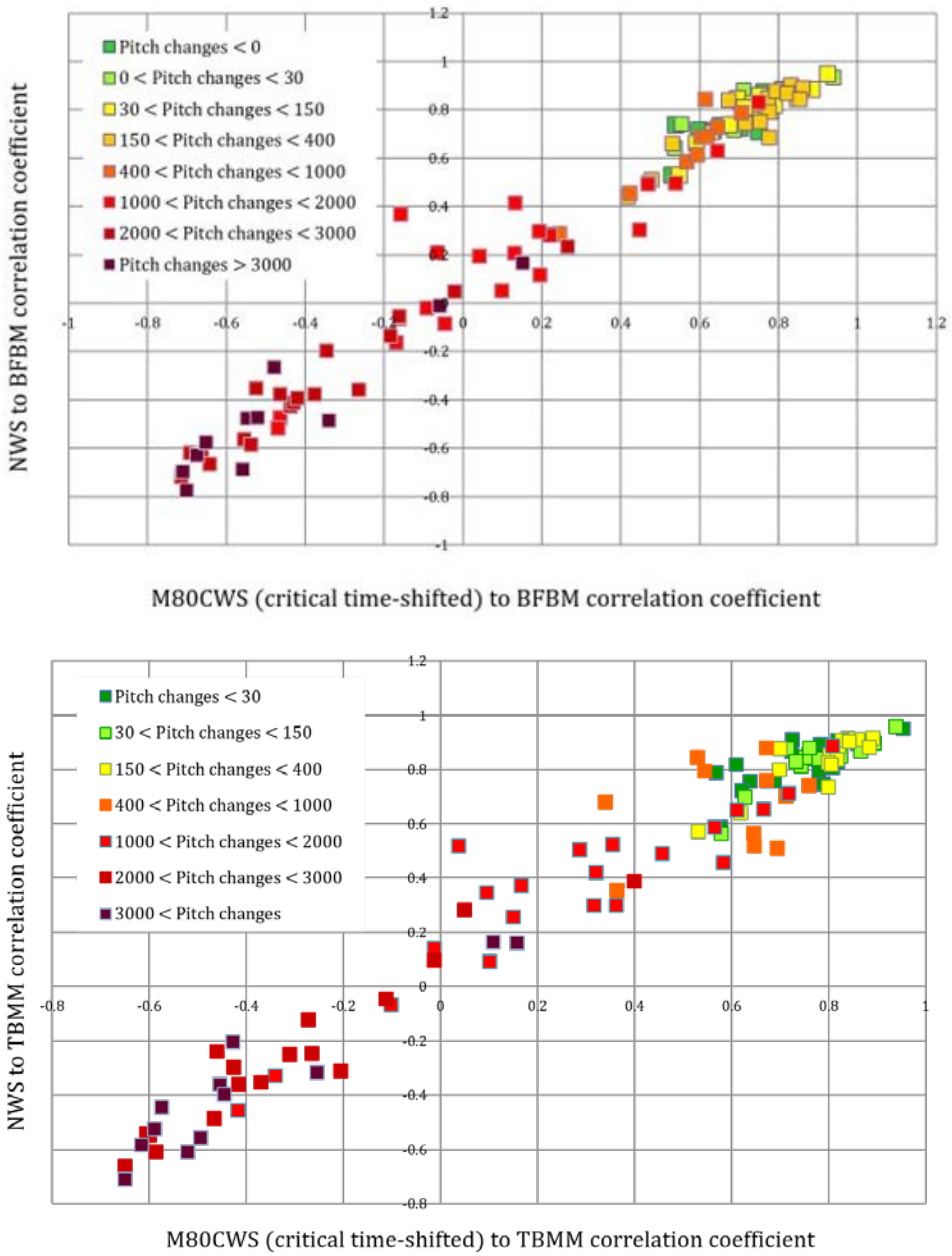

Figure 20. Correlation coefficients between the critical-time-shifted met tower wind speed (M80CWS) or nacelle wind speed (NWS) and the BFBM (top plot) or TBMM (bottom plot).

Each 10-min dataset is colored based on the number of pitch changes in each of the 10-min periods in Figure 18 (i.e., after the down-select process for misalignment and low advection speed).

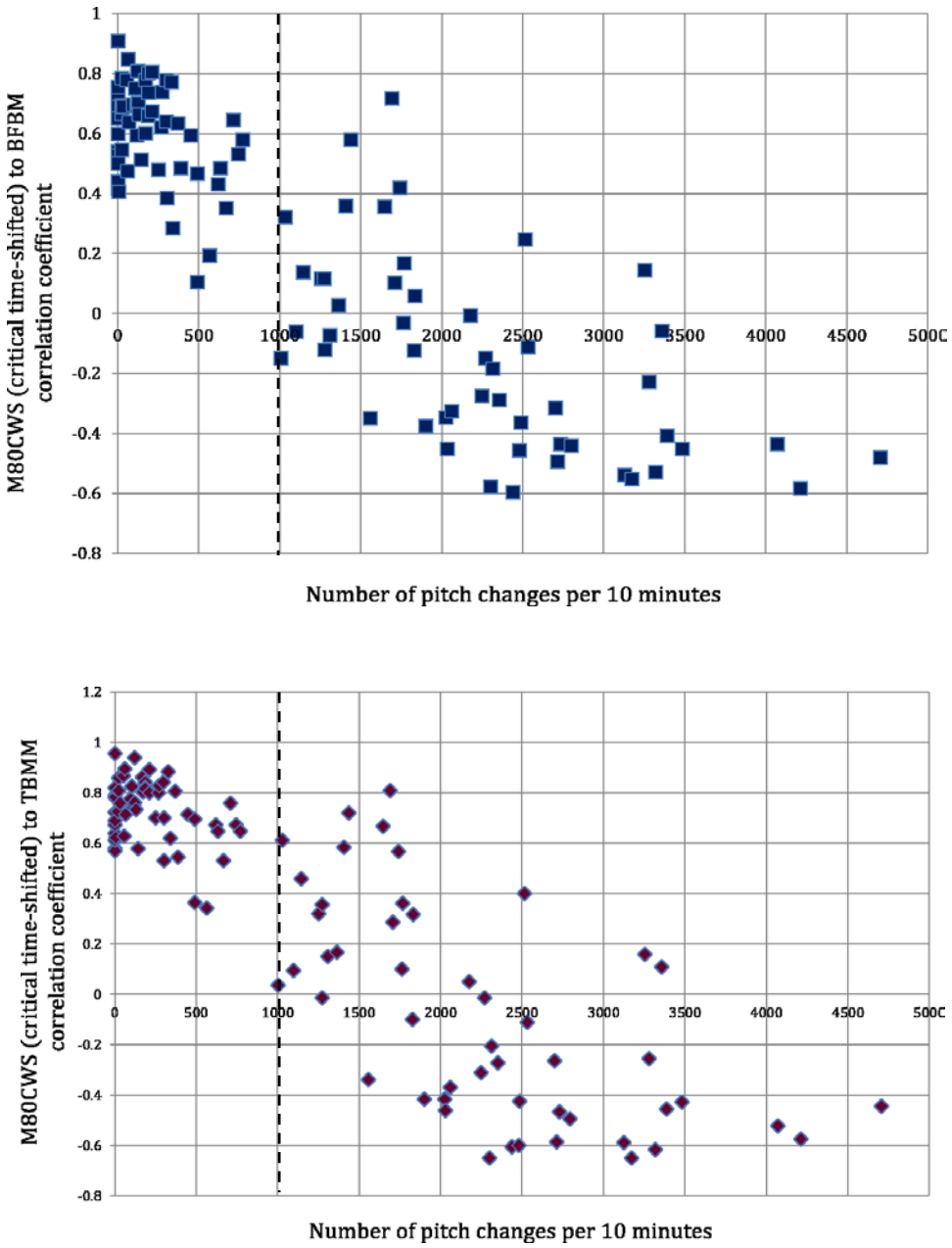

Figure 21. Correlation coefficients between the critical-time-shifted met tower wind speed and the BFBM (top) or TBMM (bottom).

Each of the 109 10-min datasets in Figure 18 is plotted here against the number of pitch control events in the 10-min period.

Figure 22 gives examples of two 10-min datasets for BFBMs and tower-based bending-moment magnitude that have survived the pitch segregation process. When the criterion is applied, 56 datasets remain from the original 132 in Figure 16; 109 datasets remain in Figure 18, where the initial datasets were segregated due to misalignments and low advection speed. Figure 23 shows the final 56 datasets that we applied in the analyses that follow.

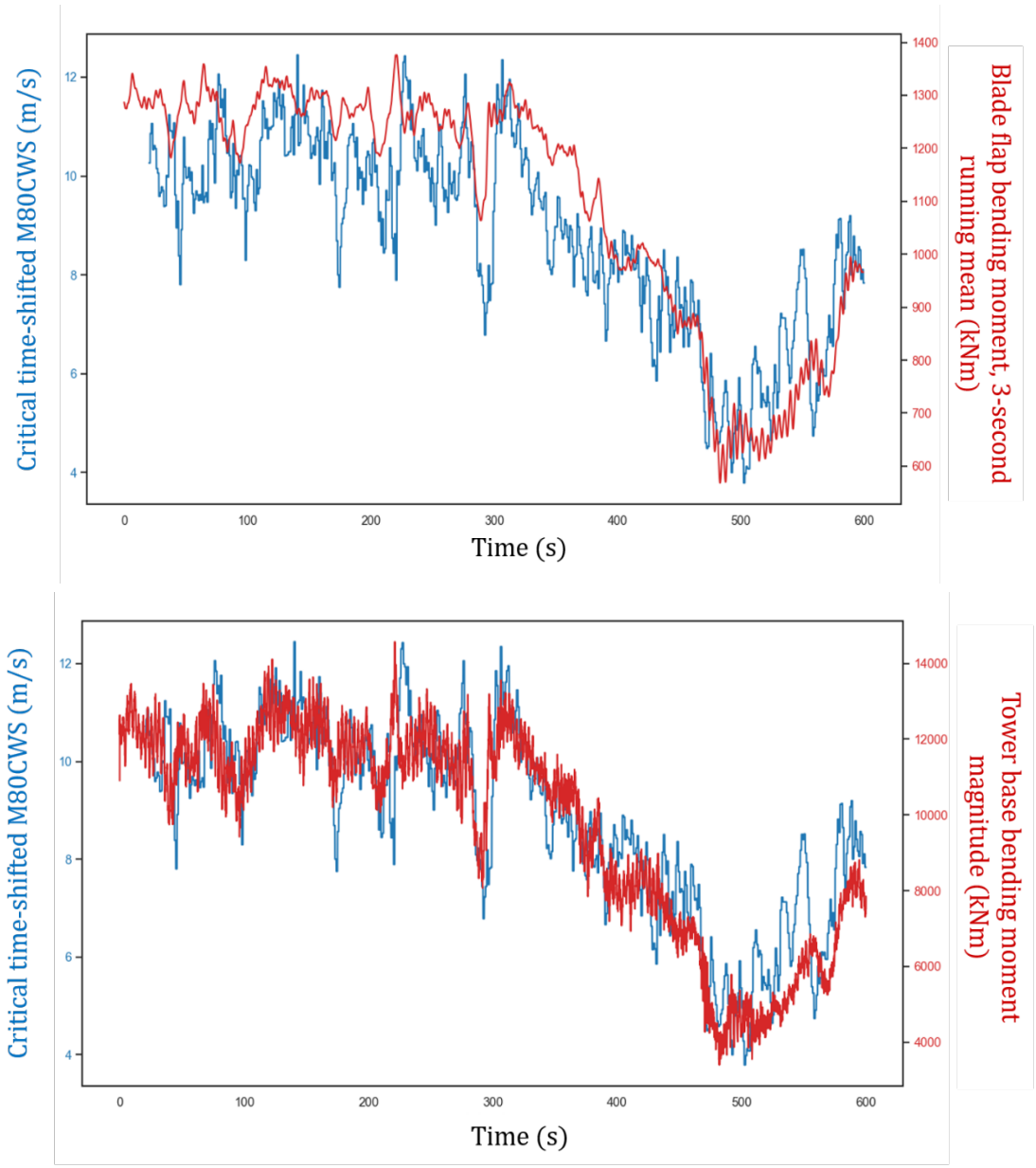

Figure 22. Examples of high-correlation comparisons of critical-time-shifted horizontal wind speed from the met tower hub anemometer (blue) and BFBM (top) and TBMM (bottom) during 10-min periods with westerly winds.

In these examples, the cc of the two datasets is 0.81 for BFBM (top) and 0.89 for TBMM (bottom). The critical time shift τ_{crit} is 20 s.

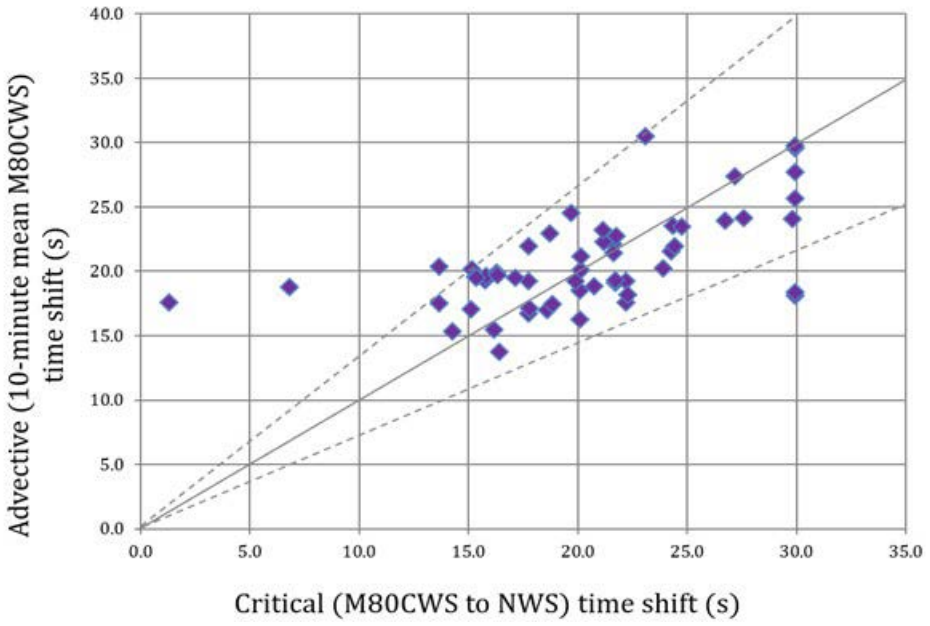

Figure 23. The 56 westerly datasets remaining from Figure 18 after removal of the datasets that exceeded the threshold of 1000 pitch control events per 10-min period.

From the 109 dataset periods in Figure 18 (reduced from the original 132), 56 datasets remain. The correlation coefficient for the points on this plot is 0.593, increasing to 0.748 when the four points outside the dashed lines are excluded.

7 Response of GE 1.5-MW Wind Turbine Loads to Westerly Turbulence Eddy Passage

7.1 Response of Main Shaft Moments to the Passage of Mountain-Generated Turbulence Eddies: Comparisons With the LES-ALM Predictions

As discussed in Section 1, whereas torque underlies power, the OOP bending moment at the hub underlies the aerodynamic forcing of the main bearing (Eq. (1)). As discussed in Section 2.3, high-fidelity LES of a 5-MW wind turbine operating in a typical daytime ABL at constant rotor speed predicts that daytime ABL turbulence creates time changes in OOP bending moment at the rotor hub with magnitudes $M_{H_\perp}(t) = \left|\mathbf{M}_{\mathbf{H}_\perp}(t)\right|$ that are *of the same order or larger* than the torque, $M_{H_x}(t)$. Importantly, the simulations predicted that, over the 200-s period of the simulations, the temporal fluctuations in torque were *fully uncorrelated* with the time changes in OOP bending moment magnitude, $M_{H_\perp}(t)$. This lack of correlation implies the existence of aerodynamic mechanisms that generate changes in power that are fundamentally different than those that generate force on the main bearing. From Figure 4 the simulations predict that temporal variations in torque are *strongly correlated* with temporal variations in horizontal wind speed averaged over the rotor plane. Like torque, time changes in horizontal wind speed are *fully uncorrelated* with those of nontorque bending moment, $M_{H_\perp}(t)$. By contrast, time variations in $M_{H_\perp}(t)$ are *strongly correlated* with the time changes in the nonuniform distribution, or "asymmetry," in the horizontal velocity distribution over the rotor disk.

The LES-ALM-predicted responses of hub moments to daytime ABL turbulence imply that the denominator in LCOE (power) is impacted by fundamentally different physics than is a potential contributor to the numerator, main bearing failures; correspondingly different mechanisms are required for mitigation strategies. It is therefore important to confirm the key LES-ALM based results in Figure 4 with field data from the response of a utility-scale wind turbine to atmospheric eddies. To this end, key validation comparisons of the responses of the GE 1.5-MW wind turbine to westerly winds with mountain-generated turbulence eddies are described in this section using wind data from the M5 met tower. This is followed in Section 9.2 with comparisons with measured responses of the GE 1.5-MW wind turbine to ABL eddies embedded within northerly/southerly winds using the nacelle anemometer.

However, whereas torque at the hub (M_{H_x}) in the computational experiments is equivalent to torque measured on the main shaft in the field experiments, this is not the case with the OOP bending moment vector, in principle. As described in Section 4.3 (Figure 10), the OOP bending moment components were measured in the field with two strain gauge bridges placed on the main shaft 0.8 m downwind of the main bearing. Eq. (2) is the equilibrium relationship between the nontorque bending moment vector measured on the main shaft, $\mathbf{M}_{\mathbf{S}_\perp}(t)$, and the hub OOP bending moment computed in the simulations, $\mathbf{M}_{\mathbf{H}_\perp}(t)$. This equation implies that $\mathbf{M}_{\mathbf{S}_\perp}(t) \propto \mathbf{M}_{\mathbf{H}_\perp}(t)$ if the contribution from net aerodynamic force does not contribute significantly to the correlations calculated. As discussed in Section 1.1, there are arguments and

a recent (unpublished) computational result that indicate that this is the case, so we argue that the correlations with $M_{H_\perp}(t)$ shown in Figure 4 should be well-approximated by correlations with time changes in the magnitude of measured OOP bending moment vector on the main shaft, $M_{S_\perp} = \left|\mathbf{M}_{\mathbf{S}_\perp}\right|$.

The average correlation coefficients with standard deviations are given in Figure 24 for the three key correlations shown in Figure 4 with $M_{S_\perp}(t)$ substituted for $M_{H_\perp}(t)$: the temporal variations in torque vs. nontorque bending moment, the temporal variations in "rotor-averaged" horizontal wind velocity vs. torque, and the temporal variations in horizontal wind vs. nontorque bending moment. These results confirm key computer simulation results: the time variations in torque $M_x(t)$ and magnitude of the OOP bending moment $M_{S_\perp}(t)$ are fully uncorrelated (cc = 0.050) in time, whereas the temporal variations in torque and rotor-averaged horizontal wind velocity are highly correlated (cc = 0.828). Also, like the computer simulations, horizontal wind velocity and nontorque bending moment are fully uncorrelated (cc = 0.072). Similar results are obtained using the nacelle cup anemometer, as will be discussed in Section 8.

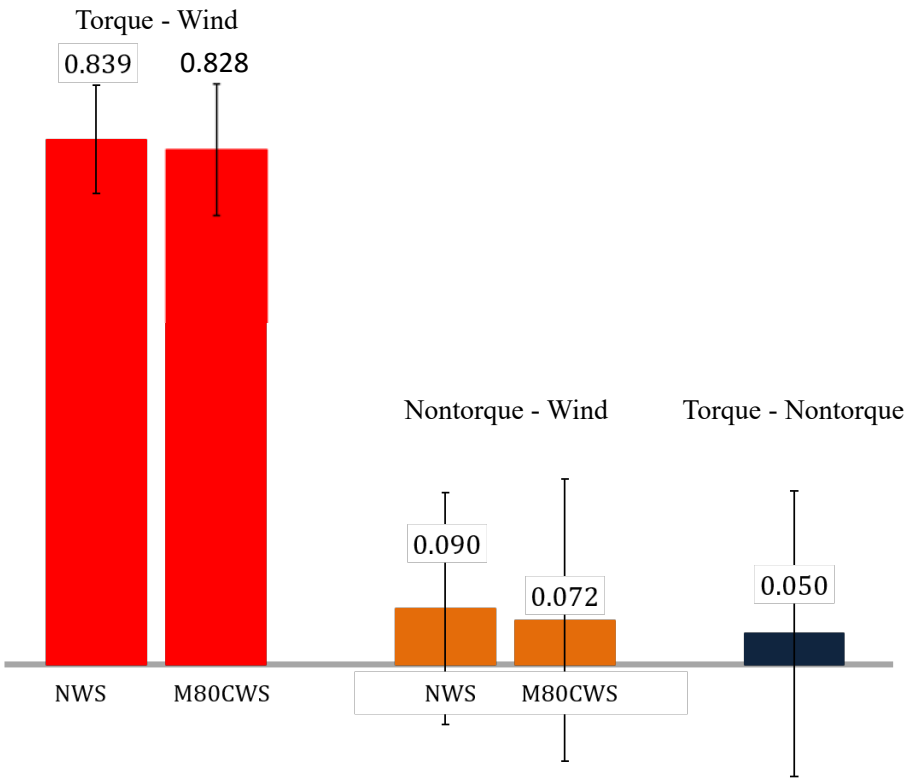

Figure 24. Five correlation coefficients (cc) are shown among the indicated pairs of variables measured with the GE 1.5-MW wind turbine in response to westerly winds and mountain-generated turbulence and averaged over the 56 datasets in Figure 23 (i.e., after segregation).

The nontorque bending moment is measured on the shaft (Section 4.3). In the correlations labeled M80CWS, "Wind" is the average over all anemometers on the met mast over the rotor plane (41.5 to 118.5 m, see Figure 10) shifted in time by τ_{crit}, as an approximation of rotor-averaged horizontal velocity used in Figure 4. The cc with the single hub anemometer alone is 0.769. In the correlations labeled NWS, "Wind" is the nacelle cup anemometer value. Bars indicate ±1 standard deviation.

In Figure 25 we show examples of 10-min signals of torque and horizontal wind velocity together, and we show examples for OOP bending moment magnitude and horizontal wind velocity together. The torque-wind pair have a high correlation coefficient (cc) of 0.84 and the nontorque-wind pair have a very low cc of −0.09. One also observes that the peak-to-peak variations around the trend lines (not shown) are much higher for the nontorque bending moment than for torque. Consequently, time-local values of OOP bending moment magnitude often exceed those for torque.

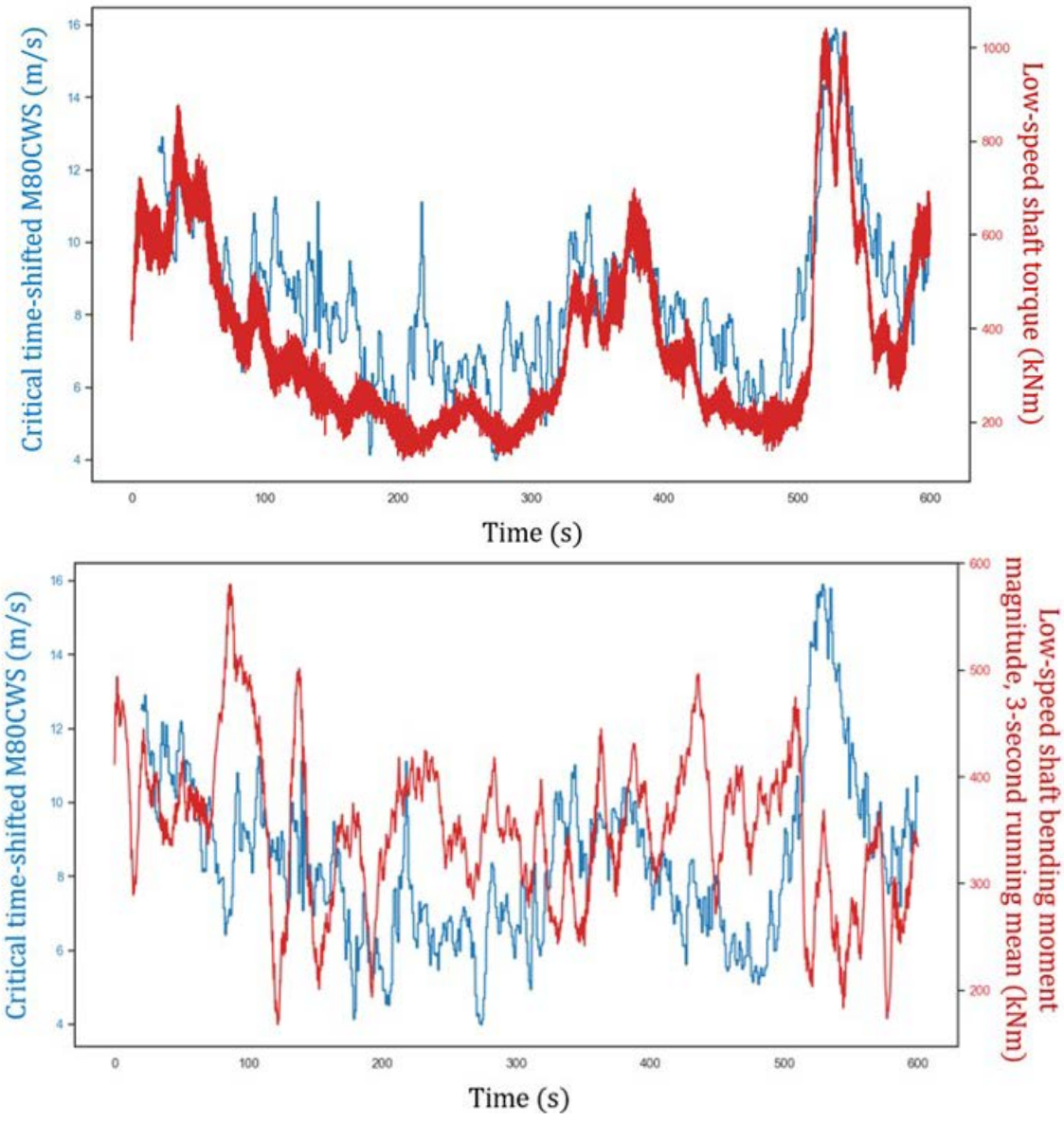

Figure 25. Examples of time variations between the met tower hub wind speed (blue critical-time-shifted M80CWS curves) and the highly correlated red signal in the top figure (main shaft torque, cc = 0.84) vs. the uncorrelated red signal in the bottom figure (nontorque bending moment magnitude, cc = -0.09).

The critical time shift, τ_{crit}, is 20 s. The 10-min mean of the torque and nontorque bending moment magnitude are 376 kNm and 351 kNm, respectively, a relative difference of 7%.

In context with the observation made in Section 2.3 that torque over the 200-s LES-ALM prediction period of Figure 4 for the NREL 5-MW wind turbine within the daytime ABL is of order the nontorque moment magnitude, in Figure 25 we note that the relative difference between the 10-min means in torque vs. nontorque bending moment magnitude is only 7%. It turns out that this is typical. Of the 56 westerly datasets, the 10-min averages of the OOP bending moment magnitudes exceed the 10-minue averages of torque in 26 out of the 56 datasets of Figure 23, and the average difference is only 2.9%, in favor of the OOP bending moment. The standard deviation of the difference, however, is 34%. This indicates wide variability between 10-min periods in which torque dominates, and 10-min periods where OOP bending moment dominates, sometimes by more than 30%. Thus, we find from the field data of interactions between mountain turbulence eddies and a 1.5-MW wind turbine that the average OOP bending moment induced by the turbulence eddies is of order the average torque and often more. Furthermore, the relative difference in average torque vs. OOP bending moment varies widely from near parity to a maximum of ±50% over 10-min periods.

7.2 Response of the Blades and Tower to the Passage of Turbulence Eddies

Figure 26 shows the correlation coefficients between time variations in horizontal wind velocity measured from the met tower hub anemometer (shifted by τ_{crit}) and the three load quantities indicated on the figure. The blade flap and edge moment was measured by the strain gauge at the blade base and the magnitude of the TBMM vector was measured with strain gauges 5 m from the tower root (Section 4.3, Figure 10 and Table 2). Shown are average correlation coefficients with standard deviation over the 56 westerly datasets indicated in Figure 23. Correlations are given using both the cup anemometer on the met tower (M80CWS) and the nacelle cup anemometer (NWS). These will be compared in Section 8.

We find good correlation between time-varying horizontal wind velocity and BFBM (average cc = 0.614) and no correlation with the blade edge bending moment (cc = 0.066). The temporal oscillations in tower bending moment are well correlated with temporal fluctuations in horizontal wind (cc = 0.736), as might be anticipated given the high correlation between torque/power and horizontal wind. Similarly, it is not surprising to find reasonable correlation between BFBM and horizontal velocity. Both of these strong correlations suggest that the time variations in the horizontal wind from the passage of energy-dominant turbulence eddies through the wind turbine rotor may play a role on blade and tower life. This is in addition to potential impacts on main bearing failure discussed in Section 7.1.

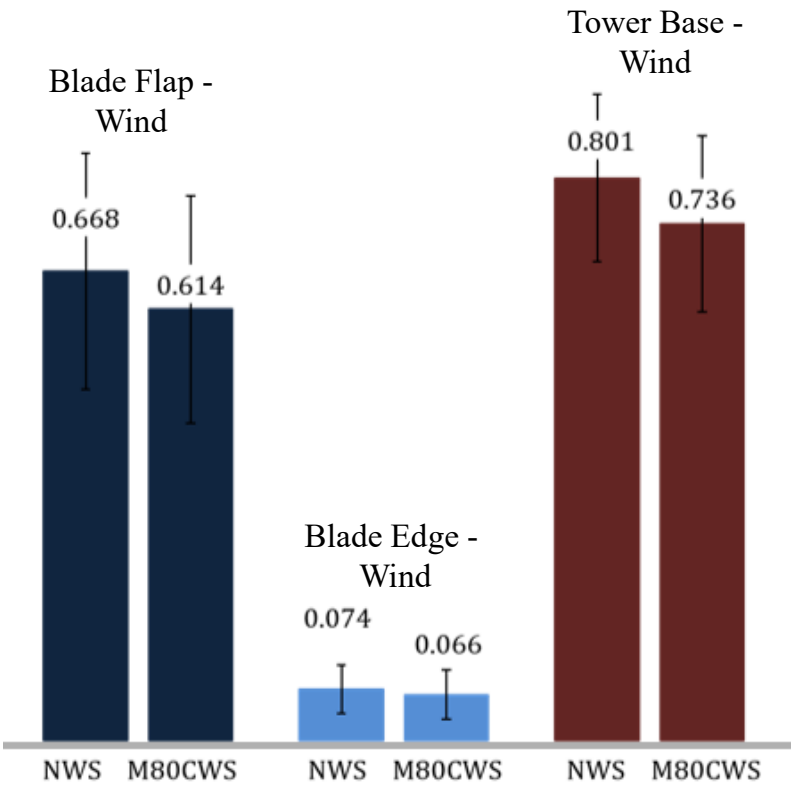

Figure 26. Correlation coefficients between the met tower hub wind speed (M80CWS) or nacelle anemometer wind speed (NWS) and the variable indicated in the westerly winds.

The wind speed measured at the met tower is time shifted by τ_{crit}. Bars indicate ±1 standard deviation.

8 Validity of the Nacelle Wind Anemometer for Turbine Load Response

Figure 27 is a typical comparison of the same frequency spectrum measured using data from the nacelle anemometer (NWS) and data using the hub anemometer on the met tower (M80CWS) for the same westerly 10-min dataset. These spectra are nearly identical, suggesting that the spectral content of the winds on the nacelle a few meters downstream of the rotor is unchanged from the winds 162.2 m upstream of the wind turbine rotor.

As explained in Section 1.2, we wish to use the nacelle anemometer as a surrogate for the met tower in our analysis of the response to atmospheric boundary layer turbulence using the northerly/southerly winds for the quantification of correlations. We therefore compare our previous analysis of the met tower with the same quantifications using the nacelle anemometer, both in westerly winds. If the comparisons are sufficiently close, we can use the nacelle anemometer with confidence to compare the response of the GE 1.5-MW wind turbine to the atmospheric boundary layer eddies embedded within the northerly/southerly winds with the mountain-generated turbulence eddies embedded within the westerly winds.

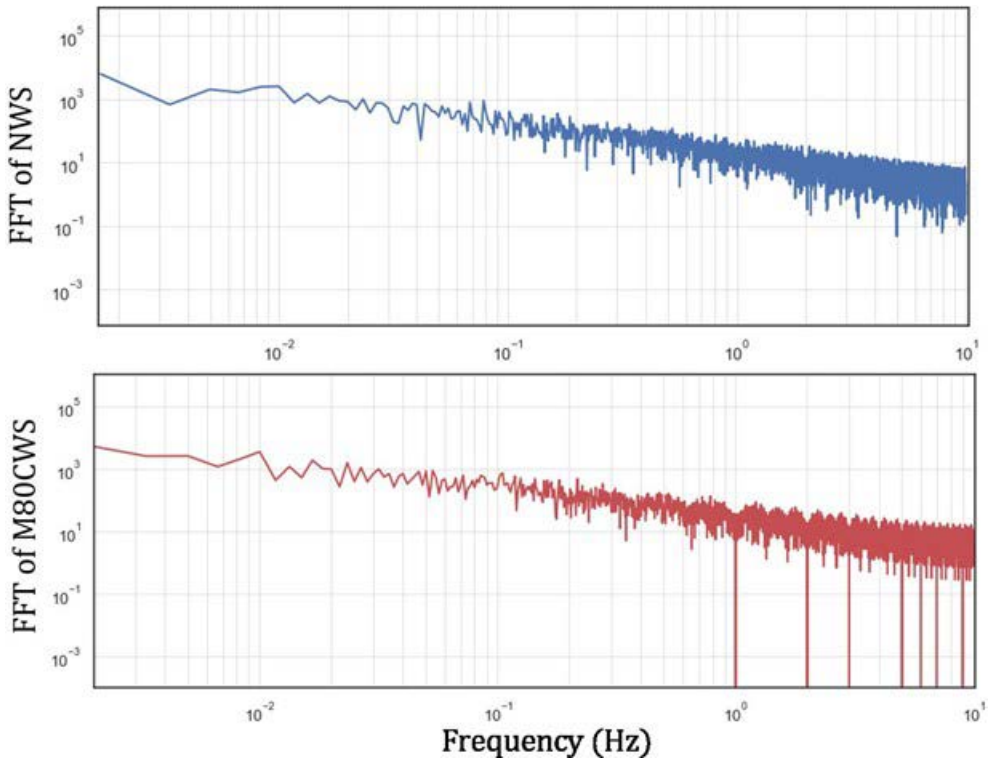

Figure 27. Time spectra of horizontal wind speed in the westerly winds measured by the nacelle cup anemometer (NWS, top), and on the met tower hub anemometer (M80CWS, bottom) from the same 10-min dataset

It was previously shown in Figure 24 that for westerly winds the key correlation coefficients (cc) discussed in the current study between moment components measured with strain gauges on the main shaft and horizontal velocities measured with time-shifted met tower anemometers produce

the same conclusions as cc's measured with the nacelle anemometer. Specifically, after averaging over the 56 final westerly datasets, the average cc between time-shifted horizontal winds measured with a single met tower anemometer (M80CWS) at hub height and torque was 0.769 (0.828 using winds "rotor-averaged" over multiple anemometers) compared to 0.839 when the nacelle anemometer (NWS) is used, all within the standard deviation bars and indicating high correlation. Similarly, the very low cc between horizontal wind and the OOP bending moment vector magnitude was 0.072 using the met tower hub anemometer and 0.090 using the nacelle anemometer, again within the standard deviation bars. We conclude from Figure 24 that the average cc's are statistically the same using either nacelle or met tower anemometers. The same conclusion results from Figure 26, where the average cc's between wind speed and flap and edge strain-gauge-measured moments on the blade and moments measured on the tower base are statistically equivalent when using the met tower hub anemometer or the nacelle anemometer.

Corresponding to the plots of average cc's in Figure 24, in Figure 28 we show scatter plots of the individual cc's for the westerly datasets with the cc value using nacelle anemometer wind speed plotted on the vertical axis against the cc value using the met tower anemometer wind speed (time-shifted) on the horizontal axis for each dataset. From Figure 28 the correlation coefficients between individual met tower and nacelle cc's are high: 0.724 for torque and 0.861 for the nontorque bending moment magnitude. Furthermore, from Figure 24 the averages of the cc's for the M80CWS vs. NWS anemometers are similar: the torque averages are 0.769 vs. 0.839, and the OOP bending moment averages are 0.072 vs. 0.090. In Figure 28, the higher level of scatter in the torque-wind scatter plot reflects the narrower range of high cc's. The cc's range from 0.55 to 0.97 over 56 datasets. In contrast, the nontorque-wind correlations are over a wider range and include some negative cc's: -0.38 to +0.50. Yet even including negative cc's, the 10-min cc values using data from the nacelle anemometer correlate well with data from the met tower.

This is even more the case for the individual cc's in the scatter-plot shown in Figure 20. In this figure the individual cc's using wind data from the nacelle anemometer are plotted individually against the same cc calculated with wind data from the met tower anemometer. The comparisons are excellent for the correlations with both BFBM and TBMM magnitude, even when the cc's are negative. As discussed in Section 6.2.2, the negative cc's are due to the existence of excessive pitch events over the 10-minute sample period, shown by the red and purple colors. These were removed in the final segregation process (Section 6.2.2). However, even including these pitch-impacted datasets with many negative cc's, the correlation coefficient between cc's with nacelle vs. met tower data was extremely high: 0.99 for both variables in the figure. These results suggest that, for the statistics calculated in this study based on 10-min sample periods, the nacelle cup anemometer produces measurements of nonsteady velocity variations that mimic closely the characteristics obtained using the met tower anemometers.

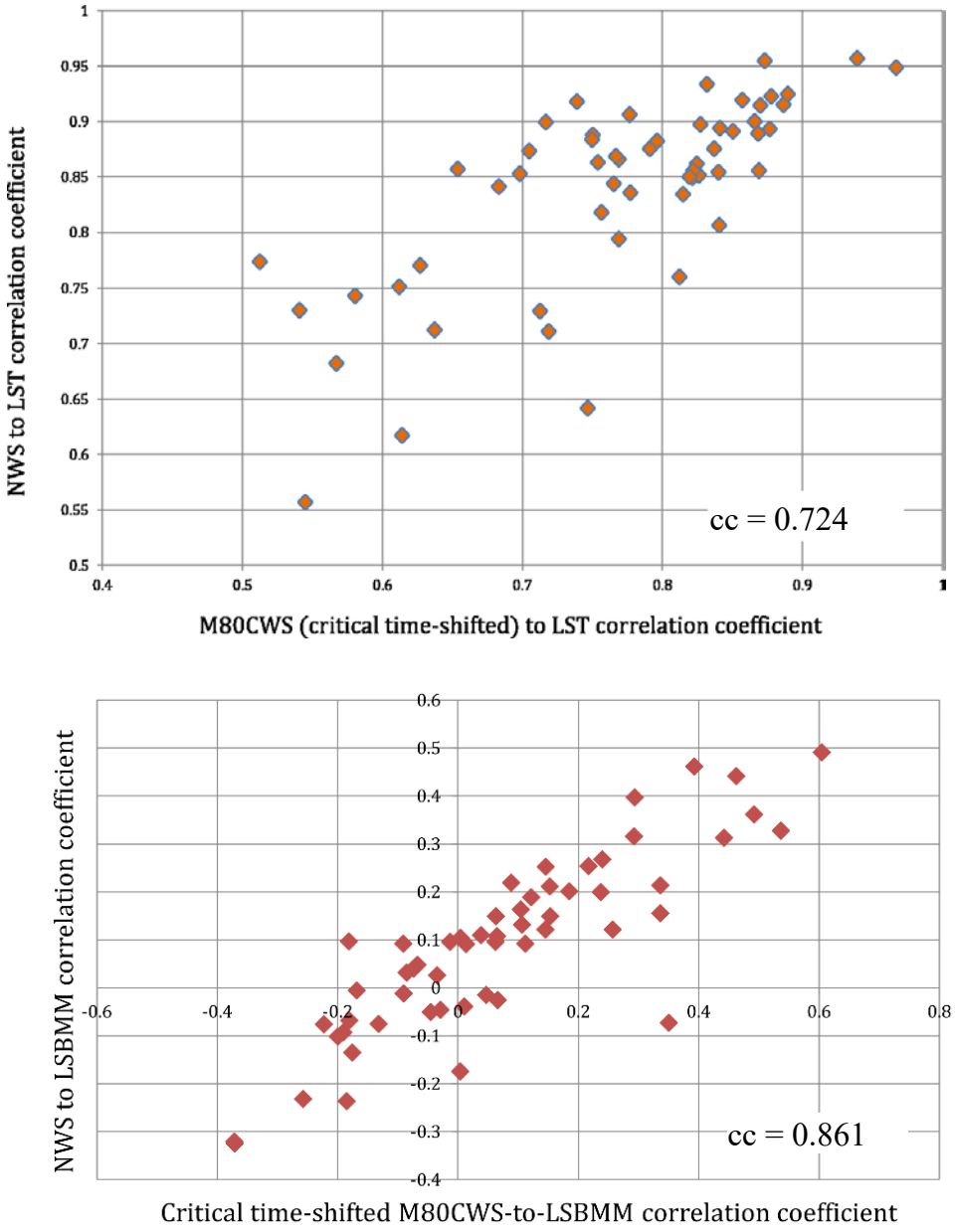

Figure 28. Scatterplots of the 10-min correlation coefficients (cc) between time variations in torque (LST, top) and OOP bending moment magnitude (LSBMM, bottom), and horizontal wind velocity measured with the nacelle cup anemometer (NWS) and the met tower hub anemometer (M80CWS)

Each point on the figure is calculated for one of the 56 westerly datasets after final segregation (Figure 23). The net cc over the 56 datasets is indicated on each plot.

The study by St. Martin et al. (2017) adds insight to our analysis. These authors quantified transfer functions between nacelle and met tower anemometers from the GE 1.5-MW wind turbine and M5 met tower at the Flatirons Campus for estimating annual energy production. In their publication, they state that "at wind speeds below 9 m/s, the nacelle anemometer measurement closely corresponds to the upwind wind speed measurement. Above this wind speed threshold, however, the nacelle anemometer underestimates the upwind wind speed and statistically significant distinctions emerge in the transfer functions for unstable and stable cases

as defined by the bulk Richardson number (R_B), particularly for wind speeds between 9 and 11 m/s." We had restricted our 10-minute datasets to exclude those with significant pitch which, from Figure 12, occurs at 9.6 m/s. Thus, we have excluded datasets at the higher wind speeds that Martin et al. (2017) found were associated with significant differences between the nacelle vs. met tower anemometers. In our analysis we restricted our analysis to datasets primarily at the lower speeds that the St. Martin et al. study associated with accurate estimates. Taken together, the two studies suggest that (1) the high correspondence obtained in the current study with data from the two anemometers is a consequent of our restriction to the lower wind speeds to minimize pitch events, and (2) that the poor correspondence in the Martin et al. study between met tower and nacelle anemometer data at their higher wind speeds may be a consequence of pitch control.

9 Response of GE 1.5-MW Wind Turbine Loads to Northerly/Southerly ABL Turbulence Eddy Passage

From the previous analysis, we conclude that the nacelle anemometer can be used as a surrogate for the met tower hub anemometer to analyze the winds from the north and south. These winds do not contain mountain-generated turbulence eddies and represent daytime ABL turbulence. We therefore analyze in this section the response of the GE 1.5-MW wind turbine to the passage of atmospheric surface layer turbulence eddies through the rotor plane, in contrast to the passage of mountain-generated eddies analyzed in Section 7.

Whereas in the westerly winds 56 datasets were analyzed after full segregation, 33 datasets were used in the analysis of northerly and southerly winds, with all but 7 from the south. Because a met tower was not used, only segregation based on pitch events was possible. Because pitch activity was low in all 33 datasets (the highest number of pitch events was only 270, well below the cutoff of 1000 previously determined in Section 6.2.2), no segregation was needed and all 33 10-min datasets were used to calculate statistics on turbine response.

9.1 Differences Between Westerly and Northerly/Southerly Wind Turbulence Characteristics and Response Loads and Scales

In Section 3.2 we described key differences between mountain-generated eddies within the westerly winds and ABL turbulence eddies from LES. In this section we compare turbulence characteristics within the westerly wind with those within the northerly/southerly winds.

In Table 6 we compare the differences in wind-related variables between westerly winds carrying mountain-generated turbulence eddies, and northerly/southerly winds containing ABL eddies, in both cases calculated using the same met tower hub anemometer. We note that all wind-related characteristics are somewhat stronger for westerly winds with mountain-generated eddies as compared to northerly/southerly winds with the elongated surface layer eddies of the ABL shown with LES in Figure 3. Specifically, the average wind speed of the westerly datasets is 14% higher than the northerly/southerly winds and the standard deviation is 26% higher. Consequently, turbulence intensity is twice as high in the westerly winds (20%), on average, as compared to the northerly/southerly winds (10%). Wind shear and veer are comparable between the two datasets. Wind shear and veer were quantified as the average difference between the 10-min-mean horizontal wind velocity magnitude (shear) and angle (veer) between the upper and lower margins of the rotor disk in the vertical, using the met mast for all wind directions. The mean velocity difference associated with shear is only about 1 m/s, whereas the mean angle difference is only about 3°. These characteristics suggest minimal impacts of average wind shear and veer on wind turbine response. Interestingly, the average integral time scale is nearly the same in the two flows, 35 s vs. 37 s, suggesting comparable advective passage times of the energy-containing turbulence eddies through the rotor disk. Similar average time scales are calculated using the nacelle anemometer (Table 7).

Table 6. Comparisons of Averages Over 10-min Datasets of Wind-Related Quantities Between Westerly and Northerly/Southerly Datasets Measured Using the Met Tower Hub Anemometer

Variable	Westerly Datasets	Northerly/Southerly Datasets
Number of available datasets	56	33
10-min mean horizontal wind speed	8.07 m/s	6.96 m/s
10-min mean standard deviation of horizontal wind speed	1.57 m/s	0.658 m/s
10-min mean turbulence intensity	0.197	0.0982
Shear: Average difference of 10-min-mean wind speed between top and bottom of the rotor disk (30 m to 130 m)	1.16 m/s	0.990 m/s
Veer: Average difference of 10-min-mean wind vector angle between top and bottom of the rotor disk (38 m to 122 m)	3.40°	2.84°
Mean integral time scale of horizontal wind speed (s) at M5 met tower	36.9 s	34.9 s

Table 7 is an interesting compilation of response time scales for different components of the wind turbine to the passage of ABL turbulence eddies in northerly/southerly winds compared with mountain eddies within the westerly winds. Whereas the time scales that characterize responses to the passage of ABL eddies within the northerly/southerly winds are comparable to those for the passage of westerly mountain eddies, the time scales themselves separate into three classes of time response. These three classes are consistent with the three ranges of time scale described by Vijayakumar et al. (2016) and Nandi et al. (2017) and discussed in Section 1.1. The first class characterizes the responses at time scales between 36 s and 49 s, associated with the passage time of the energy-dominant turbulence eddies through the rotor plane. The variables associated with large-eddy passage time scale are power, torque, BFBM, and TBMM—all responses that correlate well with horizontal velocity (Figure 4, Figure 24, and Figure 26). The OOP bending moment magnitude responds with time scales ~4 to 10 s, likely related to the 1P rotation time of the wind turbine (greater than the rated time of 3.3 s due to slower rotor speeds during data collection). The blade edge bending moment, by contrast, responds with a subsecond time scale, which is consistent with the response to the passage of individual blades through the internal gradients within individual coherent eddy structure (Section 2.3). Full blade-boundary-layer-resolved LES has shown that this response creates large subsecond peak fluctuations in moments (Vijayakumar and Brasseur 2019) that may be relevant to main bearing response and failure.

Table 7. Comparisons of Averages of Integral Time Scales From 10-min Datasets of Horizontal Wind Speed and Key Turbine Loads Between Westerly and Northerly/Southerly Datasets

Integral Time Scales (s)	Westerly Datasets	Northerly/Southerly Datasets
Met Tower Hub Horizontal Wind Velocity	36.9 s	34.9 s
Nacelle Horizontal Wind Velocity	37.9 s	39.0 s
Power	48.8 s	54.9 s
Main Shaft Torque	46.9 s	49.8 s
Main Shaft Nontorque Bending Moment	9.74 s	4.32 s
Blade Flap Bending Moment (BFBM)	35.8 s	21.1 s
Blade Edge Bending Moment (BEBM)	0.585 s	0.685 s
Tower Base Bending Moment (TBMM)	47.8 s	50.6 s

In Figure 29 we compare the 10-min-mean values of wind turbine loads averaged over the available datasets for westerly and northerly/southerly datasets. Average torque and BFBMs are significantly lower for northerly/southerly winds, which is consistent with the lower turbulence levels in the northerly/southerly winds. However, the average magnitudes of the nontorque bending moment are close, suggesting that the average levels of asymmetry in the velocity distribution over the rotor disk are comparable in the northerly/southerly vs. westerly winds. Table 7, on the other hand, indicates that the time scale for the nonsteady nontorque bending moments in the northerly/southerly winds is about half that for the westerly winds. This suggests a corresponding smaller time scale for the changes in wind asymmetry over the rotor plane, perhaps a reflection of the fundamental differences in westerly vs. northerly/southerly eddy structure.

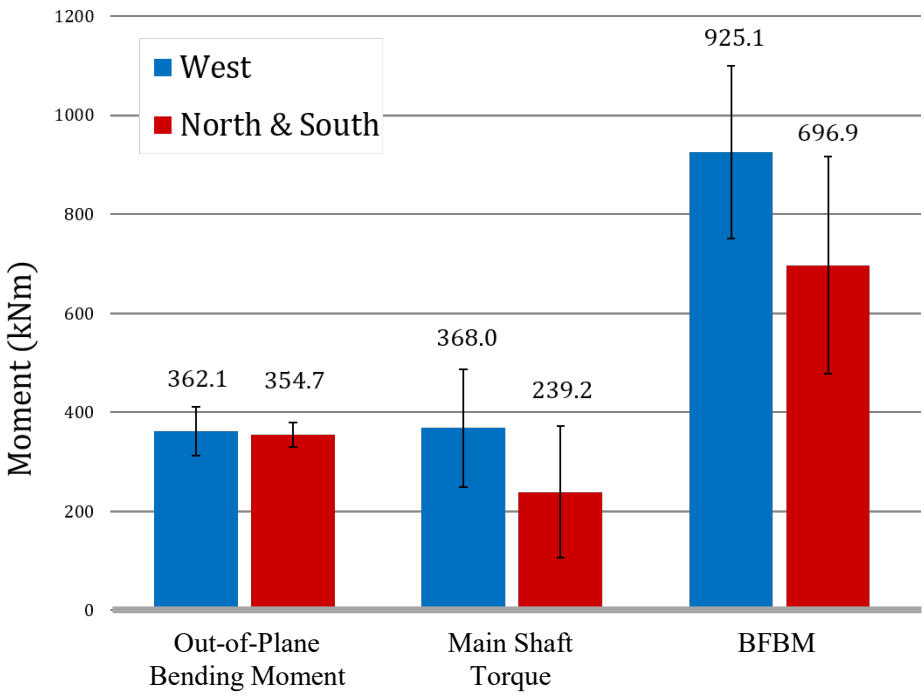

Figure 29. Comparison of mean magnitudes of OOP bending moment and torque between westerly and northerly/southerly datasets.

The bars indicate ±1 standard deviation.

9.2 Correlations in Northerly/Southerly Atmospheric Boundary Layer Turbulence

Comparing the average and standard deviation of the 10-min correlation coefficients for westerly winds in Figure 24 with those for northerly/southerly winds in Figure 30 we see that the results are very similar. Consistent with the LES-ALM computational model predictions of Figure 4 for a 5-MW wind turbine in daytime ABL turbulence, in Figure 30 we observe strong correlation between the time variations in torque and horizontal wind velocity (0.742 northerly/southerly vs. 0.769 westerly) and a complete lack of temporal correlation between torque and nontorque (OOP) bending moment magnitudes. There is also a complete lack of temporal correlation between the OOP bending moment and horizontal wind velocity fluctuations. Like Figure 25 for westerly winds, in Figure 31 we show 10-min examples of the temporal relationships between horizontal velocity measured with the nacelle cup anemometer compared to temporal variations in torque and OOP bending moment magnitude. Like westerly winds, torque correlates well with horizontal winds while nontorque bending moment does not. Furthermore, the deviations from the trends are much larger for nontorque bending moments than for torque, particularly in the response to 3P variations.

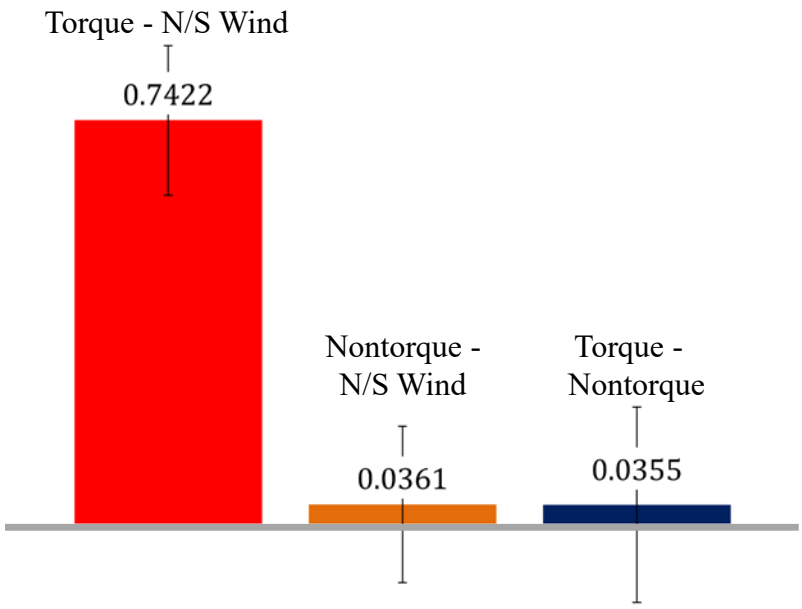

Figure 30. Averages of the 10-min cc's over the northerly/southerly datasets between the nacelle anemometer wind speed (N/S Wind) and torque, nontorque (OOP) bending moment magnitude, and between torque and nontorque bending moment magnitude.

Bars indicate ±1 standard deviation.

Note in Figure 31 that for this single 10-min dataset the average magnitude of the OOP bending moment *exceeds* that for torque by more than a factor of two. This observation is in context with that discussed in Section 2.3 regarding Figure 4, where torque exceeded nontorque bending moment by about 30% over the 200-s simulation period. The observation is also in context with the analysis of the westerly data discussed in Section 7.1 where we found that over the 56 westerly datasets with mountain turbulence eddies the relative difference between the nontorque bending moment and torque was only about 3%, on average, but with a very high standard deviation of about 40%. It turns out that over the 33 northerly/southerly datasets with ABL turbulence, the average relative difference between the OOP bending moment is even more strongly in favor of the OOP bending moment: 46% northerly/southerly vs. 3% westerly, with a comparably large standard deviation of 49%. It appears that the impact of atmospheric turbulence in the northerly/southerly winds on the generation of the OOP bending moments is even more substantial than in mountain-generated turbulence in our field analysis, and much more substantial than in the LES-ALM predictions. Based on these results, both mountain and atmospheric turbulence force the main bearing with very high variability and with mean moment magnitudes comparable to and larger than the axial moment component that drives power variations.

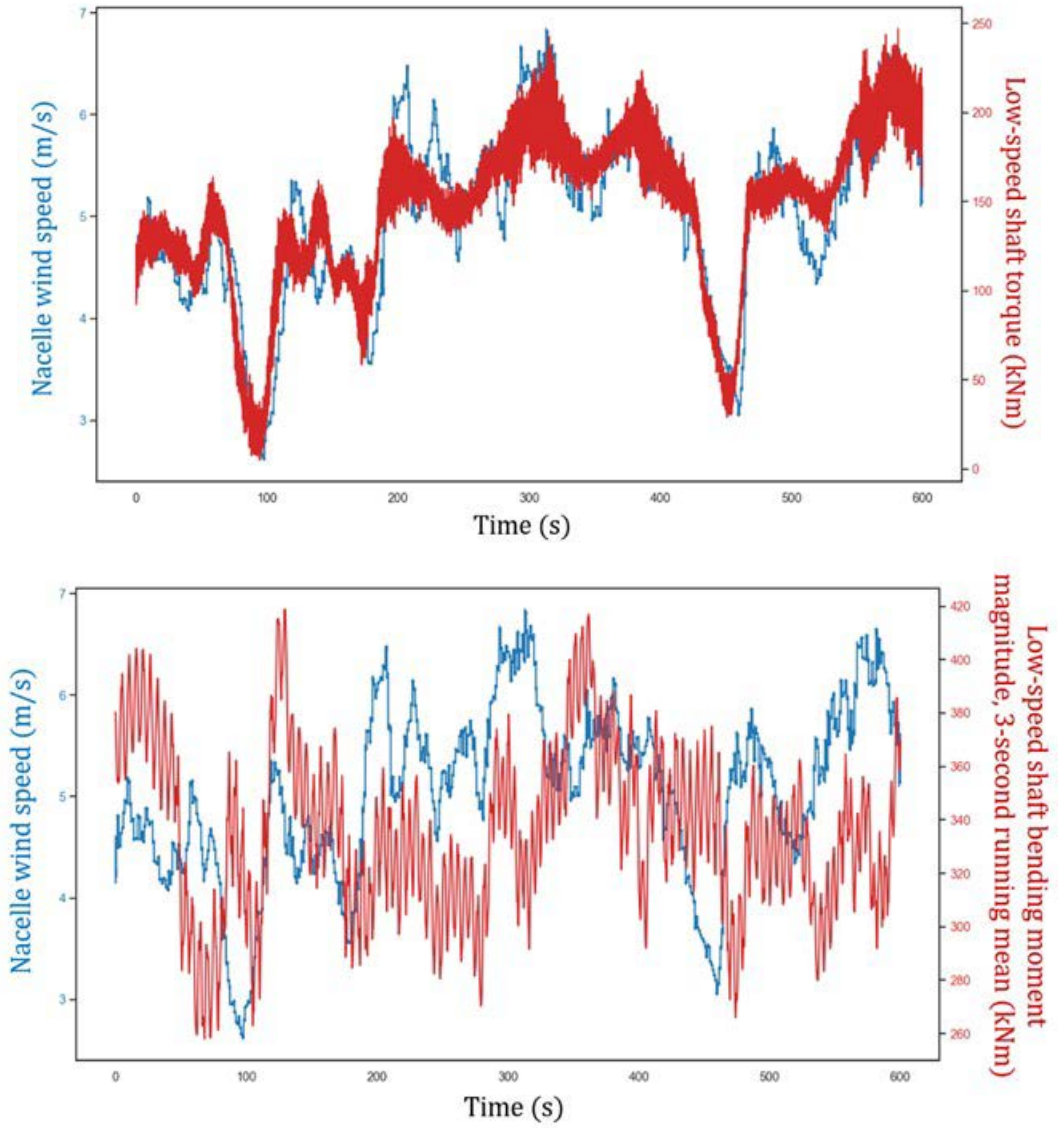

Figure 31. Examples of 10-min variations in nacelle-measured wind speed variations (NWS) and torque (top) and OOP bending moment magnitude (bottom) in northerly/southerly winds.

The cc for torque is 0.88 and for OOP bending moment is 0.41.

In Figure 32 we show the average correlation coefficients and standard deviations over the northerly/southerly datasets between horizontal wind speed (measured on the nacelle) and blade flap, blade edge, and tower base moments. Again, the results are like those for westerly winds shown in Figure 26. The correlation between winds and BFBM is moderate—0.52 for northerly/southerly winds and 0.61 for westerly winds—whereas the temporal variations in horizontal winds are uncorrelated to blade edge bending moment in both cases (0.03 vs. 0.07 for northerly/southerly vs. westerly winds). Correlation between horizontal wind variations and the TBMM is high for both northerly/southerly (0.75) and westerly (0.74) winds.

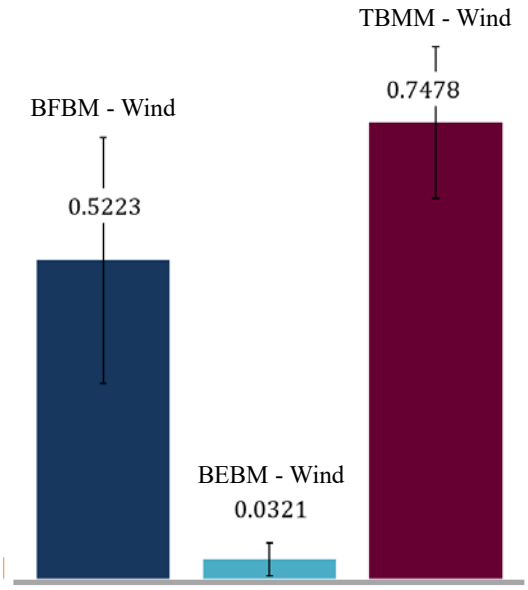

Figure 32. Averages of the correlation coefficients between nacelle wind speed (NWS) and BFBM, BEBM, and TBMM over the 33 northerly/southerly datasets.

The bars indicate ±1 standard deviation.

We conclude that the correlations in the response of the GE 1.5-MW wind turbine to ABL turbulence eddies are essentially the same as for mountain-generated eddies, even as the average torque and BFBM magnitudes in the northerly/southerly ABL winds are somewhat lower than in the westerly mountain winds (Figure 29). Given that the northerly/southerly ABL turbulence eddies are less intense than the westerly mountain eddies (Table 6), it may be that the differences in average response and correlations are due to differences in eddy intensity. To test this hypothesis, we excluded "high wind" datasets from the westerly data, where "high wind" is defined as those events with 10-min average horizontal velocity exceeding the maximum average wind speed for the northerly/southerly datasets, which is 6.96 m/s (Table 6). This exclusion left 25 datasets from the original 56 in which the response should be closer to the northerly/southerly ABL response to validate the hypothesis. In Figures 33 and 34 we compare the changes in the averaged moment response statistics and cc's in "low wind speed" datasets with all westerly datasets and with the northerly/southerly datasets. Figure 34 shows that there are only minor changes in the correlation coefficients with the removal of "high wind" datasets, all within the standard deviation bars. However, Figure 33 displays a tendency for the removal of "high-wind" westerly datasets to reduce the differences between average torque and BFBM, while not changing the previous equalization of the nontorque bending moment. We anticipate that the differences in the internal velocity structure of the three-dimensional turbulence eddies, as well as in the characteristic scale of mountain-generated versus ABL eddies, are likely also significant contributors to the differences observed in correlations between westerly winds with mountain eddies vs. northerly/southerly winds with ABL eddies.

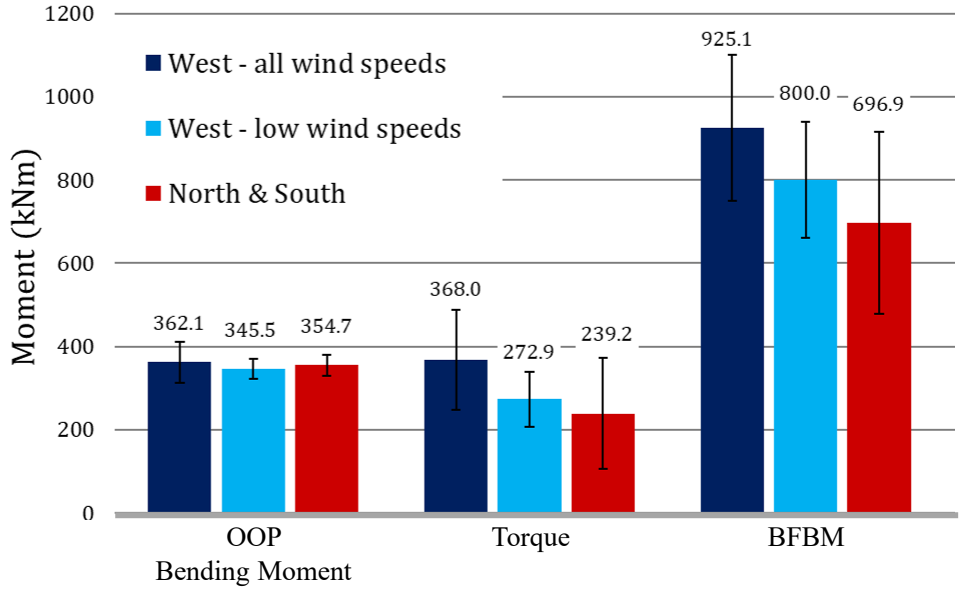

Figure 33. Comparison of 10-min-averaged OOP bending moment, torque, and BFBM.

Averages are over: (red) the 33 northerly/southerly datasets; (dark blue) the 56 westerly post-segregation datasets; (cyan) the 25 "low wind speed" westerly datasets after "high wind" datasets (> 6.96 m/s) were excluded (see text). The bars indicate ±1 standard deviation.

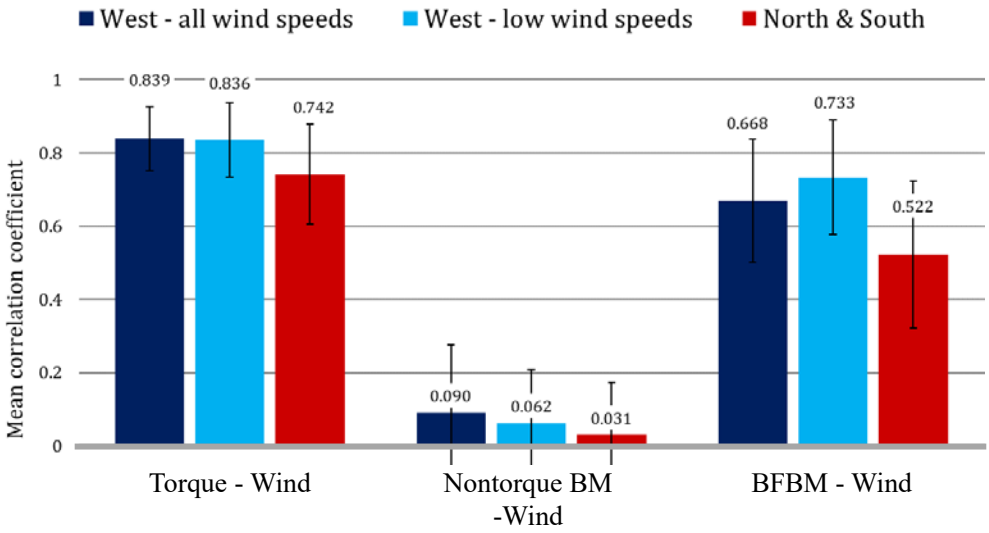

Figure 34. Comparison of averages of 10-min dataset correlation coefficients between horizontal winds and wind turbine variables in westerly and northerly/southerly datasets.

Averages are over: (red) the 33 northerly/southerly datasets; (dark blue) the 56 post-segregation westerly datasets; (cyan) the 25 "low wind speed" westerly datasets after "high wind" datasets (> 6.96 m/s) were excluded (see text). The bars indicate ±1 standard deviation.

10 Conclusions and Generalization of Wind Turbine Responses to Atmospheric and Mountain-Generated Turbulence Eddies

In this section, we integrate our analyses of data from two very different classes of experiment. The first is a high-fidelity computational experiment in which the space-time structure of the energy-containing turbulence eddies within the canonical daytime ABL are well resolved with high-resolution large-eddy simulation. This computer experiment captures the detailed interactions between the ABL turbulence eddies and the rotor blades of the NREL 5-MW wind turbine represented with an advanced actuator line model. The second class of experiment is of a smaller utility-scale 1.5-MW wind turbine in the field about 4.5 km to the east of the Rocky Mountain Front Range. This wind turbine responded to two classes of turbulence eddies, ABL turbulence eddies within the northerly/southerly winds, and mountain-generated turbulence eddies within the westerly flow over the eastern ridge of the Front Range. Whereas the nonsteady OOP moment components were calculated at the rotor hub in the computational experiments, in the field experiment the OOP moment was measured on the main shaft with strain gauges. The combination of the analyses for these two classes of experiment has allowed for the validation and generalization of important discoveries relevant to the nonsteady forcing of the wind turbine rotor and main shaft with impacts on the main bearing. These discoveries, discussed in detail in the previous sections, are summarized here.

10.1 Validation of a Key Computational Discovery and the Generalization of Aerodynamic Interactions Between Wind Turbines and Atmospheric Turbulence Eddies

From our analyses of field data obtained from the GE 1.5-MW wind turbine at the NREL Flatirons Campus, we conclude that the key predictions made with high-fidelity computer simulations of the response of a 5-MW wind turbine to turbulence eddies within the daytime atmospheric boundary layer are also true for the GE 1.5-MW wind turbine responses measured in the field, both to westerly and northerly/southerly winds. As discussed in Section 3.2 and quantified in Section 9.1, the mountain-generated turbulence eddies are of similar size and have similar eddy passage time to the ABL turbulence eddies, but are somewhat more energetic. The correspondences between the LES-ALM computer model and field measurements with both westerly and northerly/southerly winds suggest that the key mechanisms that underlie the aerodynamic responses of the wind turbine rotor to the passage of energetic turbulence eddies are generalizable to most energy-dominant turbulence eddies with lateral scales of order the rotor diameter.

As the turbulence eddies pass through the rotor plane, the aerodynamic responses of the blades and rotor at the hub are highly nonsteady with multiple time scales that reflect, in part, the passage of the rotating blades through the internal velocity-field gradients that exist within the coherence regions of the turbulence eddy structures (Vijayakumar and Brasseur 2019). Longer time scales characterize the advection of the coherent eddy structure itself through the rotor

plane. There are wide varieties of eddy structure. In ABL daytime turbulence, these are associated with convectively driven updraft and downdraft regions, and with shear-driven high and low speed streaks. These groupings of eddy structure vary with the global stability state of the daytime ABL (Jayaraman and Brasseur 2021). However, strong turbulence eddies can also be generated by nonplanar surface topography and the generation of separated flow eddies, for example from flow over mountains and hills. From the current study, we may generalize to conclude that a key consequence of the passage of energetic turbulence eddies through the wind turbine rotor is the generation of a strongly time-varying OOP bending moment vector acting on the main shaft that creates highly nonsteady changes in an aerodynamically generated force vector that acts on the main bearing at its interface with the main shaft.

10.2 The Key Impact of Atmospheric and Mountain Turbulence: The Generation of Strong Nontorque Moments on the Main Shaft

It is interesting and significant that in all three studies—the computational study of 5-MW wind turbine response to daytime ABL turbulence eddies and field analyses of the response of a 1.5-MW wind turbine to both mountain turbulence eddies and ABL turbulence eddies—the magnitude of the OOP bending moment vector is of order the torque magnitude when averaged over the 10-min dataset periods. In addition, these studies all agree that the fluctuation levels of the nontorque bending moment relative to the trends (low-pass-filtered signals) are much higher than those for torque. Consequently, the nontorque bending moment vector magnitude often greatly exceeds that for torque, both localized in time as well as for periods of time of order 10 minutes or greater. This is especially true of the energy-dominant turbulence eddies embedded within the northerly/southerly winds, which are structurally much closer to the LES-simulated ABL turbulence than are the turbulence eddies generated by highly turbulent flow over the peaks of the Rocky Mountain Front Range and embedded within the westerly winds. Furthermore, the variability in both the time-local and extended time periods in which the OOP bending moment dominates torque suggests that the OOP moment creates strong time variations in the force vector acting on the main bearing (Eq. (1)) with the characteristic time scales of the OOP bending moment vector.

Ultimately, the time changes in magnitude and direction of the moment vector acting on the main shaft result from the rotation of the blades through highly nonsteady strongly asymmetrical distributions of velocity as coherent eddies pass through the rotor plane (Section 2). A key computational result (Figure 4) indicates that the time changes in nonuniformity in the velocity distribution over the rotor plane generate time changes in hub OOP moment vector that generates time changes in the magnitude, location, and extent of the load zone over the main bearing (Figure 1). We conclude from this study that both atmospheric and mountain-generated turbulence eddies are sufficiently strong to force the hub moment vector sufficiently far off the main shaft axis to generate an OOP bending moment with magnitude as large or larger than the torque component. Thus, a necessary consequence of power production from wind turbines, in both highly turbulent ABL and mountain environments, is the generation of highly nonsteady forcing of the main bearing with potentially negative impacts that encourage bearing failure.

10.3 Mountain-Generated vs. Atmospheric Turbulence

A key observation from the current study is that the energy-dominant turbulence eddies that underlie both daytime atmospheric and mountain-generated turbulence create similar nonsteady aerodynamic responses in the blade-integrated loads that act on the main shaft. In particular, the moment component that underlies power (torque) is fully uncorrelated with the OOP moment vector that creates nonsteady forcing of the main bearing. The correspondence between the computational and experimental results confirm that both mean and fluctuating torque/power are generated primarily in response to mean and fluctuating rotor-averaged horizontal velocity. Figure 4 indicates that the same is true of the axial force acting on the main shaft at the hub (thrust). Figure 26 and Figure 32 indicate strong correlations between the temporal variations in horizontal wind velocity and TBMM and reasonably strong correlations between wind speed and BFBM. Sensitivity to horizontal velocity is consistent with what has been found computationally to be the dominant velocity component in the generation of lift on the airfoil sections of the turbine blades (Lavely 2017).

These observations are well illustrated in Figure 35, where the time changes torque and bending moment magnitude are overlaid with a color isocontour plot of the time changes in the vertical variations in horizontal velocity of the westerly winds. The isocontour plot was obtained from the available anemometers on the met tower in the vertical region within and around the rotor disk. Note that the vertical concentrations of horizontal velocity are of order the rotor disk diameter in the vertical scale and that the time changes in those concentrations correlate extremely well with the time changes in torque (cc = 0.87). In contrast, the OOP bending moment magnitude variations do not follow the time changes in horizontal velocity along the met tower, and horizontal velocity correlates poorly with the OOP bending moment (cc = -0.37). As previously discussed, although the 10-min average in bending moment is lower than that for torque, there are significant periods in which OOP bending moment exceeds torque. Like horizontal velocity, the temporal variations in the nontorque bending moment are uncorrelated with the temporal variations in torque.

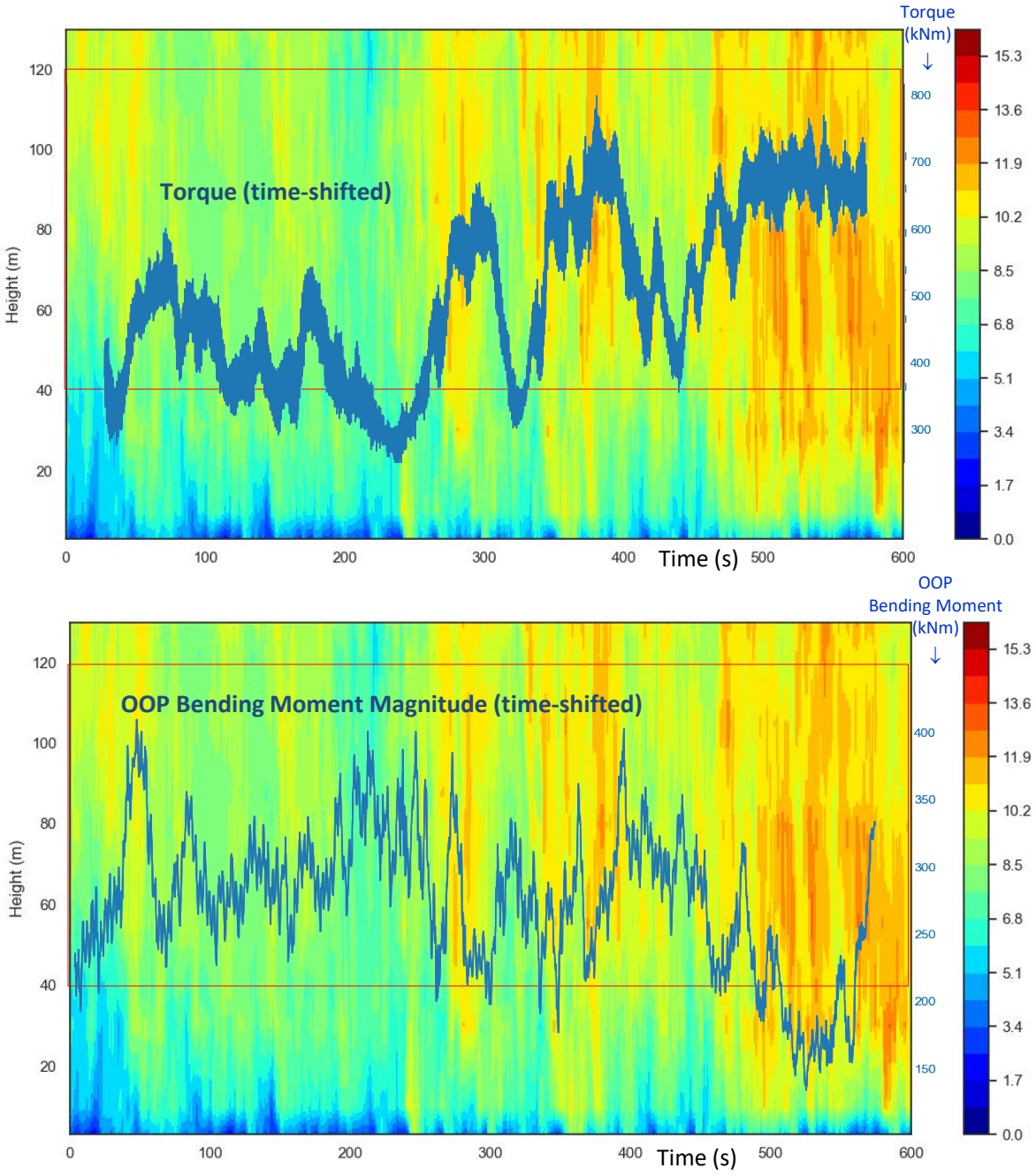

Figure 35. Isocontours of space-time varying horizontal velocity in westerly winds measured by all available anemometers on the met tower and time-shifted to the turbine rotor, together with torque and OOP bending moment vector magnitude.

The red lines indicate the rotor boundaries. The color bar for wind speed is in m/s. The cc between wind speed and torque (top) is 0.87 and between wind speed and OOPBM is –0.37.

10.4 The Fundamentally Different Mechanisms Underlying Time Changes in Power vs. Nonsteady Forcing of the Main Bearing

Because only five anemometers constrained to a vertical line were available over the GE 1.5-MW wind turbine rotor, it was not possible to replicate the integral in the asymmetry parameter (Eq. (3)) that was quantified with space-time computer simulation over the NREL 5-MW wind turbine. Various alternatives were tried, but the sparsity of data points made it impossible to generate a meaningful asymmetry measure. However, given the correspondence between the computational and field experiments, we may conclude that the variations in OOP bending moment are driven by the level of asymmetry in the horizontal velocity field over the rotor plane as the rotor blades rotate through coherent eddy structures. As discussed in Section 2.3 in context with Figure 32, asymmetry in horizontal velocity causes asymmetry in the loadings on the three blades as they rotate through the internal eddy structure, thus creating asymmetrical distributions of the individual moment contributions from the three blades and the corresponding generation of OOP bending moments. These time-varying bending moments create nonsteady changes in radial force on the main bearing (Eq. (1)), in both magnitude and direction. These time-varying changes in force vector create nonsteady changes in the magnitude, orientation, and extent of the load zone over the inner ring of the main bearing.

In contrast with the aerodynamic generation of nontorque bending moment and consequent forcing of the main bearing, power generation is a consequence of the aerodynamic creation of torque. We have shown that, whereas nontorque bending moments are generated by the asymmetries in the velocity distribution over the rotor plane, torque is generated from the average rotor-normal velocity over the rotor plane. Initially obtained from computational experiments, this important result is verified experimentally by the existence of very high temporal correlations between net rotor velocity and torque. Because the lateral scale of both the atmospheric and mountain eddies is of order the rotor diameter, both the velocity at the hub anemometer and the rotor-averaged velocity are highly correlated with torque; however, the correlation is stronger with rotor-averaged velocity.

In the current study we focus on the time changes in the OOP moment at the rotor hub in response to the passage of turbulence eddies in the atmosphere with the recognition that these strong nonsteady forcings create strong time changes in the direction and magnitude of the bearing force vector. However, the potentially deleterious impacts of atmospheric turbulence may also involve the time variations in axial thrust induced by the passage of atmospheric eddies (Figure 4). For example, an impulsive axial force on the main shaft might induce main bearing roller displacement at the time that the main bearing experiences an impulsive increase in OOP moment and radial main bearing force so as to encourage damage to the roller. In addition, the bearing force includes a large rotor weight contribution that biases the direction and magnitude of the axial and radial forces on the main bearing. To fully understand the impacts of atmospheric turbulence on the main bearing, it is necessary to integrate the important new understanding obtained in the current study with analysis of other relevant contributions to the structural responses of the wind turbine main bearing from atmospheric turbulence.

References

Aguasvivas, S., A. Lavely, G. Vijayakumar, J.G. Brasseur, S. Schmitz, and E. Duque. 2015. "Nonsteady Wind Turbine Loading Response to Passage of Daytime Turbulence Eddies." Gallery of Fluid Motion, 68th Annual Meeting of the Division of Fluid Dynamics. doi: 10.1103/APS.DFD.2015.GFM.V0038.

ASOS Network. 2019. ASOS-AWOS-METAR Data Download, Iowa Environmental Mesonet, available at: https://mesonet.agron.iastate.edu/request/download.phtml.

Castro, I.P. and A.G. Robins. 1977. "The Flow Around a Surface-Mounted Cube in Uniform and Turbulent Streams." *Journal of Fluid Mechanics* 79 (2): 307–335. doi: 10.1017/S0022112077000172.

Chovan, C. 2018. "TDI Mainshaft Bearing – Field Test Results." Presented at AWEA Wind Project O&M and Safety Conference.

Chovan, C. 2019. "Seven Years of Solid Results." *Wind Systems* 11 (3): 17–20. https://www.windsystemsmag.com/wp-content/uploads/2019/03/0319-IF-2.pdf.

Clifton, A. 2014. *135-m Meteorological Masts at the National Wind Technology– Instrumentation, Data Acquisition and Processing.* https://wind.nrel.gov/MetData/Publications/NWTC_135m_MetMasts.pdf.

Clifton, A. 2016. *135-m Meteorological Towers at the National Wind Technology Center, An Unofficial Guide to Data Products*, May 2, 2016. NREL Technical Report (unpublished).

Dao, C., B. Kazemtabrizi, and C. Crabtree. 2019. "Wind Turbine Reliability Data Review and Impacts on Levelised Cost of Energy." *Wind Energy* 22 (12): 1848–1871. doi: 10.1002/we.2404.

Hart, E., A. Turnbull, J. Feuchtwang, D. McMillan, E. Golysheva, and R. Elliott. 2019. "Wind Turbine Main-bearing Loading and Wind Field Characteristics." *Wind Energy* 22 (11): 1534–1547. doi: 10.1002/we.2386.

Hart, E., B. Clarke, G. Nicholas, A. Kazemi Amiri, J. Stirling, J. Carroll, R. Dwyer-Joyce, A. Mc-Donald, and H. Long. 2020. "A Review of Wind Turbine Main-bearings: Design, Operation, Modelling, Damage Mechanisms and Fault Detection." *Wind Energy Science* 5 (1): 105–124. doi: 10.5194/wes-5-105-2020.

Hart, E. 2020. "Developing a Systematic Approach to the Analysis of Time-varying Main Bearing Loads for Wind Turbines." *Wind Energy* 23 (12): 2150–2165. doi: 10.1002/we.2549.

Hart, E., A. Stock, G. Elderfield, R. Elliott, J. Brasseur, J. Keller, Y. Guo, and W. Song. 2022. "Impacts of Wind Field Characteristics and Non-steady Deterministic Wind Events on Time-varying Main-bearing Loads." *Wind Energy Science* 7 (3): 1209–1226. doi: 10.5194/wes-7-1209-2022.

Hart, E., K. Raby, J. Keller, S. Sheng, H. Long, J. Carroll, J. Brasseur, and F. Tough. 2023. *Main Bearing Replacement and Damage − A Field Data Study on 15 Gigawatts of Wind Energy Capacity*. Golden, CO: National Renewable Energy Laboratory. NREL/TP-5000-86228. https://www.nrel.gov/docs/fy23osti/86228.pdf.

Hearst, R.J., G. Gomit, and B. Ganapathisubramani. 2016. "Effect of Turbulence on the Wake of a Wall-mounted Cube." *Journal of Fluid Mechanics* 804: 513–530. doi: 10.1017/jfm.2016.565.

Jayaraman, B. and J.G. Brasseur. 2021. “Transition in Atmospheric Boundary Layer Turbulence Structure from Neutral to Convective and Large-scale Rolls.” *Journal of Fluid Mechanics* 913: A42, doi: 10.1017/jfm.2021.3.

Jonkman, J., S. Butterfield, W. Musial, and G. Scott. 2009. *Definition of a 5-MW Reference Wind Turbine for Offshore System Development*, Golden, CO: National Renewable Energy Laboratory. NREL/TP-500-38060. doi: 10.2172/947422.

Jha, P. K. and S. Schmitz. 2016. “Blade Load Unsteadiness and Turbulence Statistics in an Actuator-Line Computed Turbine-Turbine Interaction Problem." *Journal of Solar Energy Engineering* 138 (3): 031002. doi: 10.1115/1.4032545.

Johansson, C., A-S. Smedman, U. Högström, J.G. Brasseur, and S. Khanna. 2001. “Critical Test of the Validity of the Monin-Obukhov Similarity during Convective Conditions.” *Journal of the Atmospheric Sciences* 58 (12): 1549–1566. doi: 10.1175/1520-0469.

Kaimal, J.C., J.C. Wyngaard, and O.R. Cote. 1972. “Spectral Characteristics of Surface-layer Turbulence.” *Quarterly Journal of the Royal Meteorological Society* 98 (417): 563–589. doi: 10.1002/qj.49709841707.

Keller, J., S. Sheng, J. Cotrell, and A. Greco. 2016. *Wind Turbine Drivetrain Reliability Collaborative Workshop: A Recap* (Technical Report). DOE/GO-102016-4878. National Renewable Energy Laboratory: Golden, CO. http://www.nrel.gov/docs/fy16osti/66593.pdf.

Keller, J, Y. Guo, and L. Sethuraman. 2019. *Uptower Investigation of Main and High-Speed-Shaft Bearing Reliability* Golden, CO: National Renewable Energy Laboratory. NREL/TP-5000-71529. http://www.nrel.gov/docs/fy19osti/71529.pdf.

Keller, J., S. Sheng, Y. Guo, B. Gould, and A. Greco. 2021. *Wind Turbine Drivetrain Reliability and Wind Plant Operations and Maintenance Research and Development Opportunities*. Golden, CO: National Renewable Energy Laboratory. NREL/TP-5000-80195. https://nrel.gov/docs/fy21osti/80195.pdf.

Kenworthy, J., J.G. Brasseur, J. Keller, E. Hart, and Y. Guo. 2023a. “Nonsteady Load Responses on the Main Shaft by the Passage of Daytime Atmospheric Turbulence Eddies through the Rotor of Utility-scale Wind Turbines.” (NAWEA)/WindTech Conference 2023, Denver, CO, USA, 30 October 2023. https://www.nrel.gov/docs/fy23osti/86303.pdf.

Kenworthy, J., E. Hart, J. Stirling, A. Stock, J. Keller, Y. Guo, J. Brasseur, and R. Evans. 2023b. “Wind Turbine Main Bearing Rating Lives as Determined by IEC 61400-1 and ISO 281: A Critical Review and Exploratory Case Study.” *Wind Energy* 27 (2): 179–197. doi: 10.1002/we.2883.

Khanna, S. and J.G. Brasseur. 1998. “Three-Dimensional Buoyancy- and Shear-Induced Local Structure of the Atmospheric Boundary Layer.” *Journal of the Atmospheric Sciences*, 55 (5): 710–743. doi: 10.1175/1520-0469.

Kotzalas, M.N. and Doll, G.L. 2010. “Tribological Advancements for Reliable Wind Turbine Performance.” *Philosophical Transactions of the Royal Society A* 368 (1929): 4829–4850. doi: 10.1098/rsta.2010.0194.

Lavely, A., G. Vijayakumar, B. Craven, B. Jayaraman, P. Jha, T. Nanci, E.G. Paterson, and J.G. Brasseur. 2014. "Toward a Blade-resolved Hybrid URANS-LES of the NREL 5 MW Wind Turbine Rotor within Large-eddy Simulation of the Atmospheric Boundary Layer." AIAA 2014-0869, AIAA SciTech, National Harbor 2014. doi: 10.2514/6.2014-0869.

Lavely, A. W. 2017. Effects of Daytime Atmospheric Boundary Layer Turbulence on the Generation of Non-steady Wind Turbine Loadings and Predictive Accuracy of Lower Order Models. PhD thesis, Pennsylvania State University. https://etda.libraries.psu.edu/files/final_submissions/15433.

Martínez-Tossas, L. A., M.J. Churchfield, and C. Meneveau. 2017. "Optimal Smoothing Length Scale for Actuator Line Models of Wind Turbine Blades Based on Gaussian Body Force Distribution." *Wind. Energy* 20 (6): 1083–1096. doi: 10.1002/we.2081.

Nandi, T. N., A. Herrig, and J. G. Brasseur. 2017. "Non-Steady Wind Turbine Response to Daytime Atmospheric Turbulence." *Philosophical Transactions of the Royal Society A* 375 (2091): 20160103. doi: 10.1098/rsta.2016.0103.

Santos, R. and J. van Dam. 2015. *Mechanical Loads Test Report for the U.S. Department of Energy 1.5-Megawatt Wind Turbine.* Golden, CO: National Renewable Energy Laboratory. NREL/TP-5000-63679. http://www.nrel.gov/docs/fy15osti/63679.pdf.

Sørensen, J. N. and W.Z. Shen. 2002. "Numerical Modeling of Wind Turbine Wakes." *ASME Journal of Fluids Engineering* 124 (2): 393–399. doi: 10.1115/1.1471361.

St. Martin, C.M., J.K. Lundquist, A. Clifton, G.S. Poulos, and S.J. Schreck. 2017. "Atmospheric Turbulence Affects Wind Turbine Nacelle Transfer Functions." *Wind Energy Science* 2 (1): 295–306. doi: 10.5194/wes-2-295-2017.

Svensson, G.,·A.A.M. Holtslag, V. Kumar, et al.. 2011. "Evaluation of the Diurnal Cycle in the Atmospheric Boundary Layer Over Land as Represented by a Variety of Single-Column Models: The Second GABLS Experiment." *Boundary-Layer Meteorology* 140: 177–206. doi: 10.1007/s10546-011-9611-7.

UK Gov. 2019 *Industrial Strategy - Offshore Wind Sector Deal*, UK Government, Department for Business, Energy & Industrial Strategy.

Wiser, R., E. Lantz, T. Mai, J. Zayas, E. DeMeo, E. Eugeni, J. Lin-Powers, and R. Tusing. 2015 "Wind Vision: A New Era for Wind Power in the United States." *The Electricity Journal* 28 (9): 120–132. doi: 10.1016/j.tej.2015.09.016.

Vijayakumar, G., J. G. Brasseur, A. W. Lavely, M. P. Kinzel, E. G. Paterson, M. J. Churchfield, and P. J. Moriarty. 2012. "Considerations in Coupling LES of the Atmosphere to CFD around Wind Turbines." AIAA 2012-0817, AIAA Aerospace Sciences Meeting, January, Nashville, TN. doi: 10.2514/6.2012-817.

Vijayakumar, G., J. G. Brasseur, A. Lavely, B. Jayaraman, and B. C. Craven. 2016. "Interaction of Atmospheric Turbulence with Blade Boundary Layer Dynamics on a 5MW Wind Turbine using Blade-Boundary-Layer-Resolved CFD with Hybrid URANS-LES." AIAA2016-0521. AIAA SciTech Meeting, January, San Diego, CA. doi: 10.2514/6.2016-0521.

Vijayakumar, G. and J. G. Brasseur. 2019. “Blade-resolved Modeling with Fluid-structure Interaction.” Ch. 2 in: Veers, P. (Ed.), Wind Energy Modeling and Simulation - Volume 1: Atmosphere and Plant. Institute of Engineering and Technology (IET), doi: 10.1049/PBPO125F_ch2.

Wiser, R. and M. Bolinger. 2019. 2018 Wind Technologies Market Report (Technical Report). DOE/GO-102019-5191. U.S. Department of Energy: Washington, D.C., 2019. doi: 10.2172/1559241.

Wiser, R., M. Bolinger, and E. Lantz. 2019. “Assessing Wind Power Operating Costs in the United States: Results from a Survey of Wind Industry Experts.” *Renewable Energy Focus* 30: 46–57. doi: 10.1016/j.ref.2019.05.003

Wyngaard, J.C. 2010. *Turbulence in the Atmosphere.* Cambridge University Press, New York. doi: 10.1017/CBO9780511840524.